Mass Resolution Study of the B_s-Meson with First LHCb Data

Dissertation

zur

Erlangung der naturwissenschaftlichen Doktorwürde
(Dr. sc. nat.)

vorgelegt der
Mathematisch-naturwissenschaftlichen Fakultät
der

Universität Zürich

von

Angela Büchler

aus
Goldach/SG

Promotionskomitee

Prof. Dr. Ulrich Straumann (Vorsitz)
Dr. Jeroen Van Tilburg
Dr. Olaf Steinkamp

Zürich 2012

Abstract

The rare decay $B_s^0 \to \mu^+\mu^-$ is very strongly suppressed in the Standard Model. As a flavour-changing neutral current, this decay is forbidden at the tree-level and can only be introduced by higher order loop processes. New physics models beyond the Standard Model typically include an extended particle spectrum, which might influence the loop processes measurably. The analysis of the $B_s^0 \to \mu^+\mu^-$ branching ratio at the LHCb experiment provides interesting possibilities to constrain the parameter space of some new physics models.

The LHC at CERN Geneva is the most powerful ring accelerator at the moment. LHCb is one of the four main experiments at the LHC and is dedicated to physics in the B-meson sector. The work was divided in two main parts: an experimental part and an analysis part.

The Tracker Turicensis was successfully installed and commissioned from 2006–2009. In parallel the slow control software for the Tracker Turicensis was developed and tested. Tuning of hardware and software parameters was achieved during the proton injection tests to the LHC before proton-proton collisions happened in the LHC. After the successful commissioning of the detector in October 2009, more than 99.7% of about 143000 readout channels were working, which is of great importance for the precision measurements of the LHCb experiment.

The second part of this work is related to the analysis of the $B_s^0 \to \mu^+\mu^-$ branching ratio. The relevant parts of the analysis to determine a limit on the branching ratio for $B_s^0 \to \mu^+\mu^-$ are described. However the main focus of this work lies on a novel method on the basis of error propagation to estimate the invariant mass resolution on an event-by-event basis for a two body decay from data. A correction factor on the relative error on the momentum of the decay particles was developed to achieve a proper calibration of the error on the momentum and the mass resolution from data. The systematic uncertainty on the mass resolution determined by this novel method, using the correction factor, was found to be 1.96%, which is lower than the systematic error of the methods currently used in the $B_s^0 \to \mu^+\mu^-$ analysis.

Keywords: CERN, LHC, LHCb, Tracker Turicensis, Silicon Tracker, commissioning, injection test, PVSS, data acquisition, readout, detector mapping, slow control, ECS, timing settings, rare decay, $B_s^0 \to \mu^+\mu^-$, flavour-changing neutral current, mass resolution, correction factor

Zusammenfassung

Der sehr seltene Zerfall $B_s^0 \to \mu^+\mu^-$ ist im Standard Modell stark unterdrückt. Es ist ein sogenannt flavour-ändernder neutraler Prozess, der in erster Ordnung (tree-level) verboten ist und nur durch sogenannte Loopprozesse höherer Ordnung stattfinden kann. Neue Physik Modelle, die über das Standard Modell hinausgehen, schlagen typischerweise ein erweitertes Teilchenspektrum vor, das die erwähnten Loopprozesse messbar beeinflussen könnte. Daher ist eine Analyse der Zerfallsrate von $B_s^0 \to \mu^+\mu^-$ am LHCb Experiment eine vielversprechende Möglichkeit, den Parameterbereich neuer Physik Modelle einzugrenzen.

Der LHC am CERN in Genf ist gegenwärtig der leistungsfähigste Ringbeschleuniger. LHCb ist eines der vier Hauptexperimente des LHC, dessen Hauptaugenmerk der Physik im B-Meson Bereich gilt. Die vorliegende Arbeit ist in zwei Teile gegliedert: einen experimentellen Teil und einen Analyseteil.

Der Tracker Turicensis wurde in den Jahren 2006–2009 erfolgreich installiert und in Betrieb genommen. Parallel dazu wurde die Steuerungssoftware für den Tracker Turicensis entwickelt und getestet. Injektionen von Protonen in den LHC-Speicherring erlaubten eine Kalibrierung von Hardware- und Softwareparametern des Tracker Turicensis schon vor den ersten Proton-Proton Kollisionen im LHC. Nach der erfolgreichen Inbetriebnahme des Detektors im Oktober 2009 funktionierten mehr als 99.7% der rund 143000 Auslesekanäle, was für die Präzisionsmessungen des LHCb Experiments von entscheidendender Bedeutung ist.

Der zweite Teil dieser Arbeit hängt eng mit der Analyse der $B_s^0 \to \mu^+\mu^-$ Zerfallsrate zusammen. Daher sind die wichtigsten Schritte zur Ermittlung der oberen Grenze des $B_s^0 \to \mu^+\mu^-$ Verzweigungsverhältnisses beschrieben. Der Fokus der Arbeit liegt jedoch auf einer neuen Methode, die auf der Grundlage der Fehlerfortpflanzung aus den rekonstruierten Spurparametern der Zerfallsteilchen den Messfehler auf der invarianten Masse für jedes Ereignis abschätzt, ohne sich auf simulierte Daten zu stützen. Damit kann die Auflösung der invarianten Masse eines Zweikörperzerfalls wie zum Beispiel $B_s^0 \to \mu^+\mu^-$ aus den gemessenen Daten abgeschätzt werden. Ein Korrekturfaktor für den relativen Fehler auf dem Impuls der Zerfallsteilchen wurde entwickelt, um eine korrekte Eichung aus den Daten zu erreichen. Die Eichung mit Hilfe des entwickelten Korrekturfaktors zusammen mit der neuen Methode reduziert den systematischen Messfehler auf der Auflösung der invarianten Masse gegenüber den momentan verwendeten Methoden für die $B_s^0 \to \mu^+\mu^-$ Analyse und beträgt 1.96%.

Contents

Introduction

This thesis presents an alternative method to estimate the mass resolution of the rare decay $B_s^0 \to \mu^+\mu^-$ at LHCb from data. The Standard Model makes a precise prediction for the $B_s^0 \to \mu^+\mu^-$ branching ratio:

$$\text{BR}(B_s^0 \to \mu^+\mu^-) = (3.2 \pm 0.2) \cdot 10^{-9} \quad [1]. \tag{1}$$

A deviation of the branching ratio from the theoretical prediction of the Standard Model would point to contributions from new physics with an extended particle spectrum. The experimental measurement of the $B_s^0 \to \mu^+\mu^-$ branching ratio has thus great importance in searching for new physics and constraining the parameter space of new physics models.

Searches for this decay have been performed by experiments at e^+e^- B-factories and at the Tevatron in Chicago. However, none of these experiments has reached the sensitivity required to observe the rare decay $B_s^0 \to \mu^+\mu^-$ as predicted by the Standard Model yet. The LHCb detector is a powerful instrument to reconstruct B-decays with high precision. An important ingredient for a successful study of rare B-decays is a high momentum resolution, which LHCb is able to provide. The silicon micros trip detector Tracker Turicensis, which was designed and built at the University of Zurich, is crucial for a precise momentum measurement. The the stable operation and the calibration of the Tracker Turicensis is of great importance to achieve competitive physics results. A successful installation, a reliable detector control- and safety system and a careful commissioning of the Tracker Turicensis were the first steps to achieve these goals. After the main commissioning phase in October 2009, more than 99.7% of about 143000 readout channels were working. Data collected during proton injection tests to the LHC led to a better understanding of the tracking system and helped to fine tune hard- and software parameters before first proton-proton collisions in the LHC happened. As a first approach to improve the mass resolution, mainly the more common decay channels were studied for calibration. With the data collected until the end of 2010 an upper limit on the $B_s^0 \to \mu^+\mu^-$ branching ratio was achieved by the $B_s^0 \to \mu^+\mu^-$ working group:

$$\text{BR}(B_s^0 \to \mu^+\mu^-) < 4.3(5.6) \cdot 10^{-8} \quad \text{at } 90\% \text{ (}95\%\text{) C.L. [2].} \tag{2}$$

This result demonstrates the excellent performance of the LHCb detector.

The main part of this work focuses on the estimation of the invariant mass resolution for 2-body decays from data on an event-by-event basis using error propagation from reconstruced track parameters. The first data collected until end of 2010 were used to evaluate the method and to calibrate the mass resolution. The evaluation revealed an underestimation of the track fit errors on the momenta of the particles. A method to estimate correction factors was developed to achieve a proper calibration of the uncertainty on the track momentum from data. The systematic error on the determination of the invariant the mass resolution was found to be 1.96%, which is lower than the methods used in the published $B_s^0 \to \mu^+\mu^-$ analysis.

This thesis is divided into six chapters. In chapter 1 the Standard Model and flavour-changing neutral current decays are described, with the focus on the $B_s^0 \to \mu^+\mu^-$ decay. Chapter 2 describes the LHC and LHCb as well as the subdetector Tracker Turicensis. Chapter 3 gives an overview of the readout system and the hard- and slow-control software structure of the Tracker Turicensis and provides a closer look at its control- and safety system. In chapter 4 the tuning of hard- and software parameters with LHC proton injection tests is described and an insight is given to commissioning, the problems encountered, the lessons learned and the implemented solutions. In chapter 5 the key parts of the published analysis of the $B_s^0 \to \mu^+\mu^-$working group for the $B_s^0 \to \mu^+\mu^-$ decay is presented. Chapter 6 explains the technique for estimating of the invariant mass resolution for $B_s^0 \to \mu^+\mu^-$ from data.

Chapter 1

Theory

To understand why it is interesting to study the $B_s^0 \to \mu^+\mu^-$ decay, some introductory words about the Standard Model and possible extensions are given. The concepts of flavour and quark mixing are briefly introduced. After presenting the flavour-changing neutral currents, the motivation for a $B_s^0 \to \mu^+\mu^-$ analysis is explained.

1.1 The Standard Model and beyond

What is the world made of? Research tries to answer this question already for a long time in a organised way. Earlier approaches led for example to the periodic table, organising the chemical elements. Now the picture has evolved and the particles, which are believed to be fundamental, are found a few levels deeper than the chemical elements. To describe these fundamental particles and their interactions a theoretical model is used which is called the Standard Model. It is built from a general framework of gauge theories and describes the particles and the interactions as fields. Three of the fundamental forces of nature, the electromagnetic, the weak and the strong force, are part of the Standard Model. The electromagnetic and the weak force are combined in the unified electroweak model and the strong force is modelled by quantum chromo dynamics (QCD). Gravitation, the fourth fundamental force, has a negligible influence on the particles and the interactions studied with current accelerators. Gravitation is not part of the Standard Model. The three forces or interactions, are represented by quantised bosonic fields (integer spin) and the fundamental particles as quantised fermionic fields (half-integer spin) called quarks and leptons as Figure 1.1 illustrates. The Standard Model can be used to calculate predictions for scattering cross-sections, decay rates and other measurable quantities.

From a theoretical point of view the Standard Model is unsatisfactory, but its predictions were very well confirmed from measured data. It does not explain the existence of quantum numbers such as: the electric charge, hypercharge and colour. Furthermore it has 19 arbitrary parameters plus another 9 (7) for the Majorana

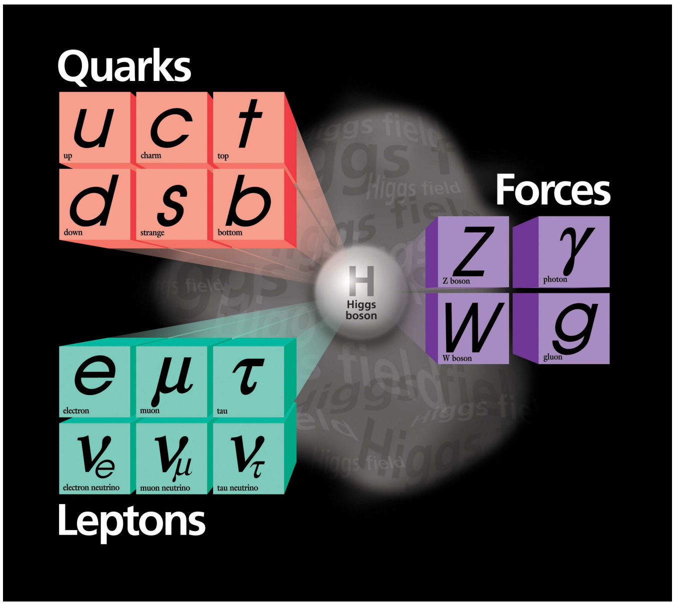

Figure 1.1: Quantised fields of the Standard Model . The quarks and leptons are represented in three flavours which distinguish themselves only by the mass.

(Dirac) neutrinos. The 19 parameters are:

- 3 independent vector boson couplings: g_{weak}, g'_{weak} (SU(2)×U(1)) and g_{strong} (SU(3)),
- 6 quark masses,
- 3 charged lepton masses,
- 3 generalised Cabibbo weak mixing angles (CKM angles see section 1.2),
- 1 CP-violating CKM phase,
- 1 W boson mass,
- 1 Higgs boson mass,
- 1 QCD vacuum angle.

The following open questions cannot be addressed with the Standard Model framework: What is the origin of mass, does the Higgs mechanism explain it? Is there a framework for unifying all particle interactions (Grand Unification Theories GUT)? Why is there flavour or, in other words, why do particles have partners in two other flavour generations with the same properties except that they are heavier?

Super Symmetry [3] is one approach to some of these questions. It is based on a symmetry relating bosons and fermions: each fermion has a boson and each boson

Table 1.1: Particle content of the MSSM (modified from Ref. [4]). The supersymmetric partners are indicated by a tilde.

Names	bosons, spin 0	fermions, spin $\frac{1}{2}$
squarks, quarks ($\times 3$ generations)	$(\widetilde{u}_\mathrm{L}, \widetilde{d}_\mathrm{L})$ $\widetilde{u}_\mathrm{R}$ $\widetilde{d}_\mathrm{R}$	$(u_\mathrm{L}, d_\mathrm{L})$ u_R d_R
sleptons, leptons ($\times 3$ generations)	$(\widetilde{\nu}, \widetilde{e}_\mathrm{L})$ $\widetilde{e}_\mathrm{R}$	(ν, e_L) e_R
Higgs, Higgsinos	$(H_\mathrm{u}^+, H_\mathrm{u}^0)$ $(H_\mathrm{d}^0, H_\mathrm{d}^-)$	$(\widetilde{H}_\mathrm{u}^+, \widetilde{H}_\mathrm{u}^0)$ $(\widetilde{H}_\mathrm{d}^0, \widetilde{H}_\mathrm{d}^-)$

	bosons, spin 1	fermions, spin $\frac{1}{2}$
gluon, gluino	g	$\widetilde{g}$
W bosons, winos	$W^\pm$	$\widetilde{W}^\pm$
Z boson, zino	Z^0	$\widetilde{Z}^0$
photon, photino	γ	$\widetilde{\gamma}$

has a fermion as a superpartner. The names of the bosonic superpartners are constructed with prepending an ’s’ to the Standard Model fermion names (for example sdown, selectron) and the names of the fermionic superpartners are constructed by appending ’ino’ to the Standard Model boson names (for example photino, wino). An overview of the particles in the minimal supersymmetric standard model (MSSM) is given in Table 1.1.

The mass eigenstates of the Higgs bosons H_u^0, H_d^0, H_u^+ and H_d^- are h^0, H^0, A^0 and $H^\pm$. The mass eigenstates of the charginos $\widetilde{W}^\pm$, $\widetilde{H}_\mathrm{u}^+$ and $\widetilde{H}_\mathrm{d}^-$ are $\widetilde{\chi}_1^\pm$ and $\widetilde{\chi}_2^\pm$. None of the superpartners has yet been found experimentally. Their masses are different from the ones of the Standard Model particles, which implies Super Symmetry to be broken. Standard Model particles and their superpartners have equal couplings. Together with the equal number of bosons and fermions in supersymmetric models, this leads to the cancelation of one loop corrections to the higgs mass parameter, which is an advantage compared to the Standard Model.

Further advantages of super-symmetric models are the unification of the gauge couplings and the possible inclusion of gravity [3]. With R-parity[1] conservation the lightest neutral super-symmetric particle is stable, which provides a good candidate for dark matter.

Another argument for Super Symmetry is also the experimentally measured value of $\sin^2 \Theta_\mathrm{Weinberg} \approx 0.23$ [5]. Θ_Weinberg has the following relation to the weak

---

[1] The R-parity is defined as: $\mathcal{R} = (-1)^{3\mathrm{B}+\mathrm{L}+2\mathrm{J}}$, where B is the baryon number, L the lepton number and J the spin of the particle. Standard Model particles have $\mathcal{R} = +1$ and the supersymmetric partners have $\mathcal{R} = -1$.

coupling constants:

$$\tan \Theta_{\text{Weinberg}} = \frac{g'_{\text{weak}}}{g_{\text{weak}}} \quad . \tag{1.1}$$

The GUT prediction for its value without Super Symmetry is $\sin^2 \Theta_{\text{Weinberg}} = 0.214$, whereas with Super Symmetry it is $\sin^2 \Theta_{\text{Weinberg}} = 0.232$ and therefore closer to the experimentally measured value.

From now on all the models beyond the Standard Model are referred to as new physics.

1.2 Flavour, Quark Mixing and CP violation

The concept of flavour is interesting because it can probe new physics before direct observation. For example the charm quark, belonging to the second flavour generation, and its mass were predicted before experimentally found. To introduce CP violation Kobayashi and Maskawa proposed a third generation of quarks. The b-quark was found in 1977 by the measurement of the $b\bar{b}$ resonance Υ(1S) [6]. The CP violation was discovered in the neutral Kaon system [7]. The measurement of the mass difference between the mass eigenstates of the B^0 - $\bar{B}^0$ system Δm_d led to the prediction of the top quark mass [8].

The Cabibbo-Kobayashi-Maskawa matrix (V$_{CKM}$) connects the weak eigenstates (d',s',b') and the corresponding mass eigenstates (d,s,b):

$$\begin{pmatrix} d' \\ s' \\ b' \end{pmatrix} = \begin{pmatrix} V_{ud} & V_{us} & V_{ub} \\ V_{cd} & V_{cs} & V_{cb} \\ V_{td} & V_{ts} & V_{tb} \end{pmatrix} \cdot \begin{pmatrix} d \\ s \\ b \end{pmatrix} \tag{1.2}$$

It is the 3×3 extension of the 2×2 Cabibbo mixing matrix. The CKM matrix is unitary and its entries give a measure of the quark mixing rate. The unitarity implies the absence of flavour changing neutral currents which are explained in section 1.3. The matrix can be parametrised by three mixing angles (θ_{12}, θ_{13}, θ_{23}) and a complex phase (δ) [9]. the parametrisation

1.3 Flavour-Changing Neutral Currents

There are two ways to look for new physics: direct and indirect searches. Direct searches in high-p_T physics are primarily a domain of general purpose detectors like ATLAS and CMS at the LHC. Indirect searches in flavour physics look for observable deviations from the Standard Model, coming from new (virtual) particles in loop processes. Rare B-meson decays are induced through flavour-changing neutral currents (FCNC). A FCNC transition changes the flavour of the quark or the lepton without changing its electric charge. In the Standard Model the FCNC processes are forbidden at the lowest order (tree level) but can still be introduced by

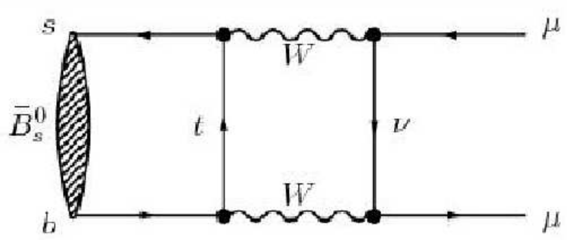

Figure 1.2: Feynman box diagram for the $B_s^0 \to \mu^+\mu^-$ decay.

loops in higher order processes. Loops often involve very heavy particles, not accessible directly with accelerator energies. One way to indirectly access the properties of these heavier particles is to study FCNCs. Figure 1.2 shows a Feynman diagram of the B_s^0 meson decaying into a muon pair by FCNCs. These processes are very strongly suppressed in the Standard Model and the predicted Standard Model branching ratio is:

$$\text{BR}(B_s^0 \to \mu^+\mu^-) = (3.2 \pm 0.2) \cdot 10^{-9} \quad [1] \tag{1.3}$$

1.4 Motivation for an analysis on $B_s \to \mu^+\mu^-$

The $B_s^0 \to \mu^+\mu^-$ decay is very strongly suppressed in Standard Model, new physics contributions can appear at the same order as the in the Standard Model and the decay is very well predicted from the theory side (Equation (1.3)). A precise measurement of the branching ratio could show a clear indication of new physics and constrain the parameter space of these models. The actual CDF measurement only gives an upper limit:

$$\text{BR}(B_s^0 \to \mu^+\mu^-) < 3.6 \cdot 10^{-8} \text{ at } 90\% \text{ CL [10]} \tag{1.4}$$

The branching ratio can be strongly enhanced by new scalar and/or pseudo scalar interactions (Figure 1.3 shows an example), as will be explained by the method of operator product expansion. This method gives the decay amplitude ($\mathcal{M}$) of B-decays (B) to a final state (f):

$$\mathcal{M} = \langle f | H_{\text{eff}} | B \rangle \tag{1.5}$$

The effective Hamiltonian H_{eff} is proportional to the Fermi coupling constant G_F

$$G_F = \frac{\sqrt{2}}{8} \frac{g_{\text{weak}}^2}{m_W^2} \quad , \tag{1.6}$$

the CKM matrix elements V_{ts} and V_{tb} and the sum over the product of Wilson

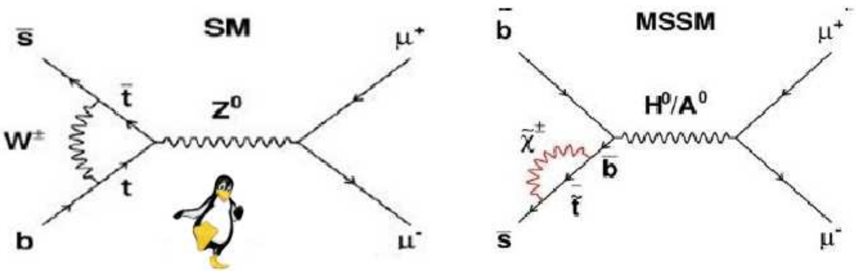

Figure 1.3: Left: Penguin diagram of a Standard Model $B_s^0 \to \mu^+\mu^-$ decay. Rigth: Example of possible new physics contributions: chargino ($\widetilde{\chi^{\pm}}$ anti-stop ($\widetilde{t}$) loop and neutral Higgs boson interaction (H^0, A^0).

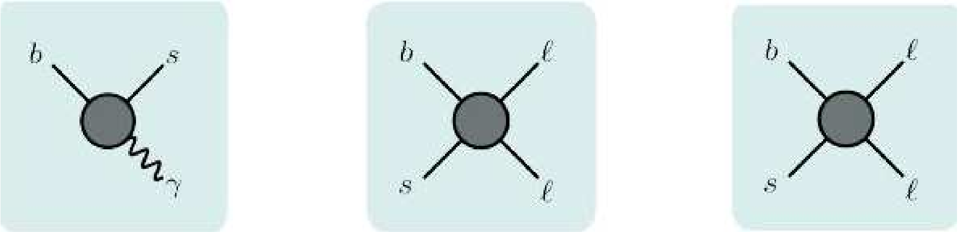

Figure 1.4: Left: $\mathcal{O}_7$ Photon penguin. Center: $\mathcal{O}_{9,10}$ Electroweak penguin. Right: $\mathcal{O}_{S,P}$ Higgs scalar and pseudo-scalar penguin.

coefficients C_i and operators $\mathcal{O}_i$ as shown in Equation (1.7).

$$H_{\text{eff}} = -\frac{4G_F}{\sqrt{2}} V_{ts}^* V_{tb} \sum_i C_i(\mu)\mathcal{O}_i(\mu) \begin{cases} i{=}1{,}2 & \text{Tree} \\ i{=}3{-}6{,}8 & \text{Gluon penguin} \\ i{=}7 & \text{Photon penguin} \\ i{=}9{,}10 & \text{Electroweak penguin} \\ i{=}S & \text{Higgs (scalar) penguin} \\ i{=}P & \text{Pseudoscalar penguin} \end{cases} \tag{1.7}$$

The Wilson coefficients relate to short-distance effects and the operators to long-distance effects. Figure 1.4 shows the diagrams for the operators of the photon penguin, the electroweak penguin and the scalar and pseudo-scalar Higgs penguin. New physics can modify the Wilson coefficients C$_i$ or introduce new operators $\mathcal{O}_i$. That affects observable quantities such as: branching ratios (for example BR($B_s^0 \to \mu^+\mu^-$) (C$_S$, C$_P$)), angular distributions (for example in $B_d^0 \to K^*\mu^+\mu^-$, (C$_9$, C$_{10}$, C$_7$)) or polarisation (for example in $B_s \to \varphi\gamma$). The MSSM proposes the Wilson coefficients $C_{S,P}$ to be proportional to $\tan^3\beta$:

$$C_{S,P}^{MSSM} \propto \frac{m_\mu \tan^3\beta}{M_A^2} \tag{1.8}$$

where m_μ is the muon mass, $\tan\beta$ the ratio of the vacuum expectation values of the two Higgs fields and M_A is the mass of the neutral pseudo-scalar Higgs boson A^0.

Many extensions of the Standard Model suggest an enhanced branching ratio of $B_s^0 \to \mu^+\mu^-$ [11], for example for a large $\tan\beta$.

Chapter 2

Experiment

2.1 The Large Hadron Collider LHC

The Large Hadron Collider (LHC) at CERN, Geneva Switzerland is the most powerful ring accelerator worldwide. It was constructed from 1998-2008 and is in operation since September 10^{th} 2008. In a 27 km circumference tunnel, 100m below the surface, two symmetric proton beams of opposite direction are colliding at four experiment locations: LHCb, CMS, ALICE and ATLAS (see Figure 2.1). The nominal centre-of-mass energy of the LHC collisions is 14 TeV, which is about seven times more than the Tevatron accelerator at Fermilab Chicago. However until the end of the 2010–2012 running period the collision energy is limited to 7 TeV. The protons are accelerated in different stages before they reach the LHC: linear acceleration in the Linac2 to 50 MeV, then in the PS Booster to 1.4 GeV, in the proton synchroton to 25 GeV and in the super proton synchroton (SPS) to 450 GeV. The LHC uses the most powerful radiofrequency cavities for the acceleration of the proton bunches ($1.15 \cdot 10^{11}$ protons/bunch [12]) to 99.999999% of the speed of light. A variety of about 9600 magnets [12] contribute to the optimisation of the bunches and their trajectories. The collision rate is around 30 MHz for a maximum number of 2808 bunches with a bunch spacing of 25 ns [12]. Beside the protons also heavy ions (^{208}Pb^{+82} fully stripped lead ions [12]) are accelerated for the heavy ion program of ALICE, ATLAS and CMS.

2.2 The LHCb experiment

LHCb is a precision experiment for the detection of CP violating processes and rare decays of charm and beauty quarks. The $b\bar{b}$ quark pairs are mainly produced under small angles θ with respect to the beam axis (Figure 2.2). Therefore the LHCb experiment is designed as a forward spectrometer. Figure 2.3 shows a photo of the LHCb cavern with the LHCb detector. The angular acceptance of the detector system is 15–300 mrad horizontally and 15–250 mrad vertically. The covered

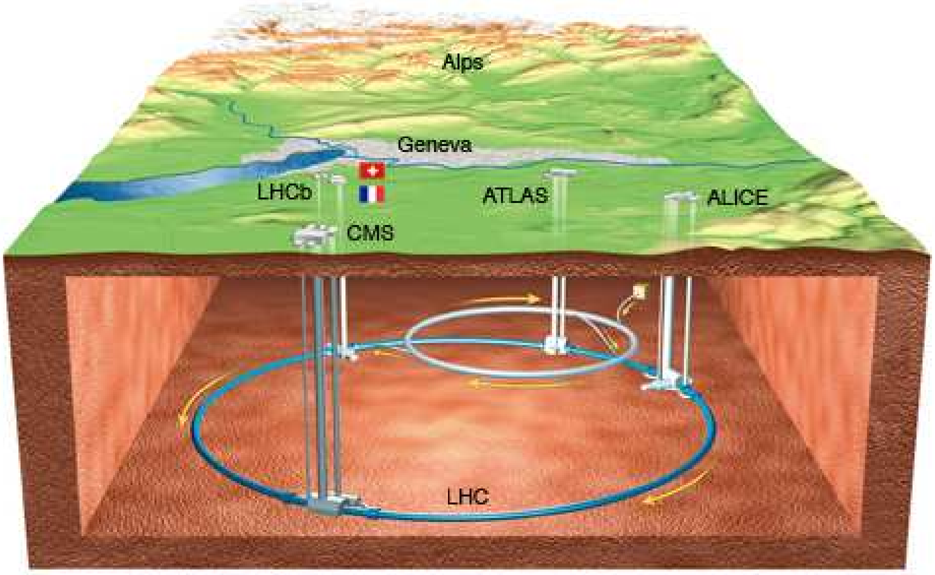

Figure 2.1: The LHC accelerator at CERN, Geneva, Switzerland, located about 100 m underground.

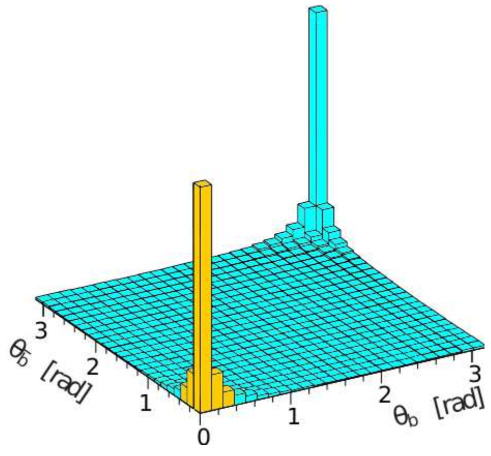

Figure 2.2: Correlation of polar angles θ_b and $\theta_{\bar{b}}$ of the flight direction of the B-hadrons, which fragmented from the same $b\bar{b}$ pair [13]. They are produced under small angles to the beam axis.

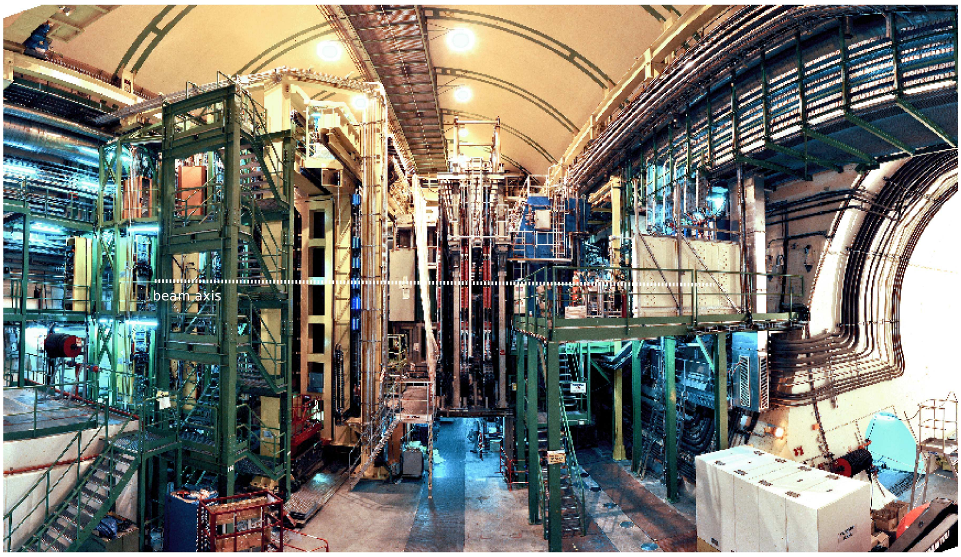

Figure 2.3: Photo of the LHCb cavern [14] with the LHCb detector, 100m underground. The beam-axis runs horizontally, the interaction point is at the right side, the muon system at the left side.

range in terms of pseudorapidity η is $1.9 < \eta < 4.9$, with η defined as:

$$\eta = -\ln\tan\frac{\theta}{2} \quad \text{with angle } \theta \text{ to the beam axis.} \tag{2.1}$$

In order to reduce the probability of more than one proton-proton interaction per collision, the beam is less focused for LHCb than for ATLAS and CMS. The result is a cleaner experimental signature.

The LHCb detector is about 10 m high, 20 m long and 10 m wide and weighs around 4500 tons. The coordinate system used within this document is right-handed with the z-axis pointing along the beam axis from the Vertex Locator towards the Muon Chambers and the y-axis pointing upwards. Figure 2.4 shows the top view of the LHCb detector with the interaction point at the left side as well as the interaction of the particles with the different sub-detectors and their trajectories.

The design of the LHCb experiment is optimised for the best possible mass resolution and vertex reconstruction. This is achieved by building the first detector of the tracking system around the collision point of the protons, placing the sensors very close to the interaction point. The tracking system consists of the Vertex Locator (VELO), the Tracker Turicensis (TT) upstream of the magnet, the Inner Tracker (IT) and the Outer Tracker (OT) downstream of the magnet. The IT and OT together form three planar tracking stations T1–T3. The particle identification is provided by two Ring Imaging Cherenkov detectors (RICH1 and RICH2) and the Muon Chambers M1-M5. The energy of the photons and electrons is measured by the electromagnetic calorimeter (ECAL) and the energy of hadrons with the

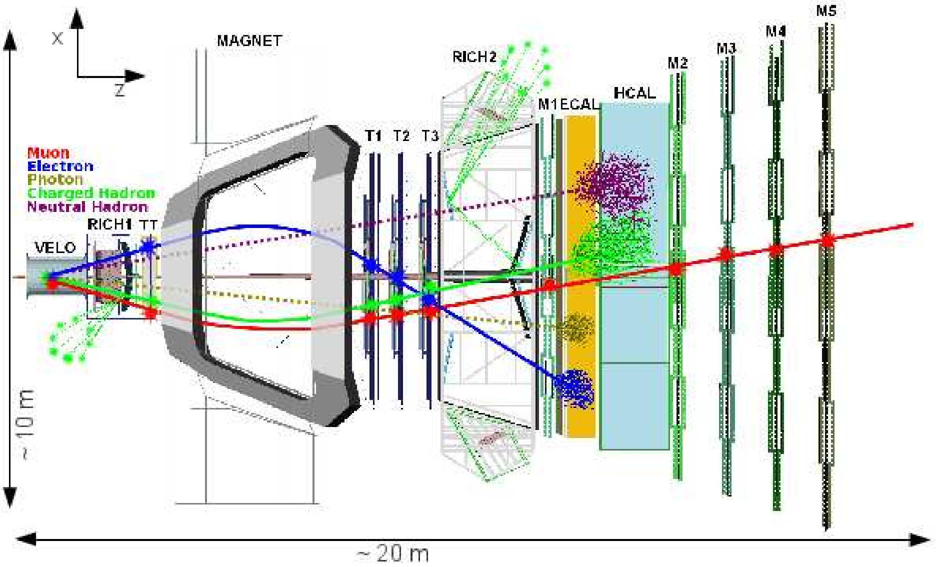

Figure 2.4: Top view of the LHCb detector with a muon, electron, charged hadron and a neutral hadron interaction. The coloured lines show the trajectories of a muon (red), an electron (blue), a photon (olive), a charged hadron (green) and a neutral hadron (violet) and their interaction with the different sub-detectors. The solid lines show the trajectories of charged particles which are bent by the magnet. The dashed lines show tracjectories of uncharged particles. [15]

hadronic calorimeter (HCAL). The calorimeters are also used to improve the particle identification. The Muon Chambers and the calorimeters provide information for the first trigger stage (L0 trigger).

2.3 Tracking System

The components of the LHCb tracking system are the VELO and four planar tracking stations: the TT and T1–T3. Silicon microstrip technology is used for the VELO, the TT and IT to cope with the high track multiplicity. The tracking stations T1–T3 consist of 2 detectors: the Inner Tracker in the cross-shaped central region around the beam pipe and the Outer Tracker covering the large area of the outer region (Figure 2.5). The OT is a gaseous drift-time detector with drift cells (straw tubes) of 4.9 mm diameter, providing a spatial resolution of about 200 μm. Both IT and OT employ four layers in the X, U, V, X2 layout which is explained in section 2.3.2. The LHCb dipole magnet consists of two coils - both weighing 27 tons - which are mounted inside a 1.45 ton steel frame. It is a warm (non-superconducting) magnet with an inhomogenous dipole field of 4 Tm bending power. The field polarity can be switched (magnet ’down’ and magnet ’up’).

Different track types are defined in the tracking system. A VELO track con-

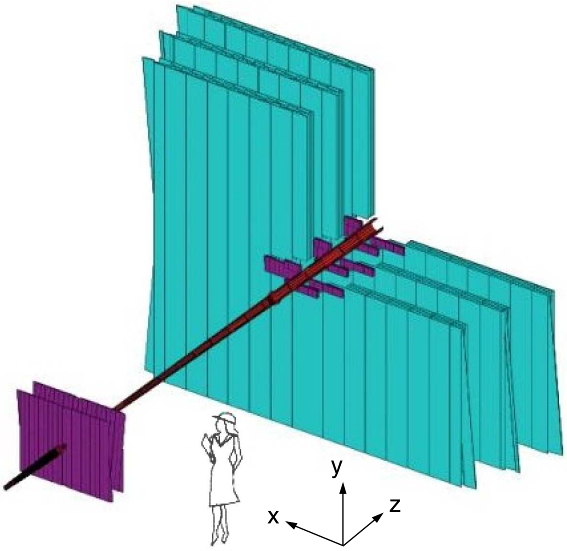

Figure 2.5: The tracking system after the VELO: TT and IT in violet and the Outer Tracker in blue.

sists of only hits in the Vertex Locator, upstream tracks have hits only upstream of the magnet: in VELO and TT. Downstream tracks have hits in TT and T1–T3 and for long tracks the hits from VELO, TT and T1–T3 are used. T tracks are reconstructed from hits in T1–T3 only. For the analysis mainly long tracks were used, since they provide the best vertex and momentum resolution. In an early stage of the analysis also downstream tracks were studied. The components of the tracking system are presented in the following chapters with a special emphasis on the Tracker Turicensis.

2.3.1 Vertex Locator

The Vertex Locator, VELO, is the first component of the tracking system. The sensors are placed as close as possible to the LHCb collision point. This allows a precise location of the primary and secondary vertices. The majority of b- and c-hadrons decay inside the VELO. The 84 half-moon-shaped silicon microstrip sensors are arranged along the z-axis opposite of each other (Figure 2.6). Each sensor provides a measure of the radial (r) or angular Φ coordinates. The sensor thickness is $300\ \mu$m. In the nominal position for stable beams the two opposite sensors are overlapping with a small opening for the beam in the centre. During beam injection the sensors are retracted by 3 cm to avoid radiation damage from the proton beams.

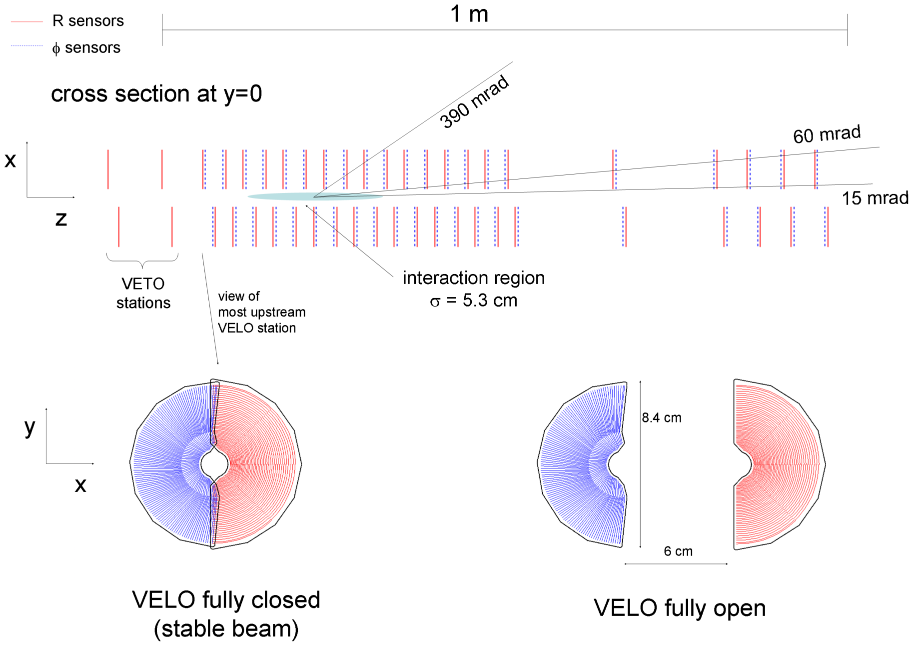

Figure 2.6: The half-moon shaped VELO sensors are arranged along the z-axis around the proton-proton interaction region. The sensors are retractable by 3 cm for beam injection. Modified from [16].

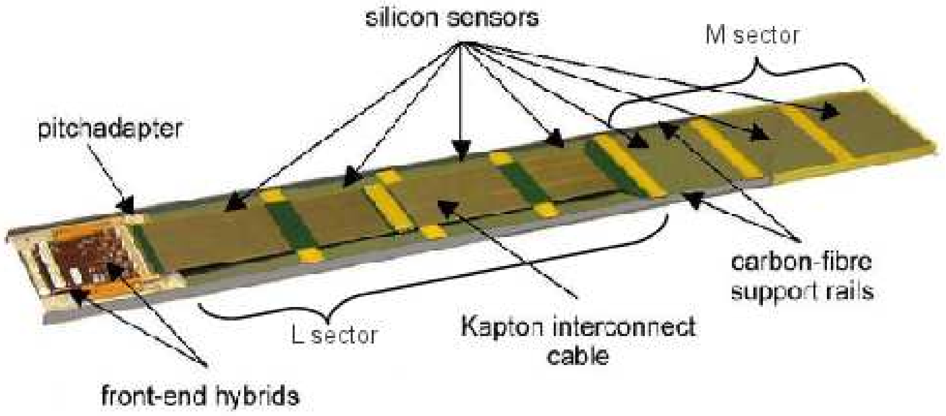

Figure 2.7: A silicon sensor half module of the Tracker Turicensis with the silicon micro strip sensors on the right side and the front-end hybrids on the left side.

2.3.2 Tracker Turicensis

The Tracker Turicensis is designed to improve the momentum resolution of particle trajectories. It is the third detector after the interaction point, located after the RICH1 and before the magnet.

The TT consists of p^+ in n doped, single sided silicon micro strip sensors. arranged in half modules (see Figure 2.7). Each sensor has 512 strips with a strip pitch of 183 μm. The TT consists of 143360 readout channels in total. Strips of up to four sensors are wire-bonded and read out together on one front-end hybrid, forming a readout sector. A readout sector with four sensors is called long sector (L), a sector with 2 or 3 sensors is called medium sector (M) and a readout sector with one sensor is a short sector (K). A long and medium sector together form a 4-3 type half module (Figure 2.7). A 4-2-1 type half module consists of a long, medium and short sector. The front-end hybrids are at one end of the half module assembled on top of eachother. The sensors from long sectors are directly wire bonded to the pitch adapter, which connects the channels with the Beetle [17] readout chips on the front-end hybrid. For the M and K sector a Kapton interconnect cable links the sensors to the pitch adapter. Hybrids from M sectors are assembled on top of L hybrids and K hybrids are arranged on top of M hybrids. Two half modules of the same type can be assembled to a module, stretching the full acceptance of the Tracker Turicensis in y-direction. Several modules and two half modules in the centre form a layer. The TT consists of four layers of silicon micro-strip sensors: the X1, U, V and X2 (Figure 2.8). The two layers in the centre (U and V) are inclined with a stereo angle of $\pm 5^\circ$. The X1 layer is closest to the RICH1 detector and the X2 layer is closest to the magnet. The V and X2 layer are equipped with more sensors than the X1 and U layer because of their larger distance from the collision point. With outer dimensions of about 160×130 cm the TT covers the full acceptance (Figure 2.9). LHCb wants to catch the tracks in the forward and very

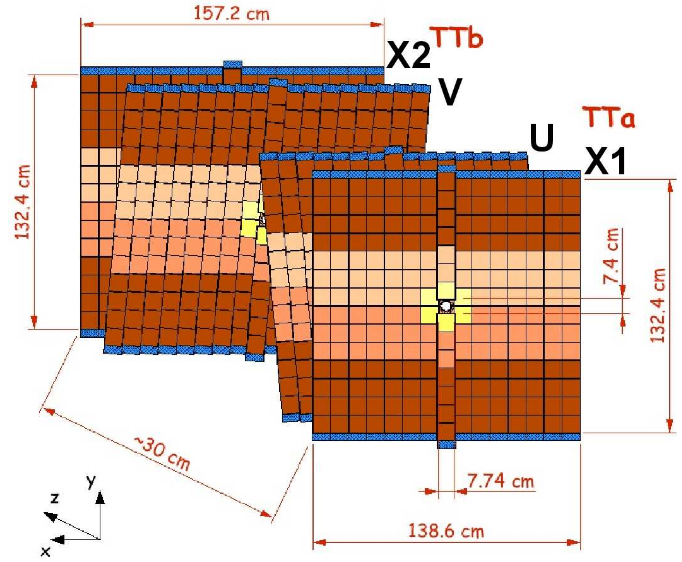

Figure 2.8: The TT consists of four layers of silicon: layer X1 (headmost) at $0°$ inclination, layer U with $-5°$, layer V with $+5°$ and layer X2 with $0°$ inclination. The shadings indicate the different readout sectors: in brown the L sectors, in orange the M sectors and in yellow the K sectors. Modified from [16].

forward region around the beam axis, therefore the layout of the TT is designed for an optimal coverage of the region around the beam pipe. Figure 2.10 shows a close up of the TT sensors in the central region, where they are as close as about 39 mm to the beam axis. To cope with the higher occupancy of the central sensors, the half modules in the centre are divided into three readout sectors instead of two. The layers are surrounded by a light-tight detector box. The detector box is constantly flushed with dry nitrogen to keep the humidity low. To dissipate the heat produced by the Beetle ASICs and to prevent radiation damage of the silicon sensors, the hybrids are attached to the support structure, which is attached to cooling plates. The cooling plates are connected to a C_6F_{14} cooling circuit. The C_6F_{14} cooling allows to keep the detector box volume at a temperature below $5°$ C. The TT was designed and built by the Physik-Institut of the Universität Zürich. After a pre-installation in Zürich and extensive testing, the detector was disassembled and transported to the LHCb cavern in December 2006. There it was reassembled and successfully commissioned until 2009. Table 2.1 gives an overview of the key parameters of the Tracker Turicensis.

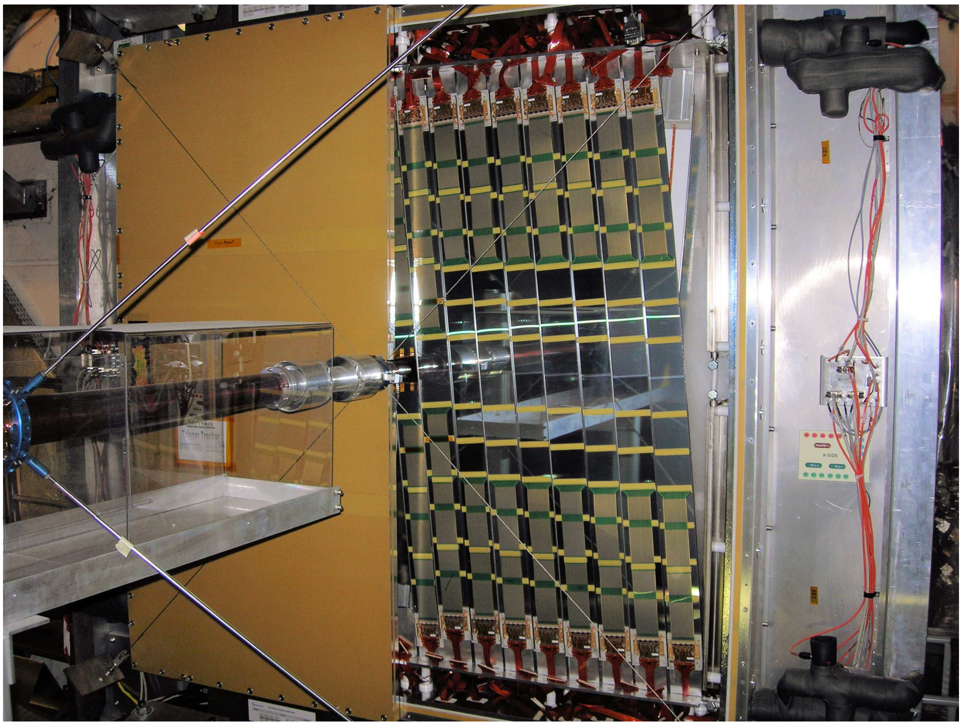

Figure 2.9: Subdetector Tracker Turicensis, seen from inside the magnet. On the left side the detector box is closed and on the right side the V layer is visible. It is inclined by 5°.

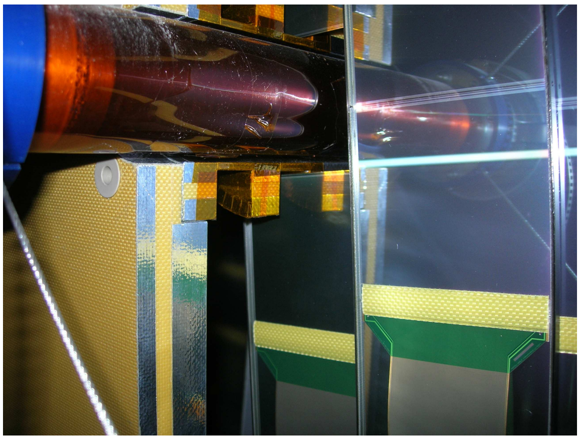

Figure 2.10: Close up of the sensors around the beam pipe, which is protected by red Kapton foil. The silicon sensors of the TT are as close as 15 mm to the beam pipe protection and have a distance of about 39 mm to the beam axis.

Table 2.1: Key parameters of the Tracker Turicensis

Total number of silicon sensors	896
Bulk material	n type
Implant	p$^+$ type
Number of strips per sensor	512
Strip pitch	183 μm
Sensor thickness	500 μm
Total number of readout channels	143360
Total number of readout chips	1120
Cooling medium	C_6F_{14}
Temperature of cooling fluid	-15° C
Operating temperature	-5° C
Total weight of the Tracker Turicensis	600 kg
Weight of the silicon	9.5 kg
Area of the silicon	7.8 m^2
Z-coordinates of the 4 silicon layers	[appendix I]
X1 layer	2331.75 mm
U layer	2368.25 mm
V layer	2601.75 mm
X2 layer	2638.25 mm

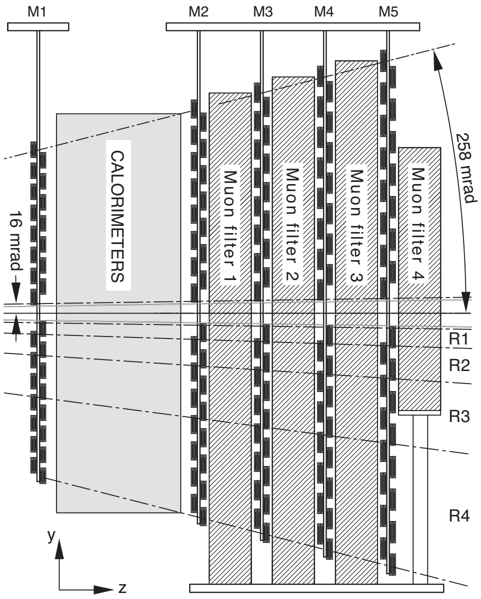

Figure 2.11: Muon stations M1-M5. The first MPWC (black) is in front of the calorimeters and the remaining ones are separated by iron (Muon filters $1-4$).

2.4 Muon System

The muon system is not part of the tracking system but plays an important role in identifying the muons. It is located at the far end of the LHCb detector. Standalone tracking is done with the five muon stations M1-M5 to provide a L0 trigger on high-p_T muons. The muon stations are a sandwich of multi-wire proportional chambers (MWPC) and 80 cm iron in between (Figure 2.11). In total the MPWCs are equipped with 2.5 million wires and the gas mixture consists of CO_2, argon and tetrafluoromethane. Muons with momenta > 6 GeV penetrate all five stations.

2.5 LHC Startup and Outlook

On September 10^{th} 2008 the startup of the LHC was celebrated with circulating proton beams. Unfortunately an incident [18] at September 19^{th} 2008 required a careful investigation and a lot of repair work. With these fixes a first running period with collisions of 450 GeV protons started on November 23^{rd} 2009. Over the Christmas break more repair work was achieved, making proton collisions with 3.5 TeV possible. A long run with this energy started with collisions on March 30^{th} 2010.

After the running period from 2010-2012 a long shutdown is planned. The interventions during the long shutdown will prepare the LHC to finally reach its nominal centre-of-mass energy of 14 TeV.

Chapter 3

TT Control and Safety System

The LHCb control system allows to process the data from the front-end devices to permanent storage. Figure 3.1 gives an overview of the control system which is divided in three main parts:

- The timing and fast control system (TFC) which is responsible for example for distributing the LHC clock and the L0 trigger commands to all the sub-systems.
- The data acquisition (DAQ) is responsible for processing the data from the front-end devices of the different sub-detectors to the permanent storage.
- The experiment control system (ECS) provides (slow-) control and monitoring of all the hardware components and protects them from incorrect use. The ECS maps the hardware in a well-arranged and clear way, to enable an effective handling of all devices.

The calorimeters and the muon chambers provide data for the L0 trigger decision unit. The L0 trigger reduces the 40 MHz rate of the bunch crossing to 1.1 MHz. The L0 trigger decision is sent from the decision unit to the TFC sytem, which distributes it to all the different sub-systems. The data is stored in the front-end devices until the trigger decision arrives. Upon a positive trigger decision the data is sent to the readout board (TELL1 [20]). The TELL1 performs for the TT for instance the pedestal subtraction, common-mode noise subtraction and zero-suppression and executes the cluster[1]-finding algorithm. The positions and ADC values of the clusters are sent to the high level trigger CPU farm. The high level trigger uses the full physics information from all subdetectors to reconstruct the events and reduces the rate for permanent storage to about 2 kHz. This corresponds to about 10^{15} bytes per year [20].

First a description of the silicon micro-strip detector and its readout chain is given in section 3.1. Then the detector mapping and the bias voltage mapping of the sensors (high voltage, HV) is described in section 3.2. This mapping is

---

[1] The definition of a cluster is given in section 4.2.1.

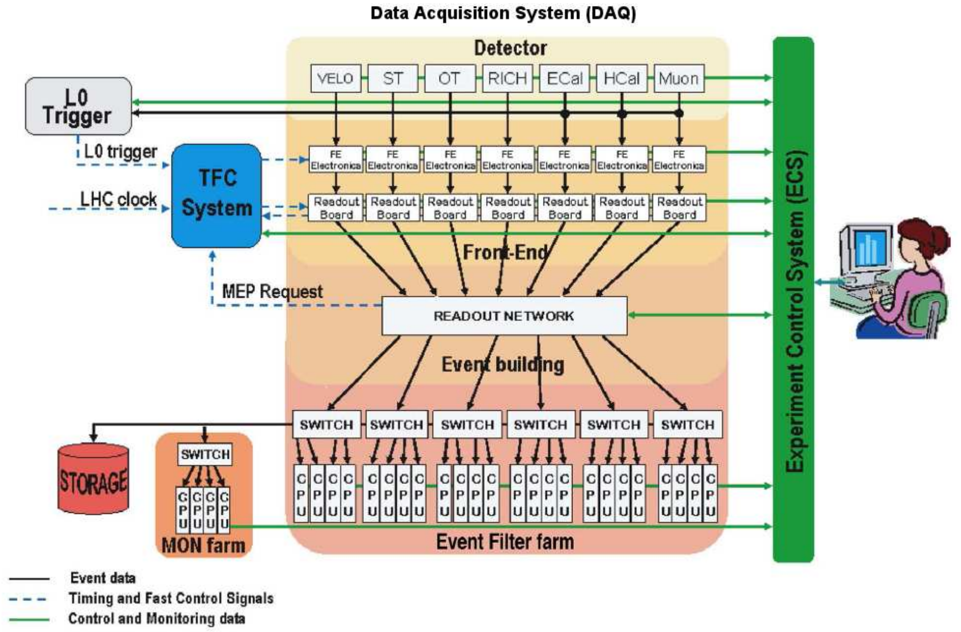

Figure 3.1: The LHCb readout system with its main components and interactions: the timing and fast controls, the data acquisition and the experiment Control System. From Ref. [19].

an important element in the design of the slow control and an example of the slow control hierarchy is given in section 3.3. To monitor the status of the detector many environmental parameters are recorded. Alarms and actions are implemented to protect the detector and to guarantee save operation. They will be presented in section 3.4.

3.1 Readout System

The cross section of a sensor is shown in Figure 3.2. It consists of a n-type bulk with implanted p^+-strips on the front side and an aluminum layer on the backside. On top of the p^+-implants a SiO_2 layer separates the aluminum stripes covering the implant. The aluminum stripes are wire-bonded to the Beetle chip of the front-end readout electronics. A reverse bias voltage of around 250 V is applied between the p^+-implants and the aluminumised backside, where the p^+-implants are connected to ground. With a depletion voltage of around 200 V [22] the TT sensors are over depleted because of the faster electron-hole collection time.

A charged particle passing a sensor ionises the bulk along its trajectory and creates a number of electron-hole pairs. The holes drift towards the p^+-implants and the charge is collected at the aluminum strip electrodes, which are connected to the input of the chip. The charge is amplified and shaped by the Beetle chip and a

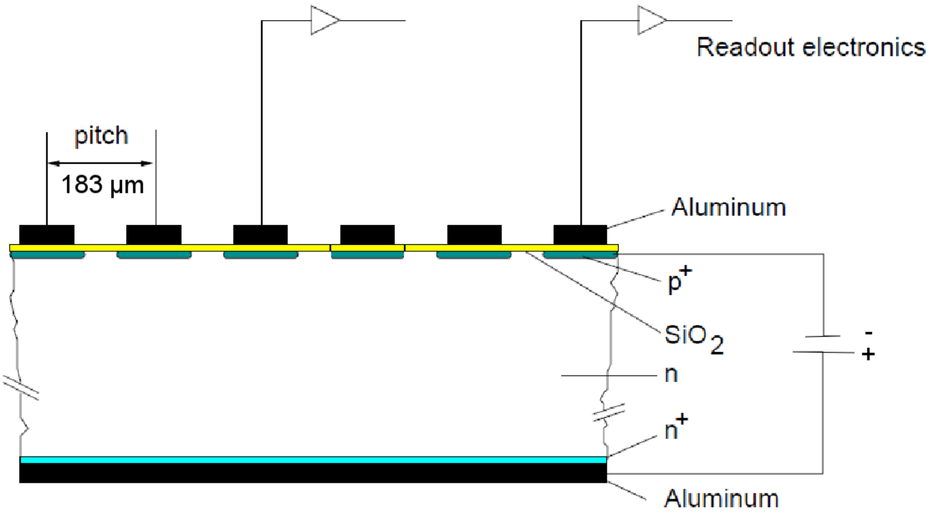

Figure 3.2: Schematic cross section of a p^+ on n silicon micro-strip sensor. Modified from Ref. [21].

voltage proportional to the generated charge is stored on a sample and hold circuit until the L0 trigger decision arrives. A group of four Beetle chips is mounted on one front-end hybrid at the end of a silicon module (Figure 2.7).

Each front-end hybrid is connected with a thin Kapton cable via a patch panel and a 8 m long readout cable to a digitiser board (see Figure 3.3). Each service box is hosting 12 digitiser boards and one control board. The analogue signals from the chips are received at the digitizer board and digitised in the ADC. The digital data stream is encoded according to the Gigabit Ethernet protocol by the CERN GOL ASIC [24]. After encoding, the signal is modulated by a 850nm VCSEL diode and the optical fibres of 3 digitiser boards are bundled to 12 fibre cables. From the service-box the bundled optical fibres transmit the signal about 60–70 m to the TELL1 board on the other side of the thick concrete wall which shields all the sensitive electronics from radiation. The TT is geographically divided in four quadrants: access-shaft side top part (AT), access-shaft side bottom part (AB), cryogenics-side top part (CT) and cryogenics side bottom part (CB) (Figure 3.5). In each quadrant a tower of 6 service boxes hosts the digitiser- and control boards. More details on the complete readout can be found in Ref. [23].

The control board in the service box is responsible for detector control and monitoring and provides interfaces to the ECS and the TFC system. Figure 3.4 shows a picture of the control board with its different components. It is connected to the digitiser boards through the backplane of the service box. The backplane is equipped with the low voltage (LV) regulators for the digitiser boards. The TTCrx chip in the TTCrq of the control board receives the LHC clock, timing- and the trigger signals from the TFC system. The serial protocol for the ECS of LHCb is called SPECS. A SPECS master (in the counting house) can communicate with several

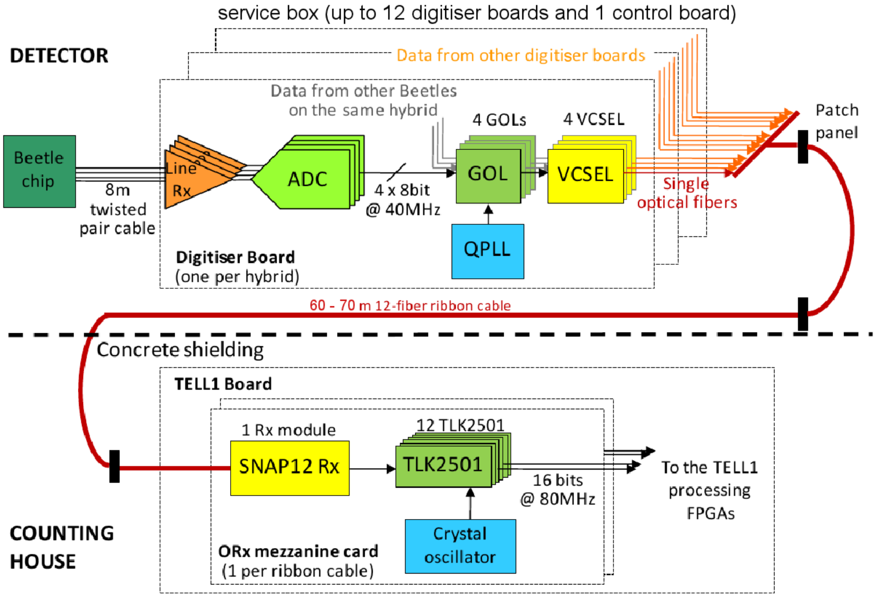

Figure 3.3: Schematic of the TT readout chain. From the Beetle readout chip on the front-end hybrid the analogue signal is routed to the service box. There it is digitised by the ADC, encoded by the GOL ASIC and converted to an optical signal by the VCSEL. Then it is sent via optical fibres to the TELL1 board behind the concrete shielding wall. Modified from Ref. [23].

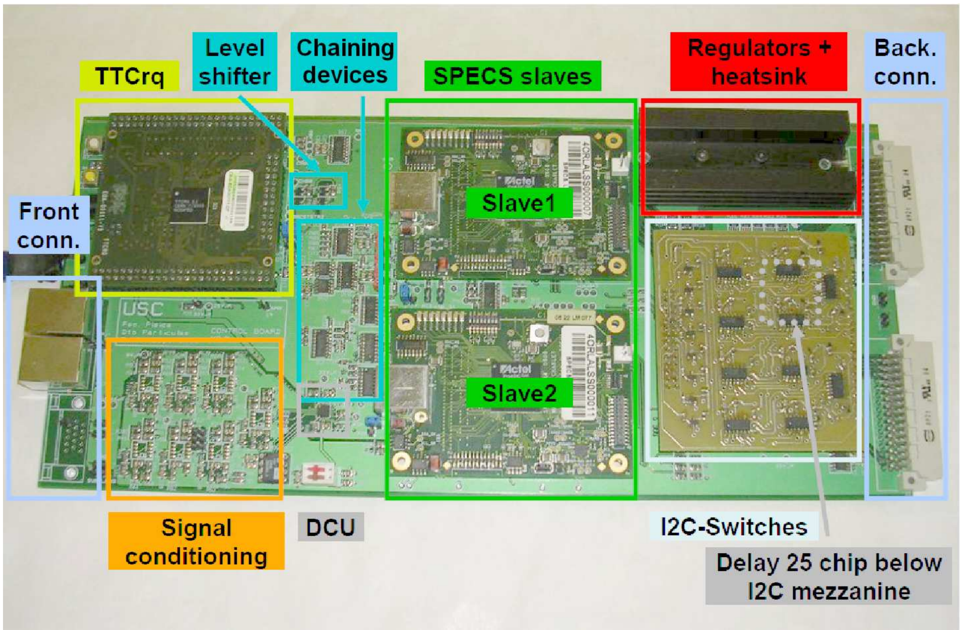

Figure 3.4: Picture of the control board with its different components. Modified from Ref. [23].

SPECS slaves. Two SPECS slaves are on each control board and each quadrant (6 control boards) shares a SPECS master. Each SPECS slave provides 4 I^2C-buses which are used to communicate with the GOL- and the Beetle chips. Each slave provides a detector control unit (DCU) [25]. They are used to monitor detector box temperatures, backplane temperatures and control board power regulator voltages. A third DCU, directly on the control board, is used for reading out a HMX2000 humidity sensor in the detector box. A delay25 chip provides phase delay of digital signals. The backplanes are equipped with the LV regulators for the digitiser boards of the service boxes. The backplanes and the control board regulators are cooled by the LHCb mixed-water cooling circuit.

3.2 Detector mapping and HV distribution

The Tracker Turicensis consists of four layers of silicon sensors, as described in section 2.3.2. Each layer is divided into three regions, A (Access), B and C (Cryo): the A-region is closest to the access shaft of the cavern, the B-region is in the centre and the C-region is closest to the cryogenics in the cavern (see Figure 3.5). The division into these three regions is due to the following constraints: a service box or a TELL1 must belong to only one region, a TELL1 must belong to only one layer, the minimum number of TELL1s (48) is not exceeded.

Each half module is divided in 2 to 3 readout sectors (as explained in section

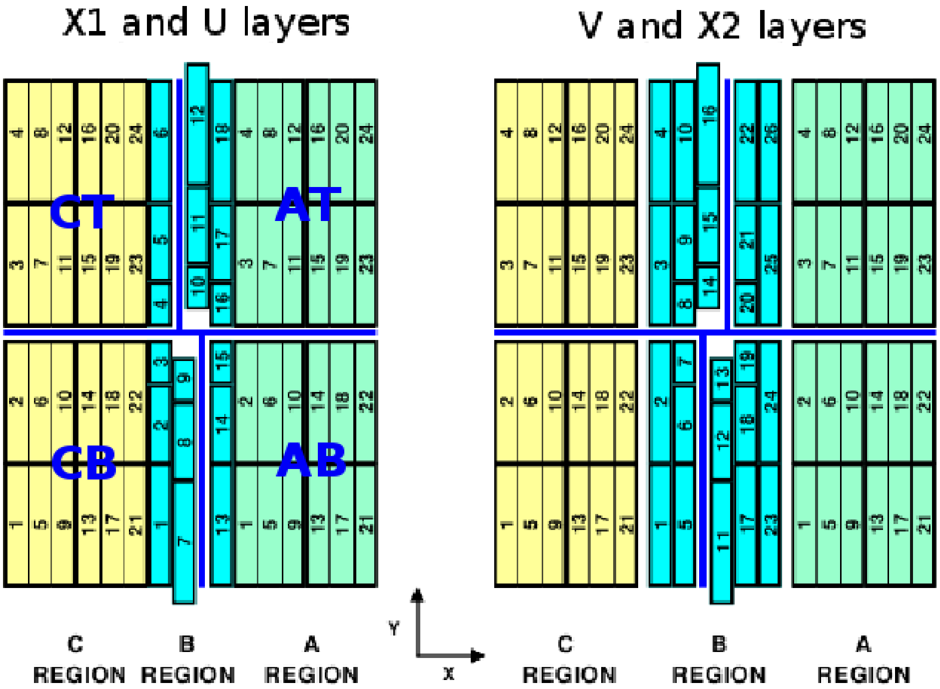

Figure 3.5: Partitioning of the TT. The numbers indicate the readout sectors and the colors green, blue and yellow the regions A, B and C. The quadrants are labeled in blue and the HV partitions are separated by bold black lines. Modified from Ref. [23].

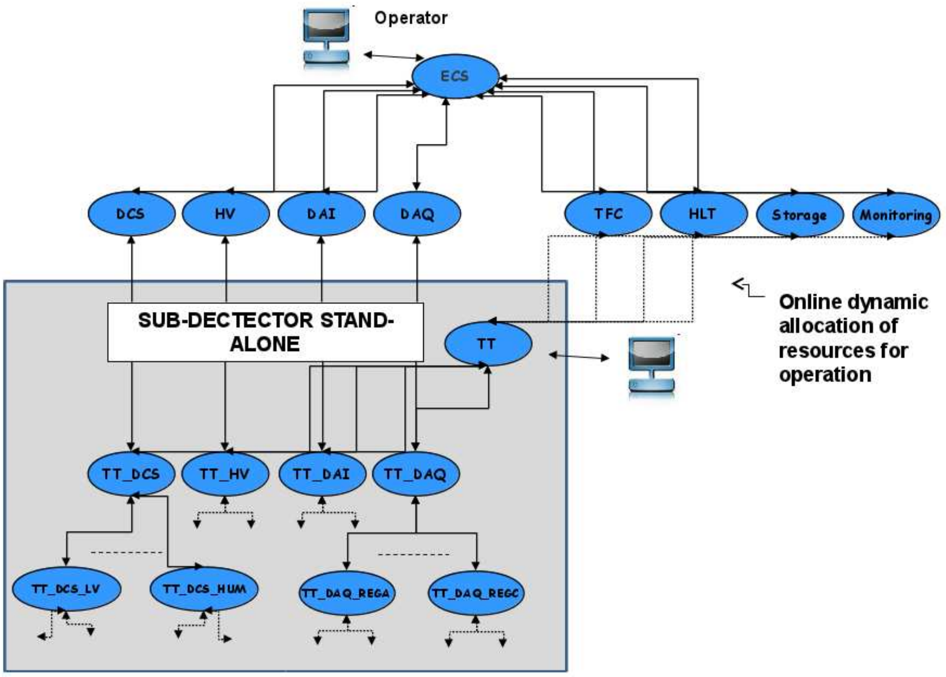

Figure 3.6: The ECS hierarchical structure. The four common domains for LHCb DCS, HV, DAI and DAQ are sub domains of the top node ECS. Below these four common domains the individual subdetector structure is deployed. Each subdetector system can run standalone for commissioning or integrated for LHCb data taking. From Ref. [23].

2.3.2) with each readout sector corresponding to one front-end hybrid. The central B-region has a more dense supply net for HV. Due to the higher radiation exposition of the central sensors, the HV needs to be adjustable per readout sector and not only per group of three sectors as in the A and C regions. Groups of readout sectors which are supplied by the same HV and LV channel are called partitions. The numbering scheme of these readout sectors and the HV partitions are presented in Figure 3.5. More details about the readout partitioning can be found in Ref. [26].

3.3 TT Slow Control

The ECS is a distributed control system of Finite State Machine (FSM) domains and has a highly hierarchical structure. It provides simple tools for an operator to configure detector components and to monitor the relevant environmental parameters. Furthermore the ECS can perform automatic actions to ensure save running. The ECS is based on the commercial PVSS [27] tool for supervisory control and data acquisition (SCADA). For the implementation of the FSMs the SMI++ [28] toolkit was used.

The Finite State Machine domains or subdomains are arranged in a tree-like hierarchical structure. The domains are distributed over several computers running on different platforms. A description of the ECS hierarchy with special focus on the TT hierarchy is given in Figure 3.6. For the TT the tree structure is built of two types of nodes: the control unit (CU) and the device unit (DU). The DU is used for physical devices and the CUs are abstract nodes. The CUs are used to group the DUs or other CUs in a sensible way. Each node is a Finite State Machine. The ECS node is the top domain of the whole system. The ECS node has four sub domains which are common for all subdetectors: DAQ, DCS, DAI and HV, where DAQ stands for data acquisition, the DCS includes the electronics supply voltages, monitoring of currents, temperatures and humidities, DAI refers to data acquisition infrastructure and HV to high voltage. Below these four common nodes the individual FSM structure of each subdetector is deployed. The individual FSM structure maps the physical layout of the subdetector hardware components and sub systems. Figure 3.7 shows the TT specific hierarchy of FSMs.

An example for a FSM of the data acquisition is presented in Figure 3.8 and shows the states of the domain and the actions. The possible states are NOT_READY, UNKNOWN, ERROR, CONFIGURING, READY and RUNNING. The possible actions are ’Recover’, ’Configure’, ’Reset’, ’Start’ and ’Stop’. In Table 3.1 the description of the different states is given for a DAQ device unit and in Table 3.2 the states are described for a DAQ control unit. The FSMs propagate actions from the top of the hierarchy downwards to the DUs. The DUs on the other hand propagate their state to the top domain. FSMs allow centralised and decentralised actions. Both features are necessary: the centralised part is important for controlling and monitoring the whole experiment and the decentralised part is needed when commissioning subdetector components. Logic behaviour can be implemented in CUs, such that for example power supplies are switched-on before the data acquisition can be configured. More details to the ECS and all the TT domains can be found in Ref. [23].

3.4 Environment parameters, Alarms and Detector Safety

To guarantee safe operation many hundred parameters of the TT are monitored. They are divided into environmental parameters, power supply parameters and voltage regulator measurements. The monitored environmental parameters for the Tracker Turicensis are: front-end hybrid temperatures measured by a platinum resistance temperature sensors PT1000s close to the Beetle readout chip, detector box temperatures and humidities with PT1000s and HMX sensors[2], the temperatures of the service box backplanes and the control board temperatures. Based on the humidity and the temperature measurements in the detector box the dew point is calculated and monitored to prevent condensation. Figure 3.9 provides a list of

---

[2] The detector box temperatures and humidities are measured at many locations (see Ref. [29] for the exact locations).

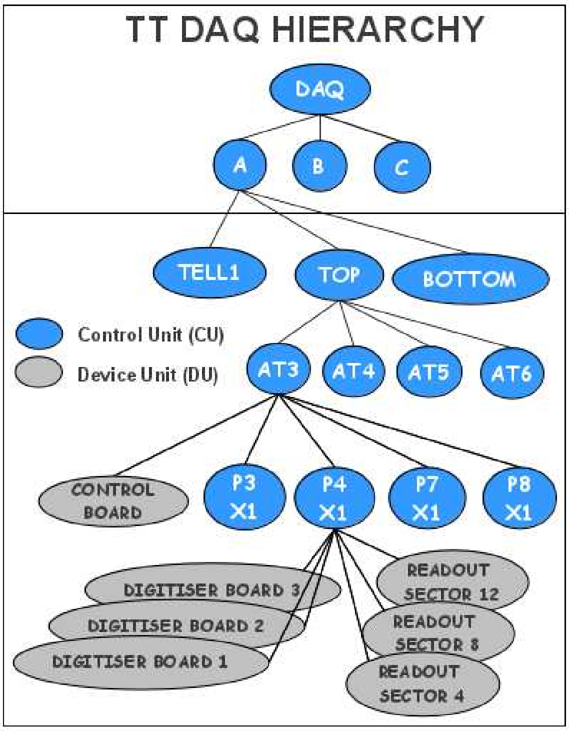

Figure 3.7: Example of the hierarchical tree structure for the TT DAQ. The first division is in the regions A, B and C. Below each region the TELL1s are a separate domain and the detector is divided into its top and bottom part. The next level are the service boxes containing the control board and low voltage partitions as sub domains. The digitizer boards and the readout sectors are sub domains of the LV partitions and represent the bottom of the tree as device units. The first two levels of the hierarchy run on a different computer than the rest.

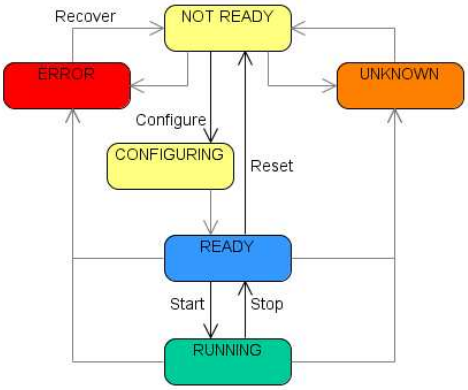

Figure 3.8: An example of a Finite State Machine from the data acquisition. The possible states are NOT READY, UNKNOWN, ERROR, CONFIGURING, READY and RUNNING which are propagated in the hierarchy from bottom up. The actions are ’Recover’, ’Configure’, ’Reset’, ’Start’ and ’Stop’ and are propagated from the top node downwards. From Ref. [23].

Table 3.1: DAQ state description for device units. From Ref. [23].

UNKNOWN	It is not possible to communicate with the device. No information about the device is available and no command can be applied to it. This can happen for example if a ’driver’ process is dead.
NOT_READY	The device is under the control of the ECS but it needs to be configured before it can be used.
READY	The device is ready to take data. For example the ’Start’ command clears some counters.
RUNNING	The device is fully configured and taking data. Its configuration cannot be changed while in this state. For this the device must be stopped and reconfigured.
ERROR	The device has detected an error which means it is not able to take valid data.

Table 3.2: DAQ state description for control units or logical units. From Ref. [23].

UNKNOWN	At least one of the sub domains is in state UNKNOWN.
NOT_READY	At least one of the sub domains is in state NOT_READY or sub domains are in mixed states, for example some are READY and some are RUNNING.
READY	All sub domains are in state READY.
RUNNING	All sub domains are in state RUNNING.
ERROR	At least one of the sub domains is in state ERROR.

the monitored parameters with the corresponding alert ranges. The temperatures are monitored every 90 s and the humidity and the dew point every 60 s. More details on the power supply parameters and voltage regulator measurements can be found in Ref. [23].

An alert panel in the control room allows the shift leader to react to the different error messages from all subdetector systems. To prevent the alert panel from flooding with error messages due to single faulty readings, a recovery mechanism was implemented in the ECS hierarchical logic. For example the DU will only go to error when the measurement reading is 5 consecutive times[3] out of the operational range. An SMS service reports directly to the on-call and subdetector expert. This happens for example when a cooling plant is in NOT_READY state.

Two important issues of detector safety for the Tracker Turicensis are: condensation and radiation damage of the silicon sensors. The condensation issue is relevant, once the detector is cooled to temperatures below the dew point of the cavern. Under these circumstances the temperature and humidity monitoring must be guaranteed at all times, such that the shifter can react to a rising dew point within time. In addition the hybrids should be kept switched-on to prevent condensation at the front-end electronics. In case of a mixed-water cooling failure, the readout devices in the service box are stopped and the readout of temperatures and humidities can no longer proceed. Then the detector has to be warmed up by changing the C_6F_{14} temperature to $+15^\circ$ C to prevent condensation. This brings up the second issue about the radiation damage of the silicon sensors. To minimise radiation damage in the irradiated sensors their temperature is kept below 5° C by the C_6F_{14} cooling circuit. The warm up of the detector box is therefore only a short term option.

The heat exchanger of the C_6F_{14} cooling plant depends on the mixed water cooling circuit. In the case of a mixed water cut, a backup cooling plant (backup chiller) is in place, which supplies cooling water in a separate circuit for the heat exchanger of the C_6F_{14} cooling plant. The backup chiller itself dissipates the heat

---

[3] In this case the measurement is repeated every second.

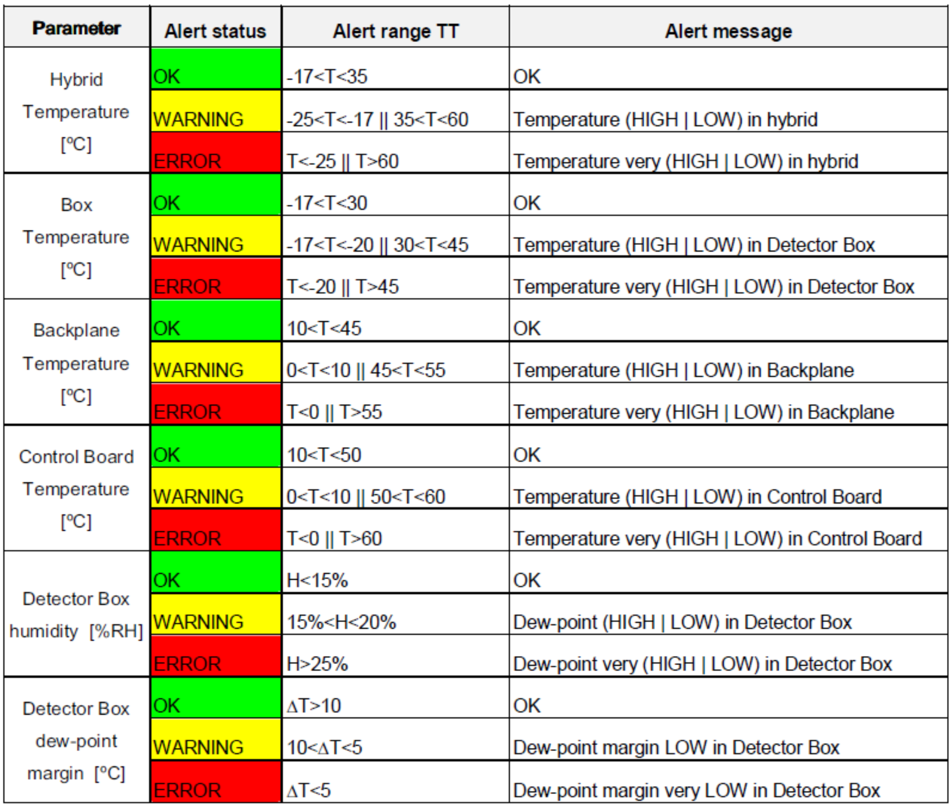

<table>
<tr><th>Parameter</th><th>Alert status</th><th>Alert range TT</th><th>Alert message</th></tr>
<tr><td rowspan="3">Hybrid Temperature [ºC]</td><td>OK</td><td>-17<T<35</td><td>OK</td></tr>
<tr><td>WARNING</td><td>-25<T<-17 || 35<T<60</td><td>Temperature (HIGH | LOW) in hybrid</td></tr>
<tr><td>ERROR</td><td>T<-25 || T>60</td><td>Temperature very (HIGH | LOW) in hybrid</td></tr>
<tr><td rowspan="3">Box Temperature [ºC]</td><td>OK</td><td>-17<T<30</td><td>OK</td></tr>
<tr><td>WARNING</td><td>-17<T<-20 || 30<T<45</td><td>Temperature (HIGH | LOW) in Detector Box</td></tr>
<tr><td>ERROR</td><td>T<-20 || T>45</td><td>Temperature very (HIGH | LOW) in Detector Box</td></tr>
<tr><td rowspan="3">Backplane Temperature [ºC]</td><td>OK</td><td>10<T<45</td><td>OK</td></tr>
<tr><td>WARNING</td><td>0<T<10 || 45<T<55</td><td>Temperature (HIGH | LOW) in Backplane</td></tr>
<tr><td>ERROR</td><td>T<0 || T>55</td><td>Temperature very (HIGH | LOW) in Backplane</td></tr>
<tr><td rowspan="3">Control Board Temperature [ºC]</td><td>OK</td><td>10<T<50</td><td>OK</td></tr>
<tr><td>WARNING</td><td>0<T<10 || 50<T<60</td><td>Temperature (HIGH | LOW) in Control Board</td></tr>
<tr><td>ERROR</td><td>T<0 || T>60</td><td>Temperature very (HIGH | LOW) in Control Board</td></tr>
<tr><td rowspan="3">Detector Box humidity [%RH]</td><td>OK</td><td>H<15%</td><td>OK</td></tr>
<tr><td>WARNING</td><td>15%<H<20%</td><td>Dew-point (HIGH | LOW) in Detector Box</td></tr>
<tr><td>ERROR</td><td>H>25%</td><td>Dew-point very (HIGH | LOW) in Detector Box</td></tr>
<tr><td rowspan="3">Detector Box dew-point margin [°C]</td><td>OK</td><td>ΔT>10</td><td>OK</td></tr>
<tr><td>WARNING</td><td>10<ΔT<5</td><td>Dew-point margin LOW in Detector Box</td></tr>
<tr><td>ERROR</td><td>ΔT<5</td><td>Dew-point margin very LOW in Detector Box</td></tr>
</table>

Figure 3.9: Monitored environment parameters with the corresponding alert ranges and alert messages.

to the cavern. The radiation damage issue is solved in this case by the backup chiller. However, the temperature and humidity monitoring is not running continually, since the electronic equipment of the service boxes cannot be cooled. An option is the manual monitoring in short intervalls, by switching-on the electronics only for a short time, to measure the temperature and the humidity, and then switch it off again. Since the hybrids at the front-end electronics are not powered in this scenario, the danger of condensation at the hybrids persists.

Another possible scenario is the complete failure of the C_6F_{14} cooling plant. That implies the front-end electronics is stopped and the repair of the cooling plant is initiated instantly.

The two worst case scenarios are a long term failure of the mixed water cooling system and/or a complete long term failure of the C_6F_{14} cooling plant. That means the front-end electronics is at higher condensation risk and the sensors are prone to radiation damage.

3.4.1 Detector safety system DSS

In addition to the PVSS software based ECS, a decoupled, hardware based detector safety system, DSS, protects the hardware components from destruction. The DSS is completely independent from the experiment control system ECS and takes action to protect the hardware from human errors, component failures and ECS software failure. Dedicated sensors are installed at the critical devices. The following DSS alarms protect the TT [23]:

1. **Thermo-switches for the detector boxes and the service boxes:** thermo-switches are installed in the detector box (one per quadrant) and on the backplane cooling block of each service box. The DSS cuts the power to the detector in case of an overheating.

2. **Mixed water flow switch and temperature switch for service boxes:** the service boxes are cooled using the LHCb common mixed water system. An alarm is triggered in case of a problem with the mixed water cooling (no flow or temperature above $25°$C for more than 5 s). An additional flow switch detects whether there is water flow in the cooling circuit of the service boxes. The DSS cuts the electrical power of the affected equipment.

3. **Water leak detection:** a detection cable is installed in a collecting tray below the service boxes. The DSS powers off the low voltage and high voltage power supplies and cuts the cooling water to the equipment.

4. **Nitrogen flow switch:** the flushing of the TT detector box with nitrogen is measured by two flow switches. If the Nitrogen stops for longer than 30 minutes the Cern Control Center needs to be called to take care of this problem. If the situation is not re-established before 8 hours, the temperature of the C_6F_{14} cooling plant needs to be increased to prevent condensation in the detector box. The DSS will only send an alarm for the operator to take an action.

5. **C_6F_{14} cooling PLC[4] Signal:** in case of a problem with the detector cooling plant, the controlling PLC provides an open contact and after a delay of 30 s the power of the detector is cut.

6. **High Voltage door switches:** to protect the sensors from sudden HV disruptions, doors with switches are installed in front of HV power supplies (located in the counting house). The DSS triggers a fast ramp down of the HV (emergency off).

7. **Smoke Sniffer System for the detector:** a signal is given by the Sniffer System PLC in case of smoke detection around the detector. It will trigger a power cut.

---

[4] Programmable Logic Controller

All the mentioned DSS alarms have a delay of 30 s before any action is taken. Further DSS alarms concern the racks with the electronic equipment behind the concrete shielding wall. They are described in Ref. [23].

Chapter 4

Commissioning

The commissioning and debugging of hard- and software was an important step after the installation of the detector components as well as the tuning of operational parameters.

In section 4.1 the opportunities for commissioning during beam injection tests are described. The optimisation of timing settings before the first proton-proton collisions are described in section 4.2. Sections 4.3 and 4.4 present two selected commissioning problems: one about oscillating temperature measurements and one related to the cooling of the control board. In section 4.5 some lessons learned during the commissioning are summarised. For more information about commissioning and lessons learned see Ref. [30].

4.1 Injection tests

LHCb is a forward spectrometer dealing with horizontal tracks. Therefore it is difficult to calibrate the tracking system with cosmic rays due to their angular distribution. Calibration with cosmic rays is partially possible for the muon system, the outer tracker and for the calorimeters, but not for the silicon tracking system. However, LHC injection tests provided a good opportunity for a first timing calibration. With these so called TED-runs, LHCb obtained some early experience with the tracking system before real LHC proton-proton collisions.

Data were collected during LHC injection tests in September 2008 and June 2009. Bunches of $2–5 \cdot 10^9$ 450 GeV/c^2 protons [31], coming from the SPS (section 2.1) as shown in Figure 4.1, were injected in the beam injection line to the LHC. The beam was stopped at the end of the injection line in a tungsten beam stopper (TED), located about 350 m behind the LHCb detector (Figure 4.2). The dumped proton bunches produced secondary particles (~ 10 GeV/c muons) traversing the LHCb detector from the opposite direction compared to particles emerging from the LHCb interaction point. The particles were used for timing studies and spatial alignment. of the

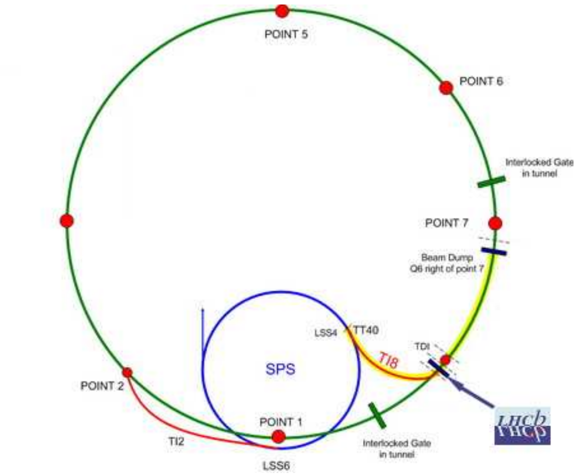

Figure 4.1: The protons from the SPS (blue) are fed to the LHC (green) via the injection line TI8.

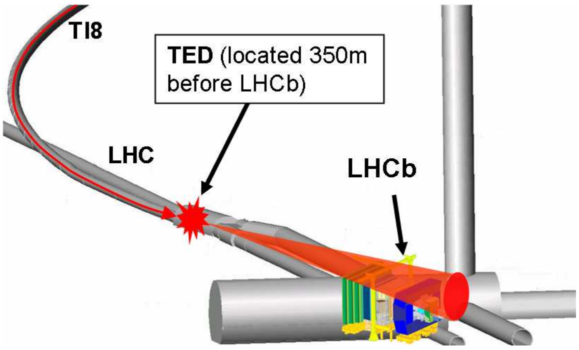

Figure 4.2: Injection Line TI8 with the beam stopper TED.

4.2 Timing settings

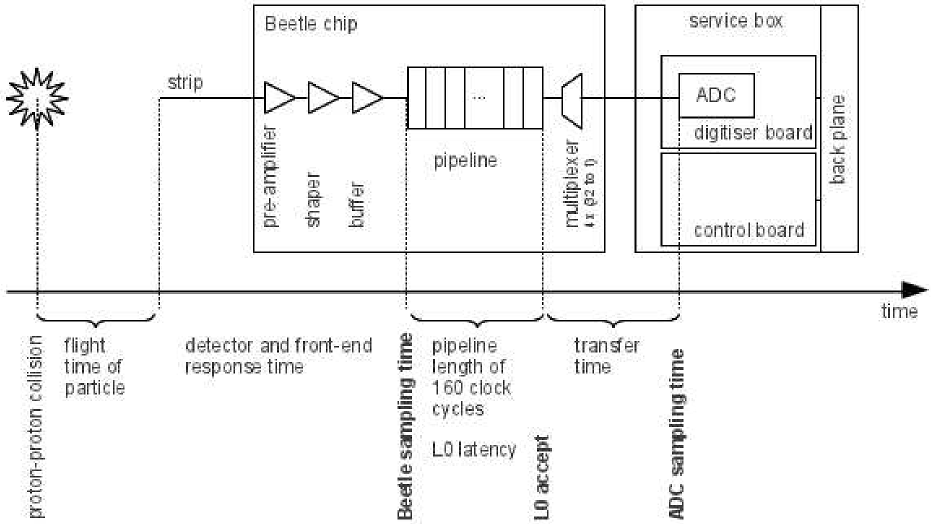

Figure 4.3: Overview of the relevant signal sampling points for the timing settings. The time axis is not in scale.

The injection tests were used to optimise the timing settings of the Tracker Turicensis. Figure 4.3 shows a sketch of the first part of the signal path. After the proton-proton collision the flight time, the detector response time and the front-end response time determine the sampling point (Beetle[1] sampling time) of the shaped detector signal. The optimisation of the Beetle sampling time is described in section 4.2.1. Then the signal is stored in the Beetle pipeline. When the L0 trigger decision (L0 accept) arrives at the Beetle, the content of the corresponding pipeline column is multiplexed and sent to the ADC. Section 4.2.2 describes the trigger signals and the evaluation of their optimal delay. The conversion time in the ADC (ADC sampling time) was tuned with calibration pulses. The synchronisation of the calibration pulses with the Beetle sampling time is discussed in section 4.2.3 and the calibration of the ADC sampling time in section 4.2.4.

4.2.1 Beetle Sampling Time

For an optimal signal-to-noise ratio, the Beetle sampling time is adjusted to the moment, where most of the signal is seen at the input of the Beetle pipeline. Figure 4.4 shows the signal amplitude as a function of time from a channel, where a particle has passed. The fine delay of ClockDes1 (Beetle clock) was used for

---

[1] The readout chain with the Beetle chip is described in section 3.1.

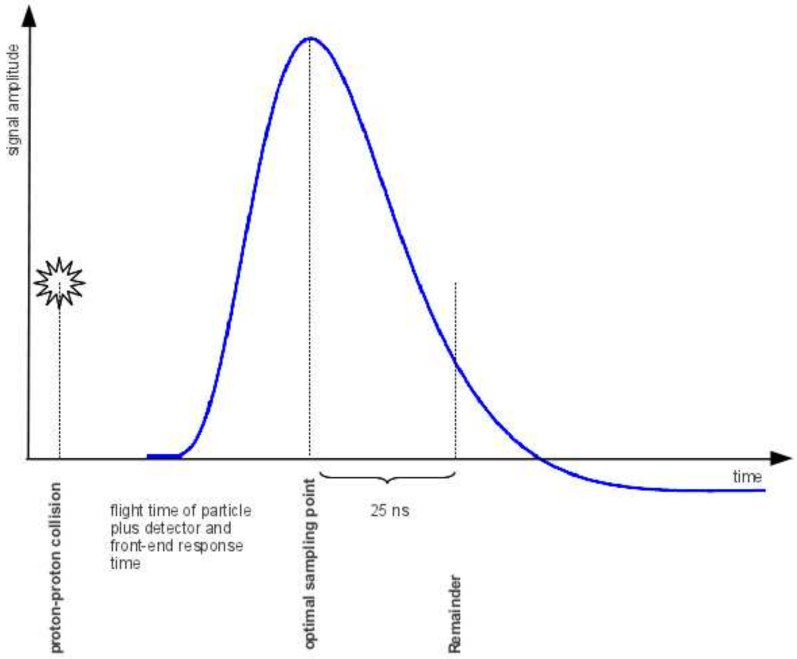

Figure 4.4: Analogue signal of one silicon micro-strip channel after the pre-amplifier and the shaper. The time axis is not in scale. Modified from Ref. [17].

tuning the Beetle sampling time to the maximum signal amplitude. ClockDes1 is one out of two 40 MHz clocks, which are provided by the TTCrx component of the control board (Figure 4.5 and section 3.1). It can be adjusted in a range of 25 ns in 240 steps of 104.17 ps. Further information about this fine delay can be found in the appendix A of the TTCrx manual [32].

The probability distribution function of the energy loss of a particle, passing through silicon sensors, follows a Landau-Vavilov-Bichsel shape [34]. A particle induces a signal on one or two channels. Due to cross talk in between the readout strips and in the Beetle readout chip up to 4 channels can measure a signal above the noise threshold [35]. These channels are called a cluster. The energy loss of a particle is measured by the total charge in a cluster (see Figure 4.6). The most probable value (MPV) of the cluster charge was scanned individually for each service box to account for the different flight time and detector and front-end response time. A range of different delays of the Beetle clock was scanned in steps of 5 ns (Figure 4.7). The Beetle sampling time was set to the fitted maximum of the scanned MPVs.

MPVs from consecutive bunch crossings, but with the same fine delay, were used to find the central bunch crossing, which aligns all the subdetectors in time. Consecutive bunch crossings were also used to determine the amount of signal left over from the previous bunch crossing (called remainder, see Figure 4.4).

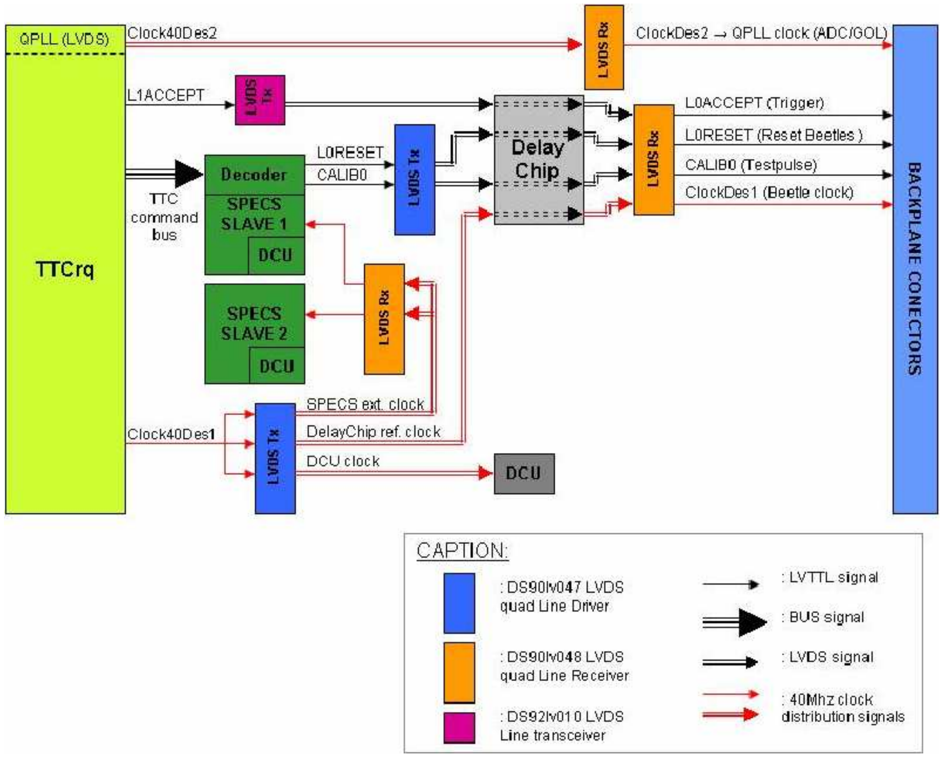

Figure 4.5: Timing signal distribution of the control board [33]. ClockDes1 and ClockDes2 are fine tuned in the TTCrx component of the TTCrq. The calibration signal (CALIB0) for the calibration pulse is delayed in the SpecsSlave (coarse delay) and the Delay25 chip (fine delay). The delay of the L0 accept signal is adjusted as well in the Delay25 chip. From Ref. [33].

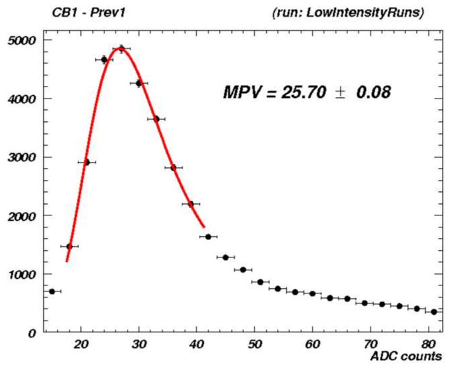

Figure 4.6: Histogram of measured charge per cluster at injection tests in 2009.

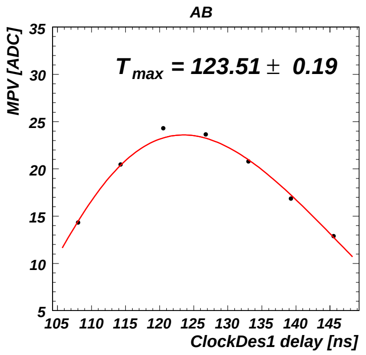

Figure 4.7: Most probable value (MPV) of Landau distributions (Figure 4.6) for different delays.

4.2.2 L0 Accept and L0 Reset Signal

The L0 trigger (section 2.2) takes the first decision, whether an event is worth to be read out and digitised. In case of a positive decision the L0 accept signal is sent to the front-end electronics (Beetle). The latency of the L0 trigger decision is defined as the time between the proton-proton collision and the arrival of the L0 accept signal at the front-end electronics [36]. The latency of $4\ \mu$s corresponds to 160 clock cycles of 25 ns and defined the length of the Beetle pipeline. The L0 reset signal is used to reset the pipeline column number (PCN) for the full subdetector.

The delay of the L0 reset and the L0 accept signal was adjusted such that they are not too close to the edge of the Beetle clock (Figure 4.8). Otherwise a desynchronisation of one clock cycle could be introduced by jitter and leads to errors in the TELL1. The L0 accept and reset signals can be fine-delayed in a range of 32 ns in steps of 0.5 ns in the Delay25 chip on the control board (Figure 4.5). Delay scans were performed in steps of 0.5 ns.

The adjustment to the correct bunch collision is done using the coarse delay of the L0 accept signal in the TTCrx. In a range of 15 clock cycles (375 ns in steps of 25ns) the coarse delay allows to choose the correct bunch collision.

The delays depend on the length of the optical fibres which carry the trigger signals. The scans were therefore performed for each service box individually.

4.2.3 Synchronisation of the Calibration Pulse Signal

For detailed system tests there is the possibility to send a calibration pulse (CALIB0) to the input of the Beetle preamplifier. The injection time of the calibration pulse needs to be optimised for best (calibration pulse) signal-over-noise with respect to the the Beetle sampling time. The calibration signal can be adjusted independent of the Beetle sampling time. On the control board, the SPECS slave 1 (Figure 4.5) provides the possibility of a coarse delay up to at least 16 clock cycles and the

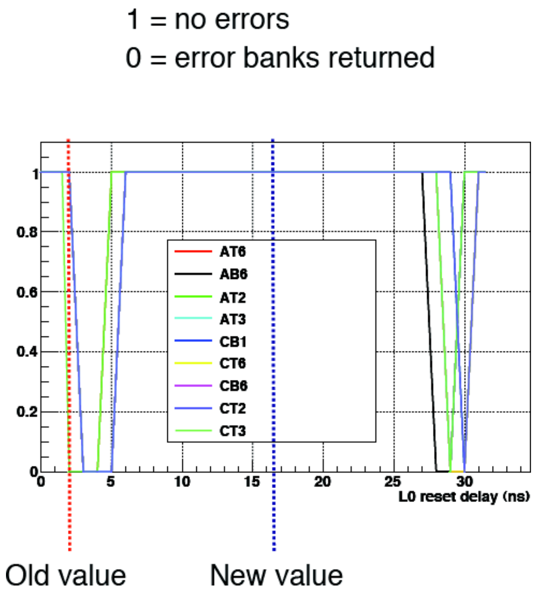

Figure 4.8: L0 reset delay scan for different service boxes.

Delay25 chip offers again the fine delay in steps of 0.5 ns in a range of 32 ns. The Specs slave 1 needs half a clock cycle to decode the calibration signal. Therefore the calibration signal arrives 1 clock cycle later at the Beetle than the L0 accept signal.

By scanning through the coarse- and fine delay of the calibration pulse in steps of 2 ns (Figure 4.9), the test pulse shape was determined.

4.2.4 ADC Conversion Time

Upon the L0 accept signal the content of the pipeline column is sent to the multiplexer. The multiplexed signal is composed of a header and the analogue signals of 32 Beetle channels as shown in Figure 4.10. The header bits are pseudo-binary: they can only be in state 1 or 0. This signal is sent to the digitiser board, where the analogue-to-digital conversion is executed. The ADC sampling time was adjusted such that it avoids the transition phases of the multiplexed signal.

The ADC sampling uses ClockDes2, the second clock provided by the TTCrx component of the control board. It is adjustable the same way as ClockDes1 (section 4.2.1). In order not to loose the optimal Beetle sampling time, the Beetle clock and ClockDes2 were shifted together. The ADC samples at the positive or negative edge of the clock (programmable).

The optimal ADC sampling time was determined by injecting a calibration pulse to every 8th channel on the Beetle. The signal at the ADC was scanned for the pulsed channel and its two neighbouring channels (see Figure 4.11) to see the full shoulders of the signal in the pulsed channel.

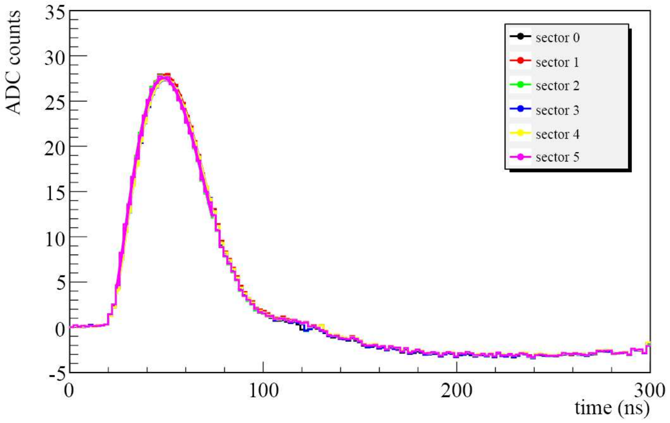

Figure 4.9: Delay scan for the calibration pulse signal. The maximum indicates the best injection time with respect to the Beetle sampling time.

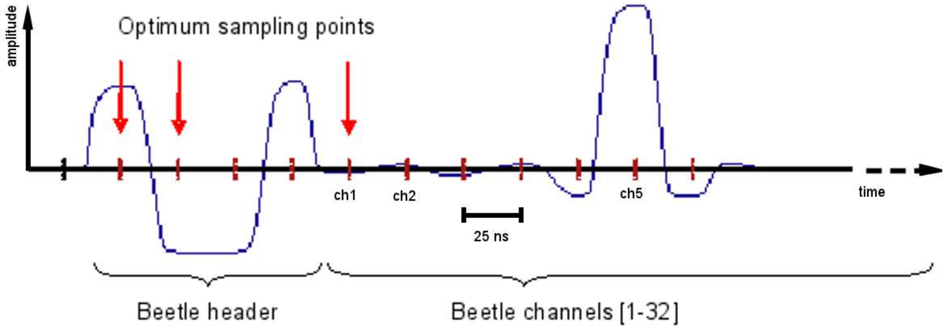

Figure 4.10: Digitizer board input signal coming from the multiplexer with optimal sampling points. Modified from Ref. [33].

Since the signal had a broad plateau, the precise timing was not too delicate. The scan was performed in steps of ~ 0.5 ns. It allowed to adjust the ADC sampling time such that the central channel is selected at the centre of the plateau, in safe distance to the transition phases.

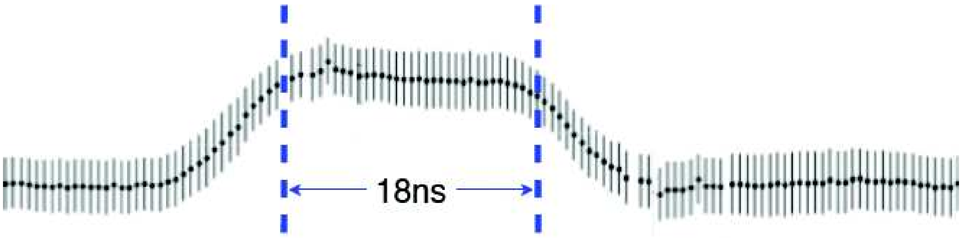

Figure 4.11: ADC delay scan of 3 channels. The central channel had the calibration pulse injected. The signal from the calibration pulse forms a broad plateau of about 18 ns. To see the full transition phases the neighbouring channels were scanned in addition. The scan was performed in steps of ∼0.5 ns.

4.3 Oscillating Temperature Measurements

during the commissioning the problem of oscillating temperature measurements is described. It has been described already in Ref. [30] where more details can be found. On each of the front-end hybrids of the Tracker Turicensis a PT1000 measures the temperature near the Beetle chip. The PT1000 temperature sensor is read out by a DCUF slow control ADC [25] on the digitiser board. The problem showed up as an oscillating behaviour of the read out ADC values (Figure 4.12) after the service boxes were installed in the cavern. An overvoltage on one of the input channels of the ADC was the cause for its malfunctioning. The voltage divider, for the input voltage of the ADC, was not correctly dimensioned. Therefore

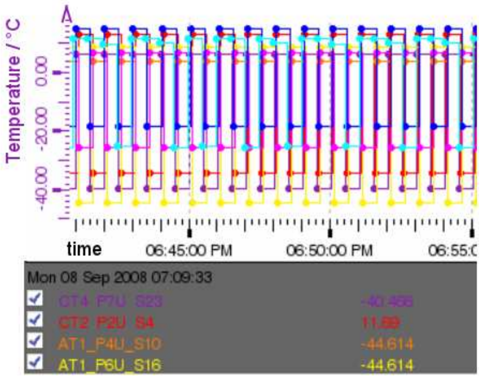

Figure 4.12: Oscillating temperature measurements of the PT1000 on the hybrid.

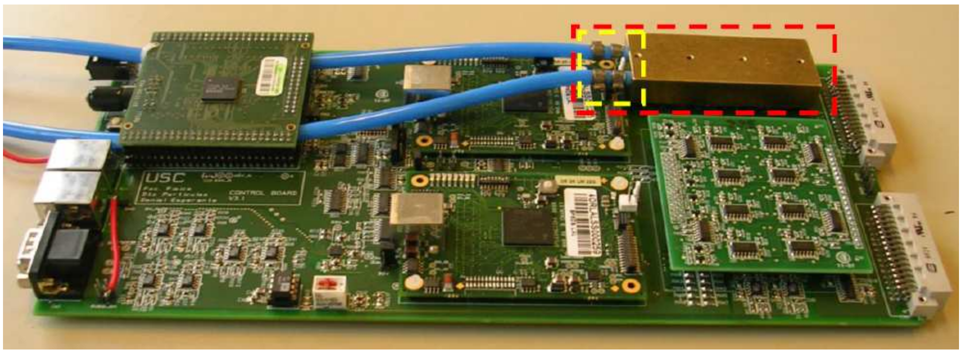

Figure 4.13: Control board with glued copper block to the regulators (red frame). The connection to the cooling circuit was done via polyurethane hoses clamped to the sockets of the copper block. From Ref. [23].

the divider was corrected by replacing a 1 kOhm with a 2.2 kOhm resistor which cured the problem.

4.4 Control Board Regulator Cooling and Colour Changing Hoses

Another problem concerned the control board regulator cooling. In Ref. [23] this problem has been described already and more details can be found therein. The LV regulators of the control board (see section 3.1) were overheating in the cavern. Although lab tests showed sufficient cooling under lab conditions the passive heat sinks on top of the regulators could not dissipate enough heat in the final setup under the full load. In the final setup the control boards are in a fully equipped service box together with 12 digitiser boards and six service boxes are stapled in a tower. Since the lifetime of electronics decreases when operated at elevated temperature, it was decided to glue a water-cooled copper block on top of the LV regulators. The copper blocks were connected to the water cooling circuit with polyurethane (PU) hoses and were fixed with one clamp at the sockets of the copper block. Figure 4.13 shows the connection of the hoses to the copper block but in the evolved version featuring two clamps at the joints.

Before the installation of the water cooled copper block, the supply conditions were carefully clarified. The pressure drop at the inlet was specified as 7 bar and that of the outlet as 5 bar. The pressure drop was more than sufficient to generate a sufficient flow rate for an efficient cooling of the regulators. To reduce the pressure on the joints between the hoses and the copper blocks, a pressure reducer was installed in the water cooling supply line.

During the first operation a severe water leak was observed, coming from the joints between the hoses and the copper block. The waterleak caused damage to the control board which required a drying procedure and the change of some electronic

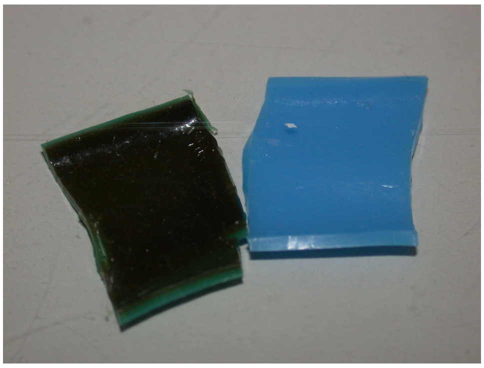

Figure 4.14: Inside of a used PU hose (left) and new PU hose (right). The diffused dark material entered the hose as can be seen in the cross section.

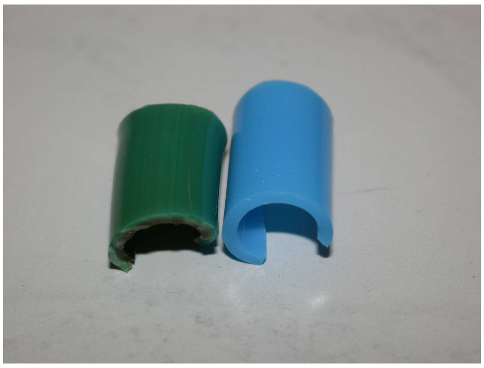

Figure 4.15: Outside of a used PU hose (left) and a new PU hose (right).

components on the board. The cause of the leak was overpressure. The pressure reducer did not prevent the overpressure, as it was mounted in the wrong direction due to miscommunication. After this incident the pressure reducer was mounted correctly, a second clamp was installed at the joints, the connection was sealed with Araldite and tested for leak-tightness up to 10 bar (Figure 4.13).

After more than 9 months of successful operation, the polyurethane hoses had changed their colour from light blue to dark green (see Figures 4.14 and 4.15). Therefore the cooling water and the hoses were investigated for a possible destructive chemical reaction and deteriorated leak-tightness of the hoses. For the cooling water and the PU hoses a deposit analysis[2] was commissioned to find the cause of the colour change. In the cooling water a large amount of Fe_2O_3 residue — rust — was found. By diffusion the Fe_2O_3 was able to enter the PU hoses. Over time the Fe_2O_3 molecules might replace the filling molecules of the hose degrading its reliability over time. Therefore the PU hoses were replaced by copper pipes as can be seen in Figure 4.16.

4.5 Lessons learned

The following list presents a collection of lessons learned from my own experience during the commissioning phase.

- Avoid quick and dirty solutions under stress, the lack of testing can seriously damage persisting equipment.
- A change of any design needs a recalculation of the affected system(s), to check if it still can full-fill the specifications or if further modifications are needed.

---

[2] The results of the deposit analysis can be found in appendix J

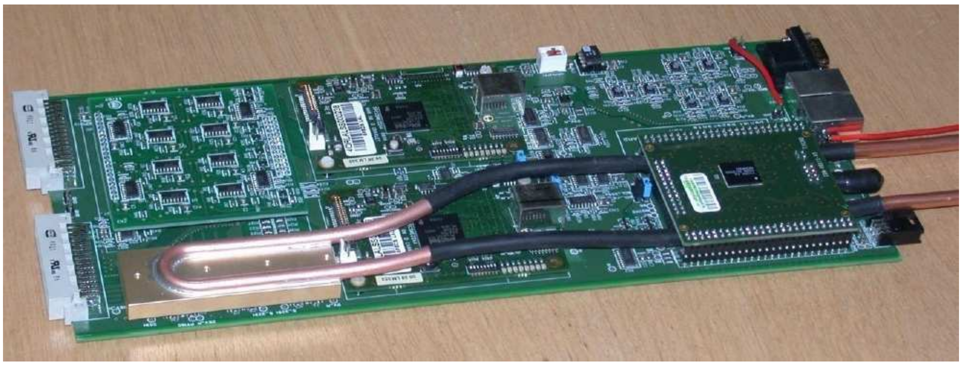

Figure 4.16: Control board with the final regulator cooling where the connection of the cooling block with the cooling circuit is done by copper pipes. From Ref. [23].

- Test the system as complete as possible. Many of the errors occurred because some components (for instance the cables) were not available for integrated testing beforehand.
- Make the testing ground as similar as possible to the real installation, this includes orientation of the devices, height differences, temperature, cooling, ventilation, cable length, movements, etc.
- Have the documentation ready before commissioning, wrong hardware settings are much easier to find then.
- Store the components the same orientation as they will be assembled in the final setting to avoid problems due to different effects of the gravitational force.
- Use robust connectors which are not prone to loose contact. Even if you expect them to be plugged and unplugged only a few times, in reality it is 100 times more during commissioning to find all the bugs.
- Include all the details in the CAD design.

A design of the hardware with easy accessible and replaceable components allowed in situ modifications and made the commissioning efficient. The optimal settings could only be found in the final setup and under full load tests. Wrong hardware settings or a change in design were the most common difficulties. Complex problems with several causes sometimes added up to strange effects. These were the most challenging problems and the ones staying unsolved the longest.

Chapter 5

Analysis of $B_s \to \mu^+\mu^-$

The mass resolution studies in this thesis are motivated by the context of the search for the decays $B_s^0 \to \mu^+\mu^-$ and $B_d \to \mu^+\mu^-$. A precise measurement of the branching ratio is an interesting probe for new physics as described in chapter 1. The first LHCb analysis of these two decays was based on 2010 data and was published in Ref. [2]. This chapter gives an overview over the $B_s^0 \to \mu^+\mu^-$ analysis and the determination of a limit on the $B_s^0 \to \mu^+\mu^-$ branching ratio. The goal of the presented analysis is to rely as little as possible on simulated data, i.e. to determine the key parameters of the analysis from data. Different methods to estimate the mass resolution of the B-meson from data were applied and are discussed with more emphasis.

5.1 Analysis strategy

An overview of the $B_s^0 \to \mu^+\mu^-$ analysis strategy is given in this section. Loose selection cuts are applied on discriminating variables and the identification of muons, to reduce the size of the data sample to be analysed (section 5.2). The limit on the branching ratio is determined relatively to three normalisation channels, whose branching ratios are precisely known (section 5.3). The remaining events after the loose selection are binned in two dimensions: in a geometrical likelihood variable (GL) (section 5.4) and in invariant mass (IM) (section 5.5). The IM and GL distributions for signal are determined from other similar decays. For the determination of the background distributions invariant mass sidebands are used. In each two-dimensional bin the distribution of the expected number of signal and background events is estimated and compared to the observed distribution. The compatibility of each branching ratio hypothesis is tested for the observed distribution leading to an upper limit on the $B_s^0 \to \mu^+\mu^-$ branching ratio (section 5.6). For this compatibility check the 'modified frequentist' method CL_s [37] is used.

The search window in the two-dimensional bins of IM and GL was blinded (Figure 5.1) until the analysis procedure was completely defined.

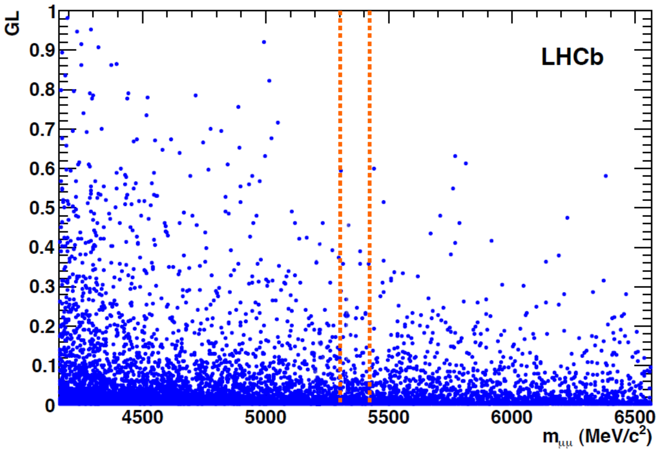

Figure 5.1: Distribution of selected events in invariant mass and geometrical likelihood. The orange-dashed lines indicate the search window of ± 60 MeV around the B_s^0 mass. From Ref. [2].

5.2 Event Selection

The first step in the analysis is the reduction of the data sample by cuts on a number of discriminating variables. The selection cuts are kept as similar as possible for signal and normalisation channels.

Two well reconstructed tracks are required, which must form a good secondary vertex (SV) and is well separated from the primary vertex (PV). Bad track combinations are rejected. If more than one PV is found, the PV with minimum impact parameter significance with the reconstructed momentum vector (flight direction) of the B-meson is chosen. The PV is re-fitted — excluding the signal tracks — before variables depending on the PV position are calculated. In addition, the flight direction of the B meson has to point back to the PV. To identify a muon track, one or more hits in the muon stations M2-M5 are required, depending on the track momentum [38]. A mass cut of ± 60 MeV around the B_s^0 meson mass is applied for the $B_s^0 \to \mu^+\mu^-$ search window.

After this selection cuts, the dominant background is due to $b\bar{b} \to \mu\mu X$, where the b and the $\bar{b}$ both decay semileptonically [2, 39]. A smaller background contribution (around 10%) are pairs of a real muon and a misidentified hadron. Background from $B_q^0 \to h^+h^-$, where both hadrons are misidentified as a muon is negligible in the mass window of ± 60 MeV around the B_s^0 mass.

5.3 Normalisation

The branching ratio can be defined as:

$$BR(B_s^0 \to \mu^+\mu^-) = \frac{N_{\mu\mu}}{2 \cdot f_s \cdot \mathcal{L} \cdot \sigma_{b\bar{b}} \cdot \epsilon_{\text{Total}}} \tag{5.1}$$

where $N_{\mu\mu}$ is the number of signal events. f_s is the fragmentation fraction of a b-quark to an B_s^0-meson, $\mathcal{L}$ the integrated luminosity, $\sigma_{b\bar{b}}$ the total $b\bar{b}$ cross section and ϵ_{Total} the total efficiency including the detector acceptance. The luminosity and the total cross section have a large systematic uncertainty.

A different approach is the normalisation of the branching ratio to well measured channels, such that the uncertainties of the luminosity and the cross section cancel out to first approximation:

$$BR(B_s^0 \to \mu^+\mu^-) = \frac{f_q}{f_s} \cdot \frac{\epsilon_X^{\text{total}}}{\epsilon_{\mu\mu}^{\text{total}}} \cdot \frac{N_{\mu\mu}}{N_X} \cdot BR(B_q \to X) \quad . \tag{5.2}$$

f_q is the fragmentation fraction of a b-quark to a B_s^0, B_d or B^+ meson (q stands for u- or d-quark). Subscript $\mu\mu$ refers to the daughter particles of the signal channel and subscript X refers to the daughter particles of the normalisation channel. ϵ^{total} stands for the total efficiency, N is the number of measured candidates and $BR(B_q \to X)$ is the precisely measured branching ratio of the normalisation channel. The total efficiency is the product of the reconstruction efficiency, the selection efficiency, the efficiency of the global event cuts[1] (GEC) and the trigger efficiency:

$$\epsilon^{\text{total}} = \epsilon^{\text{REC}} \cdot \epsilon^{\text{SEL}} \cdot \epsilon^{\text{GEC}} \cdot \epsilon^{\text{TRIG}} \quad . \tag{5.3}$$

The reconstruction efficiency ϵ^{REC} contains the geometrical detector acceptance, material interactions and the tracking efficiency.

In Equation 5.2, the fragmentation fractions, the efficiencies, the number of measured candidates of the normalisation channel and the branching ratio of the normalisation channel are merged to a normalisation factor $\alpha_{B_s^0 \to \mu\mu}$, which is calculated for all three normalisation channels individually:

$$BR(B_s^0 \to \mu^+\mu^-) = \alpha_{B_s^0 \to \mu\mu} \cdot N_{\mu\mu} \tag{5.4}$$

The three normalisation channels are:

- $B_u^+ \to J/\psi(\mu^+\mu^-)K^+$,
- $B_d^0 \to K^+\pi^-$,
- $B_s^0 \to J/\psi(\mu^+\mu^-)\phi(K^+K^-)$.

---

[1] Selection cuts applied on an event at the trigger level to reject high multiplicity events.

Table 5.1: Summary of advantages and disadvantages of the three normalisation channels.

	$B_u^+ \to J/\psi\, K^+$	$B_d^0 \to K^+\pi^-$	$B_s^0 \to J/\psi\, \phi$
event kinematics	$-$	$+$	$-$
trigger	$+$	$-$	$+$
PID	$+$	$-$	$+$
branching ratio	$+$	$+$	$-$
tracking efficiency	$-$	$+$	$-$
f_s/f_d	$-$	$-$	$+$
global event cuts	$+$	$-$	$+$

The advantages and disadvantages of the normalisation channels are discussed below and summarised in Table 5.1. For $B_u^+ \to J/\psi(\mu^+\mu^-)K^+$ and $B_s^0 \to J/\psi(\mu^+\mu^-)\phi(K^+K^-)$ the trigger and the particle identification (PID) are very similar to $B_s^0 \to \mu^+\mu^-$. Their global event cuts are the same as for $B_s^0 \to \mu^+\mu^-$. But for both channels the tracking efficiency dominates the systematic uncertainty in the ratio of efficiencies. The reason are the additional track(s) of the kaon(s) which need to be reconstructed.

An advantage of $B_s^0 \to J/\psi(\mu^+\mu^-)\phi(K^+K^-)$ is the cancellation of the uncertainty in the ratio of the B fragmentation fractions. But the branching ratio is not known to a very good precision. Its relative error is around 25%:

$$BR(B_s^0 \to J/\psi(\mu^+\mu^-)\phi(K^+K^-)) = (3.335^{+0.813}_{-0.871}) \cdot 10^{-5} \quad [40,\ 34]. \qquad (5.5)$$

However, Belle and LHCb plan to re-measure this branching ratio with much better precision. On the contrary the branching ratio is known to a precision better than 4% (Equations 5.6 and 5.7) for the channels $B_u^+ \to J/\psi(\mu^+\mu^-)K^+$ and $B_d^0 \to K^+\pi^-$.

$$BR(B_u^+ \to J/\psi(\mu^+\mu^-)K^+) = (6.007 \pm 0.211) \cdot 10^{-5} \quad [34] \qquad (5.6)$$

$$BR(B_d^0 \to K^+\pi^-) = (1.94 \pm 0.06) \cdot 10^{-5} \quad [34] \qquad (5.7)$$

However a large uncertainty is induced on both of these channels, since the fraction of the B fragmentation ratios is only known up to a relative error of $\approx 7.9\%$:

$$\langle \frac{f_s}{f_d} \rangle = 0.267^{+0.021}_{-0.020} \quad [41]. \qquad (5.8)$$

The channel $B_d^0 \to K^+\pi^-$ differentiates itself through the same kinematics as $B_s^0 \to \mu^+\mu^-$ for reconstruction but different GECs, trigger and PID. The latter two dominate the uncertainty in the ratio of the trigger efficiencies.

The analyses of the three normalisation channels are quite complementary, but the normalisation factors obtained for the three channels are in good agreement as

Table 5.2: Measured normalisation factor $\alpha_{B_s^0\to\mu\mu}$ for all three normalisation channels.

	$\alpha_{B_s^0\to\mu\mu}$ from Ref. [2]
$B_u^+ \to J/\psi\, K^+$	$(8.4 \pm 1.3)\cdot 10^{-9}$
$B_d^0 \to K^+\pi^-$	$(7.3 \pm 1.8)\cdot 10^{-9}$
$B_s^0 \to J/\psi\, \phi$	$(10.5 \pm 2.9)\cdot 10^{-9}$

can be seen in Table 5.2. The weighted average of the three channels, taking into account correlations, leads to the final normalisation factor: $\alpha_{B_s^0\to\mu\mu} = (8.6 \pm 1.1)\cdot 10^{-9}$ [2].

5.4 Geometrical Likelihood

The geometrical likelihood is a combination of variables, which allows a distinct separation of signal- and background-like events. The GL assigns a probability to each event to be signal or background like, based on the geometrical and topological characteristics of each event. As described in Ref. [2] the variables defining the GL are:

- Lifetime of the B candidate.
- Muon impact parameter χ^2. [2]
- B_s^0 impact parameter.
- Distance of closest approach between the two muon candidates.
- Isolation of each muon track.
- Transverse momentum of the B candidate.

The six variables described above are combined using the procedure described in Ref. [42] to produce a uniform distribution (GL) between 0 and 1 for signal candidates (Figure 5.2). The background peaks towards small values of GL. The GL is divided in 4 equidistant bins and the sensitive region for signal events is defined as GL>0.5 (bin 3 and bin 4).

The GL for signal and background is trained on MC and calibrated from data. The calibration of the signal probability is performed with $B_q^0 \to h^+h^-$ candidates (q stands for a u- or a d-quark and h for a pion or a kaon), while the background probability is calibrated using invariant mass sidebands.

---

[2] The muon impact parameter χ^2 is the difference between the PV χ^2 with and without the muon track.

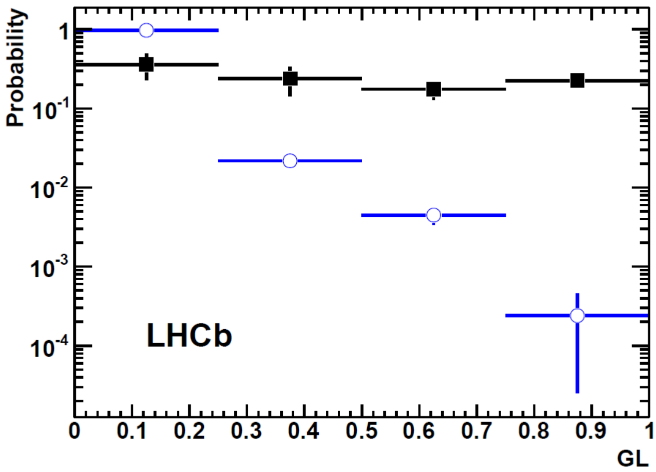

Figure 5.2: The GL probability for signal (black solid squares) and background (blue circles). From Ref. [2].

5.5 Invariant Mass

To determine the branching ratio of $B_s^0 \to \mu^+\mu^-$, the number of observed events d_i in six mass bins i was compared to the number of expected signal plus background events $s_i + b_i$. First the number of expected signal events $N_{\mu\mu}$ in all mass bins was determined by dividing the branching ratio hypothesis (for example the Standard Model branching ratio) by the $\alpha_{B_s^0 \to \mu\mu}$ from section 5.3. $N_{\mu\mu}$ corresponds to the total integral of the Crystal Ball [43] function, which defines the signal shape. Its five parameters[3] were measured as follows: the mean of the signal function by the mass fit of the decay $B_s^0 \to K^+K^-$, the σ by the weighted average of the two methods described later in this section, the tail parameter n was fixed to 1, the α was taken from $B_s^0 \to \mu^+\mu^-$ MC and the amplitude was fixed to normalise the integral to $N_{\mu\mu}$. With the Crystal Ball function determined by these measured parameters, the fraction s_i of $N_{\mu\mu}$ falling into each mass bin i is obtained.

For the background an exponential function was chosen:

$$f(M) = Ae^{-kM} \quad . \tag{5.9}$$

Its parameters were fitted from the sidebands of a mass window of ±600 (±1200) MeV in the lower (upper) two GL bins. The parameter k was fitted individually for each GL bin, to allow for different background composition. The number of expected background events b_i in each mass bin is calculated by integrating the background function over the range of the mass bin.

---

[3] The parameters of the Crystal Ball functions are: the mean m of the Gaussian part, the width σ of the Gaussian part (is equivalent to the mass resolution), the tail parameters n and α and the amplitude A.

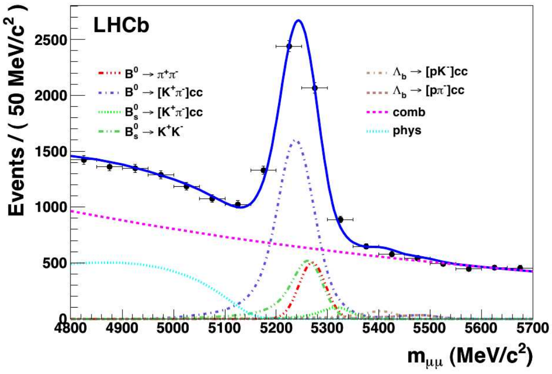

Figure 5.3: Full fit of different two body decays, with two hadrons in the final state. From [2].

To determine the mass resolution of the B_s^0 meson, i.e. the σ of the Crystal Ball function, two methods were combined: a full fit of the invariant mass spectrum taking into account $B_q^0 \to h^+h^-$ and $\Lambda_b \to h^+h^-$ two body decays and a calibration using dimuon charmonium and bottomonium resonances.

The first method uses decays with two hadrons in the final state, which are listed in Figure 5.3. Apart from the mass of the decay products, these decays feature the same event kinematics as $B_s^0 \to \mu^+\mu^-$ and the same event selection was used. The different decays were normalised to their branching ratio taken from Ref. [34] and the muon mass was assigned to the decay products. Information about the PID was not used since it biases the mass resolution. The mass resolution $\sigma_{M\ \text{two body}}$ is determined by fitting simultaneously the several overlapping mass peaks (Figure 5.3) taking into account the measured branching fractions:

$$\sigma_{M\ \text{two body}} = (25.8 \pm 1.0^{\text{stat}} \pm 2.7^{\text{syst}})\text{MeV/c}^2, \quad [2] \tag{5.10}$$

with a systematic error of 10.5%. To select the different decays with kaons and pions in the final state, the use of particle identification information from the RICH subdetectors is inevitable. The PID information is depending on the track momentum and selection cuts on the PID bias the mass resolution for two body decays. This bias was corrected for, but still introduces a notable systematic error. More details about this method can be found in reference [2].

The second method uses the dimuon resonances J/ψ(1S), J/ψ(2S), Υ(1S), Υ(2S) and Υ(3S). The mass spectra are fitted with a double Crystal Ball function on exponential background, where the tail parameters of the Crystal Ball function were fixed from MC. An event weighting procedure was applied on the momenta of the parent particles to match the parent momentum spectra to the $B_s^0 \to \mu^+\mu^-$ momentum spectra. The mass resolution as a function of invariant mass of the resonances was fitted with a first order polynomial. Knowing the mass of the B_s^0

meson, its mass resolution $\sigma_{M\ \text{polyn fit}}$ was defined from the fit:

$$\sigma_{M\ \text{polyn fit}} = (27.8 \pm 0.3^{\text{stat}} \pm 1.1^{\text{syst}})\,\text{MeV/c}^2 \quad [44]. \tag{5.11}$$

Here the systematic error comes to 4.0%. This method is dominated by the J/ψ(1S) and Υ(1S) resonances due to statistical reasons. The fit model for the mass spectra and the weighting procedure introduce non-negligible systematic uncertainty. The approximation of the relation between the mass resolution and the mass with a first order polynomial, does not well describe the resonances with higher masses and introduces a notable systematic error. The detailed description of this method can be found in [44].

5.6 Determination of the Limit on the Branching Ratio

To set a limit on the $B_s^0 \to \mu^+\mu^-$ branching ratio the 'modified frequentist' method CL_s [37] is used. A detailed description of this method is given in Ref. [45]. The CL_s method is based upon a hypothesis test. The null-hypothesis claims the absence of signal: only background is present. The other hypothesis is the presence of signal (observation of signal and background). CL_s is the ratio of the confidences in the 'signal plus background' hypothesis to the background-only hypothesis:

$$CL_\text{s} = \frac{CL_\text{s+b}}{CL_\text{b}} \quad . \tag{5.12}$$

The number of expected signal- and background events (s_i and b_i) in each mass bin was determined as described in section 5.5. Multiplied by the probabilities in each GL bin (section 5.4) a number of expected signal and background events is found for each of the 24 two-dimensional bins (s_j and b_j).

To identify the shape of the 'signal plus background' and background-only hypotheses, a two-dimensional toy MC experiment was performed. With the input of the probability of $s_j + b_j$ for each bin, the toy MC leads to a number of simulated 'observed' events d'_j in each bin. Out of d'_j, s_j and b_j a Q value is calculated for the 'signal plus background' hypothesis:

$$Q = \prod_{j=1}^{n} Q_j \quad [45], \tag{5.13}$$

$$Q_j = \frac{f(d'_j, s_j + b_j)}{f(d'_j, b_j)} \quad [45]. \tag{5.14}$$

The function $f(k, \lambda)$ is the Poisson distribution of k observed events and λ expected events. The toy MC experiment is repeated several times to obtain the probability distribution of Q-values (Figure 5.4).

The Q distribution for the background-only hypothesis is also obtained by toy MC experiments, but with the input of the GL background probability for each bin.

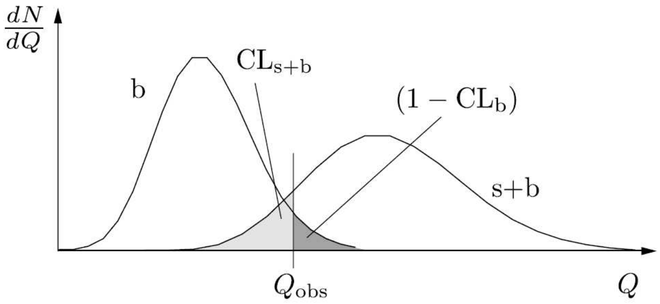

Figure 5.4: Probability distributions of Q values for the background-only hypothesis (b) and the 'signal plus background' hypothesis (s+b). The schematic shows the quantities $CL_{\text{s+b}}$ and CL_{b}. From Ref. [45].

A third toy MC experiment generates several Q distributions compatible with the background only hypothesis.

From the real number of observed events d_j in each two-dimensional bin, the Q-value Q_{obs} is calculated. The quantities $CL_{\text{s+b}}$ and CL_{b} are defined in Equations 5.15 and 5.16 and illustrated in Figure 5.4.

$$CL_{\text{s+b}} \equiv Prob(Q \leq Q_{\text{obs}})_{\text{s+b}} \quad [45] \tag{5.15}$$

$$CL_{\text{b}} \equiv Prob(Q \leq Q_{\text{obs}})_{\text{b}} \quad [45] \tag{5.16}$$

From integration of the regions in the Q-distributions the quantity CL_{s} is calculated. Alternatively CL_{s} is calculated using the expected distribution (Q_j with d_j').

Finally CL_{s} is calculated for different branching ratio hypotheses. Figure 5.5 shows the CL_{s} calculated from the observed number of events, for different branching ratio hypotheses, as the black solid curve. The black dashed curve shows the CL_{s} as a function of the branching ratio for the expected number of events. The green band indicates the $\pm 1\sigma$ interval of possible CL_{s} for the third toy MC experiment, which generates distributions compatible with the background-only hypothesis.

The upper limit on the branching ratio of $B_s^0 \to \mu^+\mu^-$ was set, where the observed distribution is not compatible with the signal hypothesis ($CL_{\text{s}} < 10\%$) at 90% confidence level (C.L.):

$$\text{BR}(B_s^0 \to \mu^+\mu^-) < 4.3(5.6) \cdot 10^{-8} \quad \text{at } 90\% \ (95\%) \text{ C.L. [2]} \tag{5.17}$$

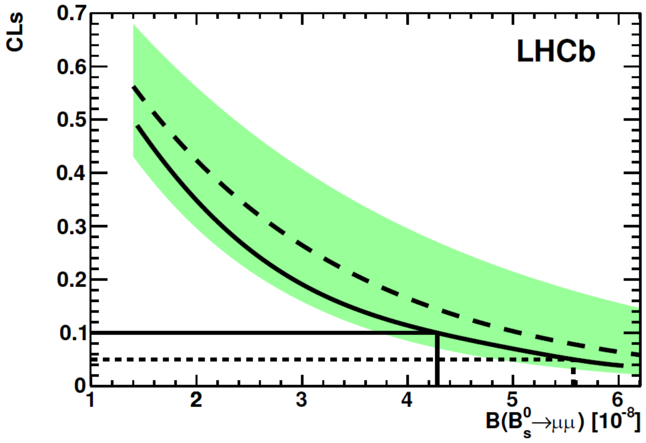

Figure 5.5: CL_s values for different branching ratio hypotheses as a function of the $B^0_s \to \mu^+\mu^-$branching ratio. The solid (dashed) curve are the CL_s values with the observed (expected) distribution. The green band is the $\pm1\sigma$ interval for CL_s from hypotheses compatible with background-only. The upper limits for the $B^0_s \to \mu^+\mu^-$branching ratio at 90% (95%) C.L. are determined by the solid (dashed) line. From Ref. [2].

Chapter 6

Mass Resolution Studies

A new method is established to estimate the $B_s^0 \to \mu^+\mu^-$ invariant mass resolution on a event-by-event basis using data and with reduced systematic uncertainty compared to the methods presented in section 5.5. In addition the method calibrates the event-by-event momentum error using data. It uses error propagation of the reconstructed momenta and opening angle of the decay products. The method was developed and tested using MC, the first real collision data from 450 on 450 GeV protons ($\sqrt{s} = 0.9$ TeV) and data from 3500 on 3500 GeV collisions ($\sqrt{s} = 7$ TeV). The decays $K_s^0 \to \pi^+\pi^-$ and $J/\psi \to \mu^+\mu^-$ were studied and $J/\psi \to \mu^+\mu^-$ was used to evaluate the method, which was applied to several other two-body decays.

The data sets used are presented in section 6.1. The basis for the method is the formula for the two-body invariant mass calculation given in section 6.2 and the needed parametrisation described in section 6.3. The influence of the key observables and its correlation were studied in section 6.4. These results were used to obtain an estimate of the uncertainty on the magnetic field calibration (section 6.4.1). In section 6.5 the main part of the mass resolution studies is presented: the calculation of the uncertainty on the mass per event. The calculation of a correction factor, acting on the track momentum error, is described in section 6.6. To remove bias on the correction factor, coming from the underlying background in the mass spectrum, a particular sideband subtraction method is described in section 6.7. Several cross-checks were performed in the systematic analysis to evaluate the method as presented in section 6.8. They allowed to estimate the systematic error on the mass resolution (section 6.8.7). In section 6.9 the results are presented and discussed.

6.1 Data Sets

The data sets were collected in two different periods: 2009 and 2010. In 2009 the centre-of-mass energy for the LHC proton collisions was $\sqrt{s} = 0.9$ TeV and was enhanced to $\sqrt{s} = 7$ TeV in 2010. Table 6.1 gives an overview of the different data sets used. The studies concerning the momentum scale factor α (see section 6.4.1)

Table 6.1: Data sets used. $\mathcal{L}$ refers to the integrated luminosity, M to the magnet polarities 'up' or 'down', $\mathcal{R}$ to the track reconstruction version and $\mathcal{S}$ to stripping version. The term $B_q^0 \to h^+h^-$includes the decays $B_s^0 \to K^+K^-$, $B_d^0 \to K^{+,-}\pi^{-,+}$ and $B_d^0 \to \pi^+\pi^-$.

decay	$\sqrt{s}$ /TeV	data/MC	M	$\mathcal{R}$	$\mathcal{S}$	$\mathcal{L}$ /pb^{-1}	used for
$K_s^0 \to \pi^+\pi^-$	0.9	data 2009	down	07	-	-	Tab. 6.5
$K_s^0 \to \pi^+\pi^-$	7	MC 2010	down	07	-	-	sec. 6.4
$K_s^0 \to \pi^+\pi^-$	7	data 2010	down	07	-	-	sec. 6.4
$B_s^0 \to \mu^+\mu^-$	7	MC 2010	down	01	-	-	sec. 6.4
$J/\psi \to \mu^+\mu^-$	7	MC 2010	up	03	-	-	sec. 6.4, 6.5 ff.
$J/\psi \to \mu^+\mu^-$	7	data 2010	down	03	-	-	sec. 6.4
$J/\psi \to \mu^+\mu^-$	7	data 2010	up	03	-	-	sec. 6.4
$J/\psi \to \mu^+\mu^-$	7	data 2010	up	08	12b	18.0 ± 2.0	sec. 6.4, 6.5 ff.
$J/\psi \to \mu^+\mu^-$	7	data 2010	down	08	12b	7.5 ± 0.7	sec. 6.5 ff.
$\Upsilon \to \mu^+\mu^-$	7	data 2010	up	08	12b	18.0 ± 2.0	Tab. 6.14
$\Upsilon \to \mu^+\mu^-$	7	data 2010	down	08	12b	7.5 ± 0.7	Tab. 6.14
$B_q^0 \to h^+h^-$	7	data 2010	up	08	12b	18.0 ± 2.0	Tab. 6.14
$B_q^0 \to h^+h^-$	7	data 2010	down	08	12b	7.5 ± 0.7	Tab. 6.14

are the only results from data collected in 2009 with the decay $K_s^0 \to \pi^+\pi^-$ and the only ones using downstream tracks and long tracks. All the other studies used only long tracks. The studies concerning the influence of the daughter momenta and the opening angle on the mass resolution (section 6.4) were prepared with MC data sets and compared to the available data until about April 2010. Later in 2010 not all events were made available for analysis anymore. An event selection step called 'stripping' channelised the reconstructed data stream into different stripping lines, where each line has its own selection cuts and scaling. The data with track reconstruction version 08 and stripping version 12b was used for all the studies concerning the determination of the event-by-event error on the mass and the correction factor $F(p)$. The integrated luminosity of 18.0 pb^{-1} corresponds to the total amount of data taken in 2010 with magnet 'up' polarity. Some data collected with magnet 'down' polarity were not used, since the temperature of the Tracker Turicensis was lowered about 20° C. The effect of the thermal contraction would have requested a new detector alignment. A new alignment was not available at this time and the data from the lower temperature was excluded. This is the reason for the unequal amount of luminosity in magnet 'up' and 'down' polarity data. The selection cuts for the different decays can be found in appendix B.

6.2 Invariant Mass

For a two-body decay, the invariant mass m_M of the mother particle can be calculated from the four-momenta $\mathcal{P}_i^2$ of the daughter particles as described in Equations 6.1 – 6.3. Subscript M refers to the mother particle, subscript 1 to the first daughter particle, subscript 2 to the second daughter particle. m_i are the masses and Θ is the angle between the daughter 3-momenta $\overrightarrow{p_i}$:

$$\begin{aligned} \mathcal{P}_M^2 &= (\mathcal{P}_1 + \mathcal{P}_2)^2 & (6.1) \\ m_M^2 &= m_1^2 + m_2^2 + 2(\sqrt{\overrightarrow{p}_1^2 + m_1^2}\sqrt{\overrightarrow{p}_2^2 + m_2^2} - |\overrightarrow{p}_1||\overrightarrow{p}_2|\cos\Theta) & (6.2) \end{aligned}$$

With the assumption $m_{1,2}^2 << p_{1,2}^2$ the terms $m_{1,2}^2$ can be neglected [1] in $\sqrt{\overrightarrow{p}_{1,2}^2 + m_{1,2}^2}$, which simplifies Equation (6.2) to:

$$m_M^2 = m_1^2 + m_2^2 + 2|\overrightarrow{p}_1||\overrightarrow{p}_2|(1 - \cos\Theta) \qquad (6.3)$$

Assuming the masses $m_{1,2}$ of the daughter particles to be known [34] (errors are negligible), the uncertainty on the mother mass m_M is dominated by the measurement error on the momenta of the daughter particles $\overrightarrow{p}_{1,2}$ and the measurement error on the angle Θ. The method presented here uses Equation (6.3) by propagating the measurement error on $\overrightarrow{p_i}$ to estimate the uncertainty on m_M.

6.3 Parametrisation of Track Parameters

The event reconstruction in LHCb starts with the clusters provided by the readout board TELL1 (chapter 3). A pattern recognition algorithm returns tracks out of the clusters. The tracks are described by several linear track segments, which are tangent to the particle's trajectory [46]. These segments are called track states. A track state $\vec{x}$ is parametrised by five parameters as a function of the z-coordinate[2]:

$$\vec{x} = \begin{pmatrix} x \\ y \\ t_x \\ t_y \\ q/p \end{pmatrix} \text{ with } t_x = \frac{\partial x}{\partial z}\text{, and } t_y = \frac{\partial y}{\partial z} \quad [46]. \qquad (6.4)$$

x and y are the positions at the given z-coordinate, $q = \pm 1$ is the charge of the particle and p its absolute momentum. These track states are the input for the track fit using a Kalman filter procedure. The Kalman filter procedure propagates the

---

[1] A Taylor expansion of the square root term in $p_{1,2} \cdot \sqrt{1 + \frac{m_{1,2}^2}{p_{1,2}^2}}$ was calculated. However, the effect on the final result was well within the errors, therefore the approach was dropped.

[2] For a definition of the coordinate system in LHCb see section 2.2

track states in z-direction through the detector and takes into account the momentum dependent multiple scattering on the detector material. After the track fit a 5×5 covariance matrix is calculated to each track state vector $\vec{x}$. A vertex fit is performed by a sequential combination of a set of tracks, requiring a common origin in space. For all studies described in this thesis, the track state was propagated to the z-value of the origin vertex.

The relevant parameters for the momentum measurement and therefore for the invariant mass measurement are t_x, t_y and q/p. A different parametrisation of the track state was used to estimate the uncertainty on the invariant mass by error propagation on Equation (6.3):

$$\vec{x} = \begin{pmatrix} x \\ y \\ p_1 \\ p_2 \\ \cos\Theta \end{pmatrix} \tag{6.5}$$

The details of the parametrisation are given in appendix A.1. A parametrisation with p_x, p_y and p_z for the last three entries of the track state vector is provided by the analysis software. As a cross-check p_x, p_y and p_z were re-parametrised to p_1, p_2 and $\cos\Theta$ (appendix A.2). The resulting two covariance matrices for p_1, p_2 and $\cos\Theta$ were found to be equal.

6.4 Track State Parameters and Invariant Mass Resolution

The correlation between p_1, p_2 and $\cos\Theta$ and their influence on the mass resolution σ_M of the mother particle were investigated in a MC study of three decays: $B_s^0 \rightarrow \mu^+\mu^-$, $J/\psi \rightarrow \mu^+\mu^-$ and $K_s^0 \rightarrow \pi^+\pi^-$. The results of the MC study were compared to data (see section 6.1). The selection cuts for the three decays can be found in appendix B.

The idea for the MC study is to replace the reconstructed $p_{1,2}$ and $\cos\Theta$ in the invariant mass formula (Equation 6.3) by their generated values and to recalculate the invariant mass m_M. The recalculated invariant mass was compared to the invariant mass after reconstruction and vertex fit, provided by the analysis software as a cross check. The invariant mass distributions of six different alternatives to calculate m_M were compared:

1. m_M after reconstruction and vertex fit.
2. m_M calculated using the reconstructed values of $p_{1,2}$ and $\cos\Theta$.
3. m_M calculated using the generated p_1 (true p_1) and the reconstructed p_2 and $\cos\Theta$.

Table 6.2: Results of MC studies on long tracks at $\sqrt{s} = 7$ TeV. The comparison of σ_M from the reconstructed m_M after the vertex fit and σ_M of the reconstructed and recalculated m_M show good agreement for $B_s^0 \to \mu^+\mu^-$ and $J/\psi \to \mu^+\mu^-$. The influence of reconstruction of the muon momenta and $\cos\Theta$ on the mass resolution σ_M is determined and the parameters of the pull distribution fitted with a Gaussian on a linear background are shown.

		$B_s^0 \to \mu^+\mu^-$	$J/\psi \to \mu^+\mu^-$	$K_s^0 \to \pi^+\pi^-$
1.	σ_M reconstr. after vertex fit /MeV/c^2	16.90 ± 0.09	13.14 ± 0.05	3.01 ± 0.07
2.	σ_M reconstr. /MeV/c^2	16.94 ± 0.09	13.12 ± 0.05	3.42 ± 0.07
3.	σ_M with true p_1 /MeV/c^2	12.43 ± 0.06	9.96 ± 0.06	3.01 ± 0.09
4.	σ_M with true p_2 /MeV/c^2	12.27 ± 0.06	10.01 ± 0.06	3.01 ± 0.09
5.	σ_M with true p_1 and p_2 /MeV/c^2	5.41 ± 0.03	5.01 ± 0.03	2.73 ± 0.08
6.	σ_M with true cosΘ /MeV/c^2	15.76 ± 0.08	12.13 ± 0.05	0.92 ± 0.02
	pull distribution (after vertex fit)			
	mean of pull distribution	0.081 ± 0.005	0.065 ± 0.002	0.071 ± 0.007
	σ of pull distribution	1.141 ± 0.004	1.242 ± 0.002	1.16 ± 0.01

4. m_M calculated using the generated p_2 (true p_2) and the reconstructed p_1 and $\cos\Theta$.

5. m_M calculated using the generated $p_{1,2}$ and the reconstructed $\cos\Theta$.

6. m_M calculated using the generated $\cos\Theta$ (true $\cos\Theta$) and the reconstructed $p_{1,2}$.

The obtained invariant mass distributions were fitted with a Crystal Ball function (see plots in appendix C). The mass resolution σ_M is taken as the standard deviation of the Gaussian part of the fitted Crystal Ball function. Table 6.2 shows the σ_M from the six alternatives and three different decays studied. All the alternatives but the first are independent of the vertex fit information. As can be seen in Table 6.2, the mass resolution obtained by the first alternative is in the same range as the one from the second alternative, which was calculated as a cross check.

Table 6.2 also shows the influence of the reconstruction of the two muon momenta and their opening angle Θ on the mass resolution σ_M. The impact of the daughter momenta on σ_M is more pronounced for the decays $B_s^0 \to \mu^+\mu^-$ and $J/\psi \to \mu^+\mu^-$, than for $K_s^0 \to \pi^+\pi^-$. On the other hand the impact of the opening angle on σ_M is small for $B_s^0 \to \mu^+\mu^-$ and $J/\psi \to \mu^+\mu^-$ but gets relevant for the decay $K_s^0 \to \pi^+\pi^-$.

In view of a method to estimate the mass resolution for the $B_s^0 \to \mu^+\mu^-$ decay, a decay with a similar parameter space in terms of momentum and opening angle

Table 6.3: Results of studies on long tracks with $\sqrt{s} = 7$ TeV collision data. Again the recalculated mass resolution is compared to the reconstructed one from after the vertex fit. The parameters of the pull distribution fitted with a Gaussian show a small mass bias and an underestimation of the errors.

		$J/\psi \to \mu^+\mu^-$ down	$K_s^0 \to \pi^+\pi^-$ down
1.	σ_M reconstr. after vertex fit /MeV/c^2	14.94 ± 0.88	3.4 ± 0.11
2.	σ_M reconstr. /MeV/c^2	15.20 ± 0.92	3.6 ± 0.16
	pull distribution (after vertex fit)		
	mean of pull distribution	-0.93 ± 0.08	-0.07 ± 0.02
	σ of pull distribution	1.67 ± 0.08	1.42 ± 0.02

of the daughter particles is required to evaluate the method. Figures 6.1 and 6.2 show, that the momentum and opening angle distributions of $J/\psi \to \mu^+\mu^-$ do overlap to a large fraction with the corresponding $B_s^0 \to \mu^+\mu^-$ distributions for data and MC. The $K_s^0 \to \pi^+\pi^-$ event topology is not close enough to the one from $B_s^0 \to \mu^+\mu^-$ and therefore the decay $K_s^0 \to \pi^+\pi^-$ was not used for evaluating the method to calculate the uncertainty on the mass per event. This is also reflected by the results in Table 6.2.

The pull distribution of the invariant mass m_M was studied, to check for a possible bias of the reconstructed invariant mass and to cross check the reliability of the covariance matrix for the reconstructed parameters $p_{1,2}$ and $\cos\Theta$. The invariant mass distribution and its pull distribution are shown in appendix C. The goodness of the error estimate on the momentum was of particular interest, since the uncertainty on the mass is dominated by it. If the errors are correctly estimated, the pull distribution has a Gaussian shape with a mean of 0 and a σ of 1.0. The mean of the pull distribution in Table 6.2 (MC) shows a bias, most pronounced for the decay $B_s^0 \to \mu^+\mu^-$. As a side-result a scale factor for the momentum could be determined (section 6.4.1) from the mean of the pull distributions. Also the σ of the pull distribution shows a tendency towards bigger values than 1.0 and reveals, that the errors on the momenta are underestimated by the track fit. This behaviour could also be introduced by an incorrect description of the multiple scattering in the simulation. For data (Table 6.3) the effect is even more pronounced. This is attributed to not yet perfect detector alignment, magnetic field calibration and material description and is discussed in section 6.6.2. In section 6.6 this problem of underestimating the errors of p_1 and p_2 is addressed.

The correlation between the two muon momenta and $1 - \cos\Theta$ was studied and is found to be $< 5\%$. Figure 6.3 shows the distributions of the relative errors of p_1, p_2 and $1 - \cos\Theta$ and the correlation coefficients ρ between the three parameters. Table 6.4 shows the structure of Figure 6.3.

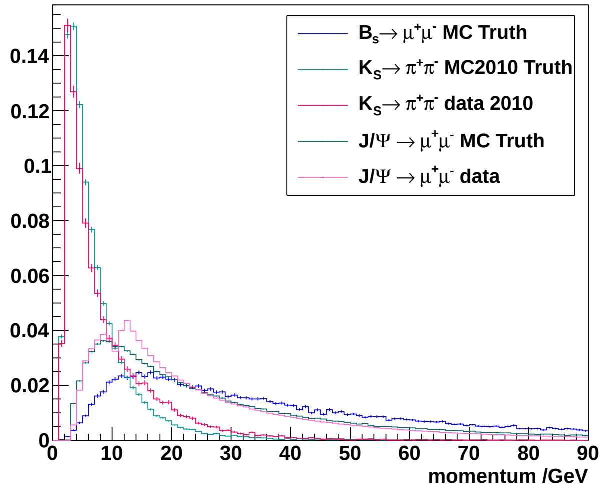

Figure 6.1: Momentum distribution of the negative daughter particle for $K_s^0 \rightarrow \pi^+\pi^-$ and $J/\psi \rightarrow \mu^+\mu^-$ data and MC and $B_s^0 \rightarrow \mu^+\mu^-$ MC at $\sqrt{s} = 7$ TeV. The overlap of $J/\psi \rightarrow \mu^+\mu^-$ with $B_s^0 \rightarrow \mu^+\mu^-$ is good, whilst the $K_s^0 \rightarrow \pi^+\pi^-$ are at lower momenta.

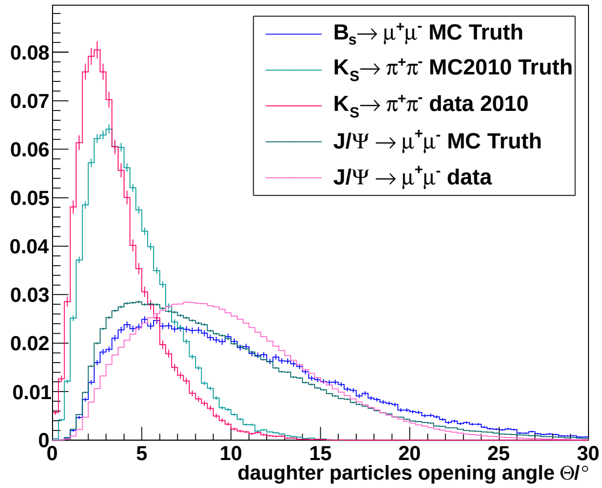

Figure 6.2: Distribution of the opening angle Θ for $K_s^0 \rightarrow \pi^+\pi^-$ and $J/\psi \rightarrow \mu^+\mu^-$ data and MC and $B_s^0 \rightarrow \mu^+\mu^-$ MC at $\sqrt{s} = 7$ TeV. The overlap for $J/\psi \rightarrow \mu^+\mu^-$ with $B_s^0 \rightarrow \mu^+\mu^-$ is good while $K_s^0 \rightarrow \pi^+\pi^-$ peaks at smaller opening angles.

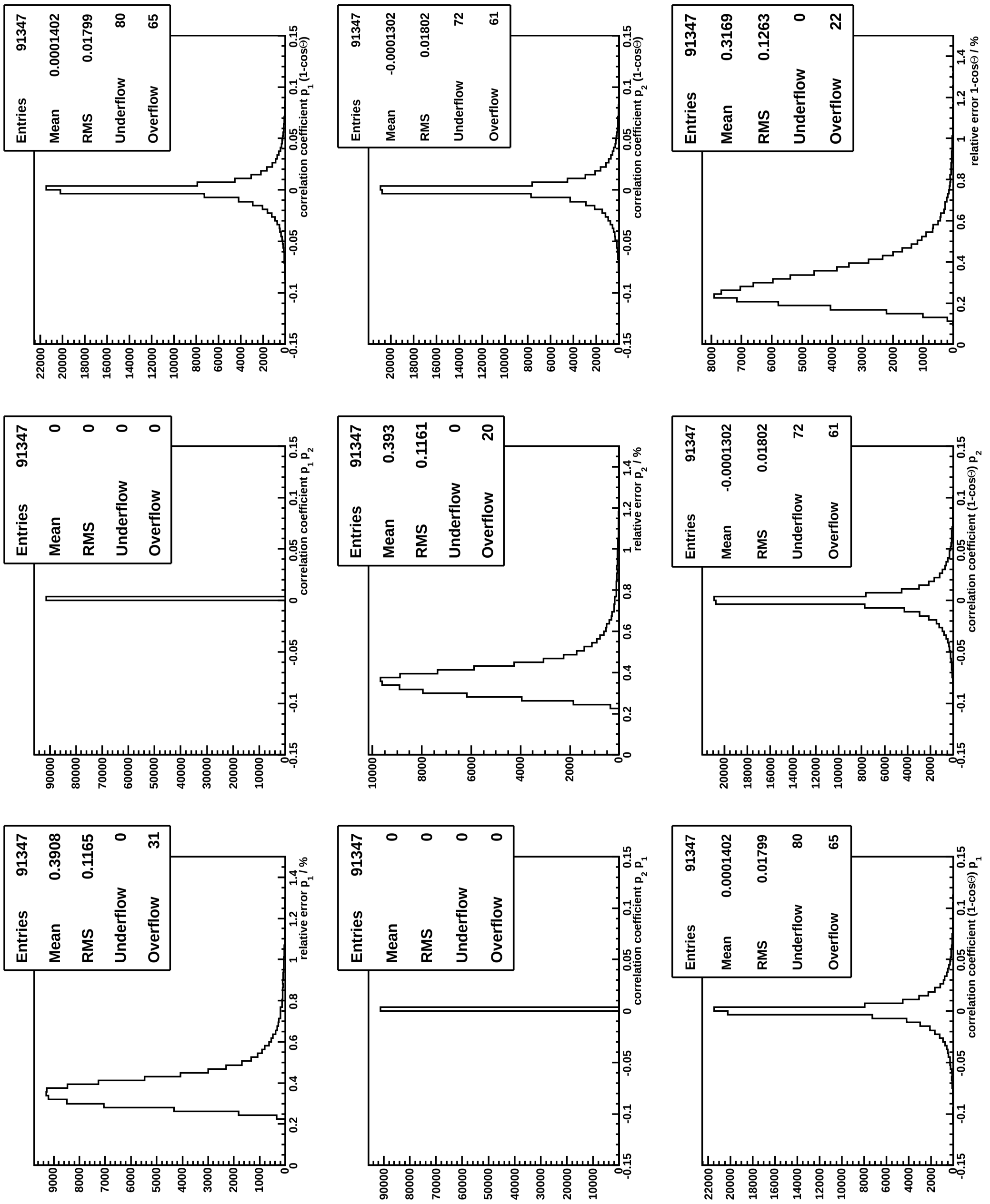

Figure 6.3: Correlation and relative errors for the muon momenta and $1 - \cos\Theta$ determined on $J/\psi \to \mu^+\mu^-$ MC. The correlation between momenta and opening angle is found to be below 5%.

Table 6.4: Structure of Figure 6.3. ρ are the correlation coefficients between the three parameters p_1, p_2 and $1 - \cos\Theta$.

	p_1	p_2	$1 - \cos\Theta$
p_1	rel. error p_1/%	ρ	ρ
p_2	ρ	rel. error p_2/%	ρ
$1 - \cos\Theta$	ρ	ρ	rel. error $1 - \cos\Theta$/%

Table 6.5: K_s^0 masses of $\sqrt{s} = 0.9$ TeV collision data. A bias is determined compared to the measured value $m_{Ks} = 497.614 \pm 0.024$ MeV from Ref. [34]. The momentum scale factor α was calculated and compared to the α found in Ref. [47].

	long tracks	downstream tracks
K$_s$ mass reconstr. after vertex fit /MeV/c^2	497.37 ± 0.13	497.3 ± 0.2
K$_s$ mass reconstr. /MeV/c^2	497.56 ± 0.15	497.5 ± 0.3
α from Ref. [47]	-0.14 ± 0.04 %	
α for reconstr. mass after vertex fit	-0.08 ± 0.04 %	-0.1 ± 0.07 %
α for reconstr. mass	-0.02 ± 0.05 %	-0.03 ± 0.1 %

6.4.1 Mass Bias and Momentum Scale Factor α

The mean of the invariant mass distribution is shifted for data, when the magnetic field is not calibrated correctly. This effect was studied in detail in Ref. [48] and [47]. The momentum scale factor α was calculated as in Equation (6.6) and compared to the results from Ref. [47].

$$\Delta m = -304 \cdot \alpha \quad [48] \tag{6.6}$$

Δm is the mass difference in MeV/c^2 between the measured mass and the measured mass from the Particle Data Group [34] (PDG mass). The results for the decay $K_s^0 \to \pi^+\pi^-$ are in Table 6.5 and the study was done for long tracks and downstream tracks (section 2.3) of the very first LHCb data taken at $\sqrt{s} = 0.9$ TeV. The α from the reconstructed mass after the vertex fit for long tracks is in agreement with Ref. [47] as shown in Table 6.5. The α from the reconstructed mass is much lower than the one found by Ref. [47], since the mass is closer to the PDG mass [34]. The α was recalculated for the 2010 data and MC in Ref. [49]. The values are presented in Table 6.6 and they are applied on the track momenta as a global correction factor: $p_{\text{corrected}} = (1 - \alpha) \cdot p$. For all further studies in this thesis this momentum scale factor is applied. This reduces the mass bias to below

Table 6.6: Momentum scale factors for $\sqrt{s} = 7$ TeV 2010 collision data [49].

α for MC	$+0.03$ %
α for data	-0.048 %

0.03% for the $J/\psi \to \mu^+\mu^-$decays from 2010 data.

6.5 Uncertainty on the Invariant Mass Calculated per Event

Instead of obtaining the mass resolution from the fit of the invariant mass distribution, the uncertainty per event on the mass can be estimated from the mass distribution itself. The uncertainty on the invariant mass is depending on the following three variables: p_1, p_2 and $\cos\Theta$ as described in section 6.2. Based on Equation (6.3) the uncertainty on the invariant mass of the mother particle is deduced by simple error propagation:

$$m' \equiv m_M^2 - m_1^2 - m_2^2 = 2|\overrightarrow{p}_1||\overrightarrow{p}_2|(1 - \cos\Theta) \quad . \tag{6.7}$$

Uncorrelated variables are assumed, taking into account the results in section 6.4. Be $\sigma_{m'}$ the absolute error on m' and analogue for m_M, p_1, p_2 and $cos\Theta$, and be $p_1 \equiv |\overrightarrow{p_1}|$ and $p_2 \equiv |\overrightarrow{p_2}|$. The relative error $\sigma_{m'}/m'$ is then given by:

$$(\frac{\sigma_{m'}}{m'})^2 = (\frac{\sigma_{p_1}}{p_1})^2 + (\frac{\sigma_{p_2}}{p_2})^2 + (\frac{\sigma_{cos\Theta}}{1 - cos\Theta})^2 \tag{6.8}$$

The daughter masses m_1 and m_2 are assumed to be known [34] and their errors are neglected. From Equation (6.7) then follows:

$$\sigma_{m'} = \frac{\partial(m_M^2 - m_1^2 - m_2^2)}{\partial m_M}\sigma_M \tag{6.9}$$

$$= 2m_M\sigma_M \tag{6.10}$$

where σ_M is the error on the reconstructed invariant mass of the mother particle. Using Equations (6.7), (6.10) in Equation (6.8) the absolute error on the mass σ_M is:

$$\sigma_M = \sqrt{(\frac{\sigma_{p_1}}{p_1})^2 + (\frac{\sigma_{p_2}}{p_2})^2 + (\frac{\sigma_{cos\Theta}}{1 - cos\Theta})^2} \cdot \frac{m_M^2 - m_1^2 - m_2^2}{2m_M} \quad . \tag{6.11}$$

The distribution of σ_M for the per event calculated mass error is shown in Figure 6.4. The average per event error is 9.299 ± 0.001 MeV/c^2. Figure 6.5 shows the distribution of the reconstructed invariant mass for the same data set fitted with a Crystal Ball function on an exponential background. There the fitted mass resolution σ amounts to 13.60 ± 0.01 MeV/c^2.

Figures 6.4 and 6.5 show a strong disagreement between the mean of the σ_M distribution and the mass resolution σ of the fitted mass. The average per event error σ_M is much lower than the fitted mass resolution. Figure 6.6 shows the pull distribution of the reconstructed invariant mass for the same data set. It was fitted with a Gaussian on a linear background. The pull distribution shows a Gaussian $\sigma > 1.0$. This means the errors on the invariant mass are underestimated. The error on the invariant mass is dominated by the errors of the daughter momenta as found in section 6.4. This implies the underestimation of the daughter particles momentum error by the track fit. This behaviour was already found in section 6.4 (Tables 6.2 and 6.3) on the fitted invariant mass distributions.

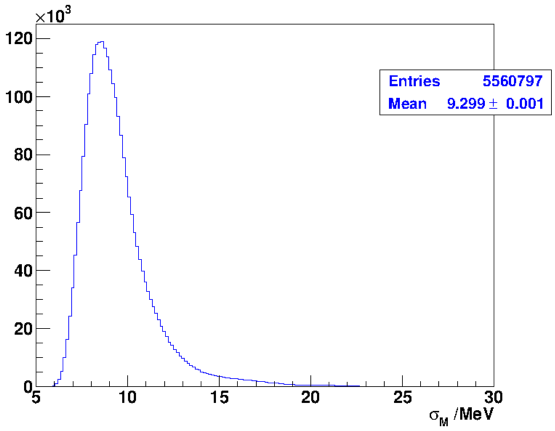

Figure 6.4: Distribution of per event calculated mass error σ_M for the decay $J/\psi \rightarrow \mu^+\mu^-$ magnet 'up' polarity and reconstruction 08.

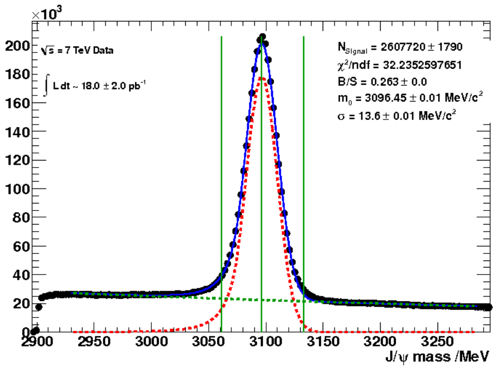

Figure 6.5: Mass distribution of $J/\psi \rightarrow \mu^+\mu^-$ magnet 'up' data from reconstruction 08. The invariant mass distribution is fitted with a Crystal Ball function on an exponential background (blue). The Crystal Ball function without the exponential background is dashed in red and the exponential background is dashed in green. The signal window for the B/S determination is indicated in solid green.

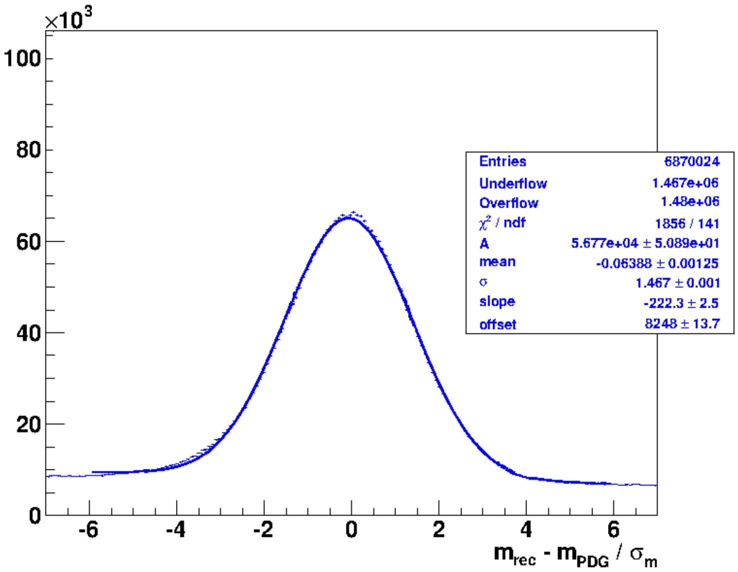

Figure 6.6: Mass pull distribution of the $J/\psi \to \mu^+\mu^-$ magnet 'up' data from reconstructiton 08. The distribution is fitted with a Gaussian on a linear background. m_{rec} is the reconstructed and mother mass, m_{PDG} acts as the 'true' value of the mother mass and is taken from Ref. [34]. The fitted Gaussian parameter σ of the pull is ≈ 1 if the errors are estimated correctly. Clearly the error is underestimated with a σ of 1.437 ± 0.001.

6.6 Correction Factors for the error on the momentum

As shown in section 6.5 the errors on the momenta, received by the track fit are underestimated. To correct for this effect a momentum dependent correction factor $F(p)$ is introduced, acting on the relative error of p_1 and p_2.

$F(p)$ is determined on a decay which gives a good mass peak in data ($J/\psi \to \mu^+\mu^-$) and is applied on several other two-body decays (see section 6.9.1, Table 6.14) as a cross check. $F(p)$ was determined from the pull of the invariant mass distribution such that applying $F(p)$ on the relative error of the two daughter momenta gives an unbiased estimate of the event-by-event uncertainty on the reconstructed mass.

Equation (6.12) shows how the correction is implemented in the formula for the absolute uncertainty on the mass (Equation (6.11)) modified by the correction factor $F(p)$.

$$\sigma_M = \sqrt{\left(F(p_1)\frac{\sigma_{p_1}}{p_1}\right)^2 + \left(F(p_2)\frac{\sigma_{p_2}}{p_2}\right)^2 + \left(\frac{\sigma_{cos\Theta}}{1-cos\Theta}\right)^2} \cdot \frac{m_M^2 - m_1^2 - m_2^2}{2m_M} \tag{6.12}$$

There is no correction factor for $\sigma_{\cos\Theta}$ since its contribution to σ_M is small (see section 6.4).

To estimate $F_i(p_{\text{bin}})$ from data, events were binned in p: $[0.7, 10, 15, 22, 30, 42, 60, 100, 150]$ GeV/c [3] for the realisation of the condition $p_1 \approx p_2$. The binning was a optimised to as many bins as possible and having enough statistics in each bin, to achieve a converging fit of the mass distribution. Equation 6.12 can be resolved for $F_i^2(p_{\text{bin}})$ for each event i, if p_1 and p_2 are in the same bin:

$$F_i^2(p_{\text{bin}}) = \frac{\frac{(m_{\text{rec}}-m_{\text{mean}})^2 \cdot 4m_M^2}{(m_M^2-m_1^2-m_2^2)^2} - \left(\frac{\sigma_{cos\Theta}}{1-cos\Theta}\right)^2}{\left(\frac{\sigma_{p_1}}{p_1}\right)^2 + \left(\frac{\sigma_{p_2}}{p_2}\right)^2} \tag{6.13}$$

For σ_M the difference $m_{\text{rec}} - m_M$ between the reconstructed invariant mass of the mother particle and its nominal mass from Ref. [34] was chosen. Figure 6.7 shows the mass distributions in each bin and the fit by a Crystal Ball function on an exponential background. Although in section 6.4.1 the overall mass bias was found to be small and was corrected by applying α, the picture changes for data binned in momentum. A small mass bias is still left after applying α.

This effect is discussed in the results section 6.6.2. To be independent of this mass bias, the difference $m_{\text{rec}} - m_M$ in each momentum bin was chosen to be $\sigma_M = m_{\text{rec}} - m_{\text{mean}}$ instead and magnetic field correction factors were applied (section 6.4.1, Table 6.6). With this replacement of σ_M, $F_i(p_{\text{bin}})$ can be extracted for similar p_1, p_2 from MC and from data for each event. The correction factor $F(p)$ for each momentum bin i is defined as the mean of the $F_i(p_{bin})$ distribution.

---

[3] For MC the last bin was removed due to a lack of statistics.

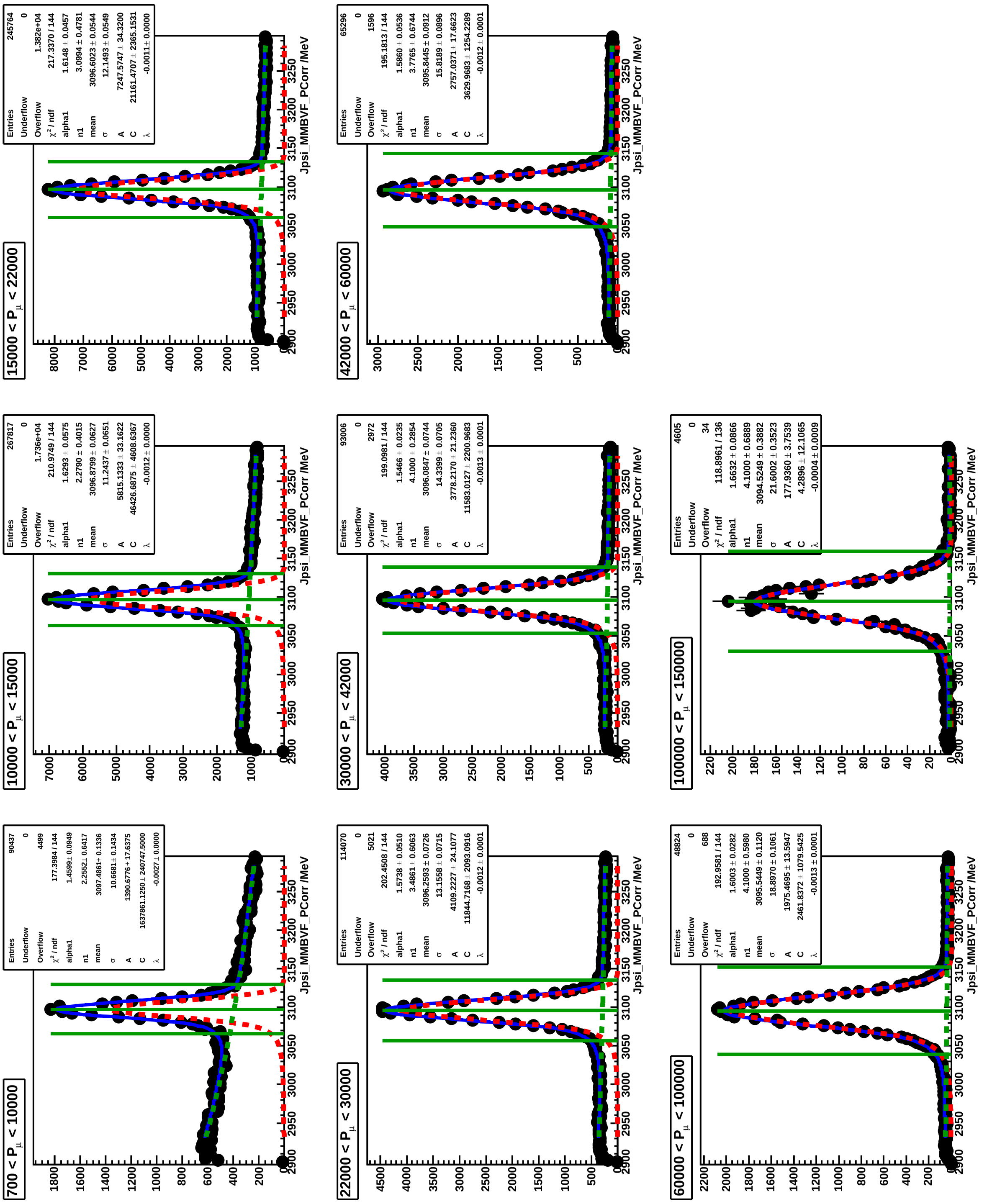

Figure 6.7: Mass histograms in momentum bins for $J/\psi \rightarrow \mu^+\mu^-$ data. In black are the data points, in blue the fit of signal plus background, in red the signal part of the function and in green the background part. The vertical lines in green indicate the size of the signal window which is at 3σ from the fitted mean.

$F(p)$ is sensitive to the amount of underlying background. The $F(p)$ calculation assumes a two-body decay, which is not necessarily true for background. Therefore the method of mass sideband subtraction is applied, which is described in section 6.7.1. Systematic checks revealed, that the method of the sideband subtraction is sensitive to non-Gaussian behaviour of the peaking mass distribution. So the radiative tail on the left side of the mass peak spoils the correction factor $F(p)$ if used (see section 6.8.4) and is responsible for a higher $F(p)$ when the left half of the signal window and the left sideband are used. To study this effect $F(p)$ was determined in three different ways: with the full signal window and both sidebands, with the left half of the signal window and the left sideband and with the right half of the signal window and the right sideband (see plots in appendix F). This bias led to the decision to only use the right side of the signal window and the right sideband to determine $F(p)$.

The correction factor $F(p)$ is determined on the decay $J/\psi \to \mu^+\mu^-$ for each magnet polarity separately (see results in section 6.9.1).

6.6.1 Comparison $F(p)$ and $F_{MC}(p)$ from MC Truth

To verify the calculation of the correction factor $F(p)$ a similar MC quantity was used. $F(p)$ corrects for a wrong error estimate on the momentum. Making use of the MC truth information, the pull κ of the momentum was calculated for each event:

$$\kappa = \frac{p_{\text{rec}} - p_{\text{true}}}{\sigma_p} \quad , \tag{6.14}$$

where p_{rec} is the reconstructed momentum, p_{true} the generated momentum and σ_p the momentum error from the track fit. The quantity similar to $F(p)$ is the RMS of the momentum pull distribution in each of the momentum bins:

$$F_{MC}(p) = \sqrt{\frac{1}{N}\sum_{i=1}^{N} \kappa_i^2} \tag{6.15}$$

N is the number of events in each momentum bin. $F(p)$ and $F_{MC}(p)$ were calculated on the same MC sample and are plotted against the daughter momentum in Figure 6.8. The two quantities agree within the statistical errors except for two momentum bins.

6.6.2 Discussion of the Results

Mass Fit Parameters Data

Table 6.7 shows the parameters χ^2/ndof, the mean and the σ of the Crystal Ball fit to the mass distribution for the different momentum bins. The plots are in Figure 6.7 (in logarithmic scale in appendix D.1). Two trends show up: The trend in the mean towards lower masses with higher momentum and the second trend of a worse mass resolution for high momenta.

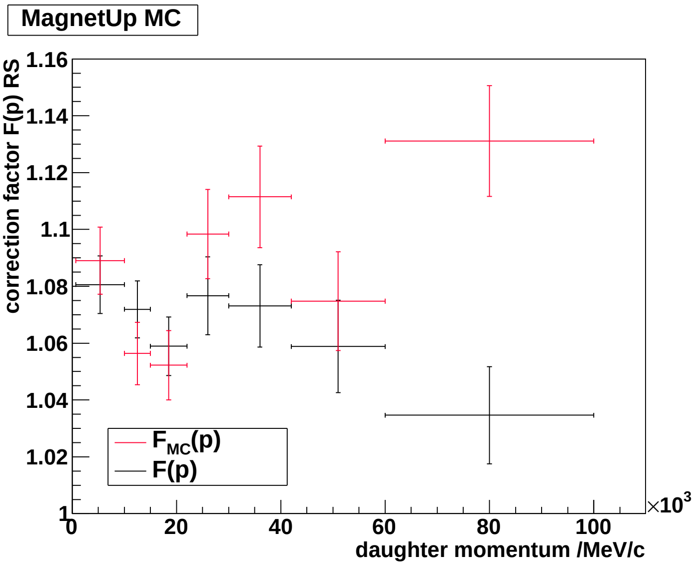

Figure 6.8: $F(p)$ and $F_{MC}(p)$ versus p determined from the same $J/\psi \rightarrow \mu^+\mu^-$MC data set. The statistical errors are shown.

The first trend of the mean can be explained by an imperfect material description in the detector. If each of the particles has to pass more material as it is assumed by the software model for the reconstruction, the mass will be consistently underestimated. According to the Bethe-Bloch formula [34], higher momentum muons lose more energy in material than lower energetic muons. So the effect is more pronounced for the muons in the high momentum bins.

The cause of the second trend, the decreasing mass resolution (an increasing σ) with higher momentum, can be found in the way LHCb measures the track momentum. The magnet bends the trajectories of charged particles and from the track curvature the momentum is calculated. For high momentum particles, the curvature decreases and the error of the curvature measurement increases and therefore the mass resolution decreases for higher momenta.

Mass Fit Parameters MC

The parameters of the mass fit in each momentum bin are presented for MC to compare them with data. The values are shown in Table 6.8 and the plots can be found in appendix D.2 and E. The second trend of a decreasing mass resolution at higher momenta shows up also in MC, since the curvature is less good determined for high momenta and therefore the error on the the momentum measurement bigger. The first trend about the mean is small due to the insertion of the correction factor α from section 6.4.1. A different model for the energy loss of a particle passing through matter was used for the simulation than for the reconstruction. This could explain the remaining bias.

Table 6.7: Mass fit parameters for $J/\psi \rightarrow \mu^+\mu^-$ magnet'up' polarity data from reconstruction 08. The mean of the mass has a bias to lower values for higher muon momenta. The mass resolution (σ) is worse for higher muon momenta.

Momentum Range /MeV/c	χ^2/ndof	mean /MeV/c^2	σ /MeV/c^2
$700 < P_\mu < 10000$	$177.4/144$	3097.49 ± 0.13	10.67 ± 0.14
$10000 < P_\mu < 15000$	$211.0/144$	3096.88 ± 0.06	11.24 ± 0.07
$15000 < P_\mu < 22000$	$217.3/144$	3096.60 ± 0.05	12.15 ± 0.05
$22000 < P_\mu < 30000$	$202.5/144$	3096.26 ± 0.07	13.16 ± 0.07
$30000 < P_\mu < 42000$	$199.1/144$	3096.08 ± 0.07	14.34 ± 0.07
$42000 < P_\mu < 60000$	$195.2/144$	3095.84 ± 0.09	15.82 ± 0.09
$60000 < P_\mu < 100000$	$193/144$	3095.54 ± 0.11	18.90 ± 0.01
$100000 < P_\mu < 150000$	$118.9/136$	3094.52 ± 0.39	21.60 ± 0.35

Table 6.8: Mass fit parameters for $J/\psi \rightarrow \mu^+\mu^-$ MC. The mass resolution σ is reduced for higher muon momenta.

Momentum Range /MeV	χ^2/ndof	mean /MeV	σ /MeV
$700 < P_\mu < 10000$	$63.16/29$	3096.31 ± 0.11	8.88 ± 0.10
$10000 < P_\mu < 15000$	$44.73/27$	3096.21 ± 0.11	9.50 ± 0.09
$15000 < P_\mu < 22000$	$73.71/24$	3096.34 ± 0.11	10.22 ± 0.09
$22000 < P_\mu < 30000$	$80.73/20$	3096.72 ± 0.15	11.07 ± 0.12
$30000 < P_\mu < 42000$	$86.81/21$	3097.00 ± 0.16	11.70 ± 0.13
$42000 < P_\mu < 60000$	$97.28/20$	3097.10 ± 0.19	12.49 ± 0.16
$60000 < P_\mu < 100000$	$57.79/23$	3098.10 ± 0.23	14.35 ± 0.20

6.7 Sideband subtraction

The idea of the sideband subtraction method is to get the shape of a distribution without background pollution. The method of the sideband subtraction is described for arbitrary distributions (different from the mass distribution) in four steps:

1. **Mass histogram:**
   The mass distribution is fitted. A signal window is chosen such that a large fraction of signal events are contained. This splits the mass distribution into a signal region and a sideband region, where the sideband region consists of the left and right sideband. The number of signal- and background events is calculated in the signal region (see Figure 6.5).

2. **Signal+background histogram:**
   The distribution, which needs the sideband subtraction (for example the momentum distribution) is plotted for the signal region of the mass distribution.

3. **Background histogram:**
   The distribution which needs sideband subtraction is plotted for the sideband region of the mass distribution. Then it is scaled to the number of background events in the signal region of the mass distribution.

4. **Sideband subtraction:**
   The background histogram (from $3.$) is subtracted from the signal+background histogram (from $2.$). This is now the sideband-subtracted distribution for the signal window. [4]

The mass distribution is fitted with a Crystal Ball function plus an exponential background. The size of the signal window was chosen by systematic studies described in the section 6.8.4 and was set to a size of 3 standard deviations from the Gaussian mean of the Crystal Ball function. The sidebands start at around 5σ on each side (at 3030 MeV/c^2 and at 3160 MeV/c^2 for $J/\psi \to \mu^+\mu^-$). The number of signal (background) events is calculated by integrating over the fitted mass signal (background) distribution in the mass signal window.

6.7.1 Sideband Subtraction for the Correction Factor $F(p)$

The sideband subtraction for $F(p)$ is described in three steps which are done for each momentum bin:

1. $F^2(p)$ for signal+background:
   Calculate $F_i^2(p_{\text{bin}})$ for each event in the signal window from Equation 6.13. $F^2(p)$ is the mean of this distribution. For the error on $F^2(p)$ the statistical error of the mean is taken.

---

[4] Another approach does fit the background distribution and subtracts then the fitted distribution.

2. $F^2_{\text{bkg}}(p)$:
   Compute $F^2_{\text{bkg}}(p)$ as described below.

3. $F^2_{\text{Signal}}(p)$:
   Subtract $F^2_{\text{bkg}}(p)$ quadratically from $F^2(p)$ and obtain $F^2_{\text{Signal}}(p)$ as in Equation (6.16). S is number of signal events and B the number of background events in the signal region.

$$F_{\text{Signal}}(p) = \sqrt{\frac{(S+B)\cdot F^2(p) - B\cdot F^2_{\text{bkg}}(p)}{S}} \tag{6.16}$$

The second step about the calculation of $F^2_{\text{bkg}}(p)$ is described now. A simple sideband subtraction cannot be used since the mass distribution itself is used to extract the correction factor $F(p)$. This means the term $(m_{\text{rec}} - m_{\text{mean}})^2$ in Equation 6.13 cannot be used for background events, since it is not describing the events in the signal region below the peak but also the ones in the sideband region. So $(m_{\text{rec}} - m_{\text{mean}})^2$ is replaced by the expectation value of the analytical term representing the fitted background distribution in the signal window.

The background is fitted by an exponential distribution $p(x) = C \cdot e^{\lambda x}$. The expectation value replacing $(m_{\text{rec}} - m_{\text{mean}}) \equiv (x-\mu)$ is calculated as follows:

$$\begin{aligned}
\langle (x-\mu)^2 \rangle &= \frac{\int_a^b (x-\mu)^2 \cdot p(x)dx}{\int_a^b p(x)dx} && (6.17)\\
&= \frac{\int_a^b (x-\mu)^2 \cdot C \cdot e^{\lambda x} dx}{\int_a^b C\cdot e^{\lambda x} dx} && (6.18)\\
&= \frac{\left[\frac{C}{\lambda^3}\cdot e^{\lambda x}\left(\lambda^2(\mu-x)^2 + 2\lambda(\mu-x)+2\right)\right]_a^b}{\left[\frac{C}{\lambda}e^{\lambda x}\right]_a^b} \quad , && (6.19)
\end{aligned}$$

where a and b are the lower and the upper bound of the signal window and $\int_a^b p(x)dx$ is needed for proper normalisation.
Equation 6.19 is plugged into Equation 6.13 for the term $(m_{\text{rec}} - m_{\text{mean}})^2$. All other terms in Equation 6.13 are taken from events in the sidebands. It is assumed that background events from the sidebands provide a good estimate of background events in the signal window.

Figure 6.9 shows the result of the third step of the sideband subtraction: $F^2_{\text{Signal}}(p)$ for the different momentum bins. The Figures for step one and two can be found in appendix F. The values of $F^2_{\text{Signal}}(p)$ are listed and plotted in the results section 6.9.1 and Figures 6.10 and 6.11 show the σ_M distribution and the mass pull distribution with $F^2_{\text{Signal}}(p)$ applied.

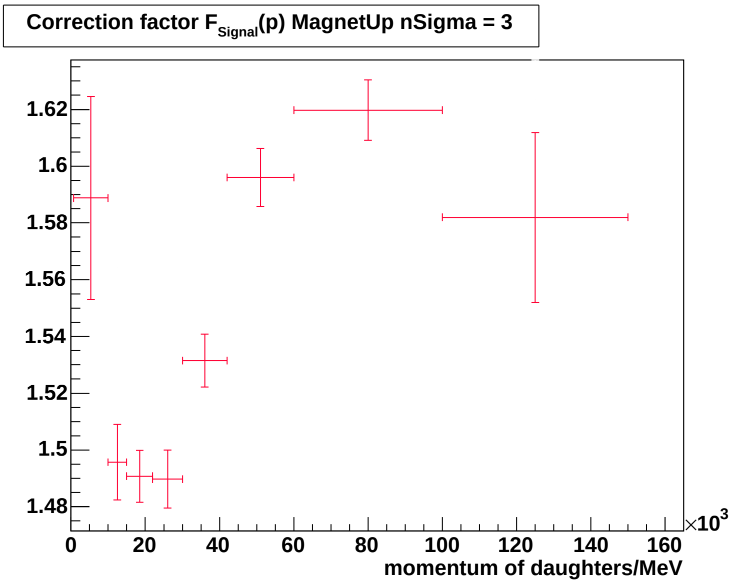

Figure 6.9: Correction factor $F_{\text{Signal}}(p)$ after sideband subtraction of the background.

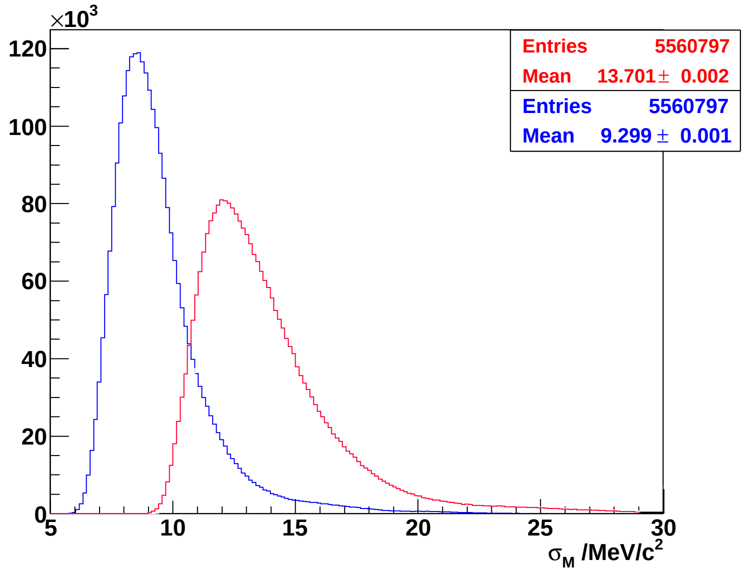

Figure 6.10: Distribution of per event calculated mass error σ_M (blue) for the decay $J/\psi \to \mu^+\mu^-$ magnet 'up' polarity. In red the σ_M was corrected with $F_{\text{Signal}}(p)$.

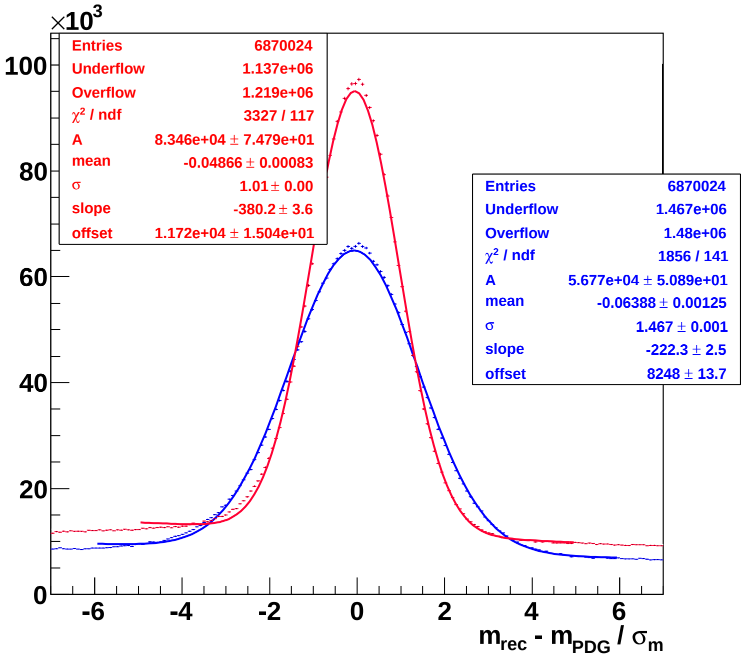

Figure 6.11: Mass pull distribution of the $J/\psi \to \mu^+\mu^-$ magnet 'up' data sample, fitted with a Gaussian on a linear background. $m_{\rm rec}$ is the reconstructed mother mass, $m_{\rm PDG}$ acts as the 'true' value of the mother mass and is taken from Ref. [34]. The σ of the pull is unity if the errors are estimated correctly. Clearly the error is underestimated for the uncorrected momenta (blue). This improves if $F_{\rm Signal}(p)$ is applied (red).

6.8 Systematic Analysis

’You can never prove that an analysis is perfect, but the more checks you perform successfully, the greater the credibility of the result.’[50]

The checks performed on this analysis are described. Some of the the checks revealed systematic effects which are taken into account for the systematic error.

6.8.1 Selection Cuts

The goal was to keep the bias on the mass resolution as low as possible. Cuts on the particle identification were avoided, since they bias the sample towards higher momenta. No lifetime cuts were applied.

6.8.2 Background Parameterisation

Different background parameterisations have been applied. For the full mass peak of the J/ψ a constant, linear or exponential background can be used (Figure 6.5). However looking at the mass peak in bins of momentum (Figure 6.7), the linear and constant backgrounds do not fit well in the lower momentum bins and hence the exponential background parametrisation was chosen. However, the method for calculating the event-by-event error on the reconstructed invariant mass (section 6.7.1) could be modified — if needed — and used with all of these background models.

6.8.3 Signal Parameterisation

Different signal parameterisations have been tried: single Gaussian, double Crystal Ball function and single Crystal Ball function. The single sided Crystal Ball function was chosen, since there is a physical tail on the left side of the mass coming from radiative decays. The double Crystal ball function was not chosen because of low statistics in some momentum bins. For the B-decays in section — where the the number of events are even less — a single Gaussian parameterisation was chosen 6.9.1.

6.8.4 Size of the Signal Window

The influence of the size of the signal window on the pull was evaluated in a range from 1–7 standard deviations from the fitted Gaussian mean of the Crystal Ball function of the mass histogram. Ideally the signal window is chosen as large as possible, since a bias is introduced on the pull by cutting tails of a Gaussian distribution at < 4 standard deviations σ. The presence and the size of this effect was verified with a toy MC study and the result is presented in Table 6.9. But non-Gaussian tails [5] on both sides of the mass peak bias the pull as well. Thus a

---

[5] For the non-Gaussian tails see the logarithmic mass plots in appendix D.1

window as small as possible is favoured to suppress the influence of these tails as much as possible. For this study these two effects bias the pull in opposite ways and cancel at a window of around 3σ as can be seen in Table 6.9. Therefore the window size of 3σ is chosen. A systematic error is assigned to the pull for bias observed when varying the window size between 1–7σ.

The non-Gaussian tails are visible in MC as well (see Table 6.10). Invariant mass plots show a start of the non-Gaussian tails at around 3σ (appendix D.2), on the right side of the fitted mean. On the left side, the radiative tail and the effect of the non-Gaussian tail is much more pronounced. Therefore only the right side was used to determine the correction factor $F(p)$ in order to be affected only of a weakened form of this non-Gaussian tail effect. All distributions from 7 to 1 standard deviation are shown in the appendix H. By choosing progressively smaller signal windows, the difference between left and right vanishes.

6.8.5 Diagonal and Off-Diagonal Data Subsets

The method to determine the correction factor $F(p)$ uses only events where the two muon momenta are in the same momentum bin. These events are called 'diagonal' in the following. Accordingly the events where the two muon momenta are in different bins are called 'off diagonal'. To investigate a possible bias coming from the use of this diagonal sub sample for $F(p)$, the pull of the total sample is compared to the pull of the diagonal sub sample (Table 6.9). The full sample can be regarded as almost unbiased, since only 14.5% of the events were used to determine the correction factor $F(p)$. Table 6.9 shows a deviation of 0.2% from 1.0 for the diagonal sub sample for the 3σ window while the total sample shows a deviation of 1% from 1.0. For the 3σ window this bias will be part of the systematic error.

6.8.6 Variation of the Fitted Mean of the Mass Peak

The effect of a variation of the parameter m_{mean} in the calculation of $F(p)$ (Equation (6.13)) was investigated. The test was done for each momentum bin since the statistics varies for the different bins. The value of m_{mean} was shifted in both directions by the amount of the statistical error given by the fit of the mass spectrum (see Table 6.7). Then the correction factor $F(p)$ was recalculated using the shifted means. The maximum deviation of the two shifted $F(p)$ to the un-shifted $F(p)$ was taken into account as a systematic error (section 6.8.7).

6.8.7 Systematic Errors

The following sources of systematic errors on $F(p)$ have been identified through cross-checks in previous sections:

1. The bias introduced by determining $F(p)$ only on the diagonal subset, but applying it to the full data set. This systematic error B is the deviation of

Table 6.9: Pull for different sizes of the signal window for $J/\psi \rightarrow \mu^+\mu^-$ data from magnet 'up' and reconstruction 08.

μ^{+-} **momentum /GeV**	2σ	2.7σ	2.8σ	2.9σ	3σ	3.1σ	3.2σ	3.3σ	4σ	5σ	6σ	7σ
0.7-10	1.109	0.982	0.982	0.982	0.981	0.977	0.964	0.964	0.917	0.916	0.904	0.944
10-15	1.130	1.017	1.009	1.001	0.995	0.986	0.981	0.979	0.947	0.957	0.935	1.002
15-22	1.126	1.019	1.013	1.003	0.994	0.988	0.988	0.984	0.956	0.957	0.947	0.958
22-30	1.138	1.026	1.020	1.012	1.006	0.999	0.995	0.987	0.968	0.960	0.953	0.976
30-42	1.139	1.029	1.023	1.017	1.011	1.009	1.002	0.998	0.978	0.968	0.981	0.989
42-60	1.129	1.019	1.013	1.004	0.998	0.994	0.989	0.986	0.969	0.972	0.970	0.977
60-100	1.130	1.030	1.023	1.015	1.009	1.005	1.001	0.996	0.988	0.985	0.983	1.004
100-150	1.109	1.029	1.006	1.005	0.996	0.987	0.981	0.981	0.966	0.966	0.966	0.934
Total pull of Diagonals	1.129	1.019	1.013	1.005	0.998	0.993	0.989	0.985	0.961	0.961	0.954	0.978
stat. Error	0.002	0.002	0.002	0.002	0.002	0.002	0.002	0.002	0.002	0.002	0.002	0.002
deviation from 1.0 in %	12.90	1.90	1.30	0.50	0.20	0.70	1.10	1.50	3.90	3.90	4.60	2.20
Total pull	1.141	1.030	1.024	1.016	1.010	1.005	1.000	0.996	0.973	0.972	0.966	0.988
stat. error	0.001	0.001	0.001	0.001	0.001	0.001	0.001	0.001	0.001	0.001	0.001	0.001
deviation from 1.0 in %	14.10	3.00	2.40	1.60	1.00	0.50	0.03	0.43	2.72	2.85	3.38	1.24
Pull from Gaussian toy MC	1.167	1.033	1.026	1.021	1.016	1.012	1.009	1.006	1.000	0.999	1.000	1.001
dev Gaussian from total pull in %	2.28	0.29	0.2	0.49	0.59	0.7	0.93	1.03	2.84	2.83	3.46	1.33

Table 6.10: Pull for different sizes of the signal window for $J/\psi \to \mu^+\mu^-$ MC.

Window size /σ	Pull RS
2	1.169 ± 0.002
3	1.043 ± 0.002
4	1.018 ± 0.001
5	0.9999 ± 0.0014
6	0.9924 ± 0.0014
7	0.9891 ± 0.0014

the total pull from the nominal value 1.0 for the 3σ window (Table 6.9, row 'Total pull of Diagonals').

2. The combined effect of cutting the tails of a Gaussian and the non-Gaussian tails of the mass spectrum. The systematic error C introduced by this effect is the deviation of the pull from the Gaussian toy MC to the nominal value 1.0 for the 3σ window (Table 6.9, row 'Pull from Gaussian toy MC').
3. The uncertainty S on the fitted mean of the mass peak. It is the only systematics determined for each momentum bin i individually.

The three quantities were assumed to be fairly uncorrelated. Thus the relative systematic error r_i on $F(p)$ per bin is calculated as in Equation 6.20.

$$r_i = \sqrt{B^2 + C^2 + S_i^2} \tag{6.20}$$

$$= \sqrt{1.0\%^2 + 1.6\%^2 + S_i^2} \tag{6.21}$$

In Table 6.11 the systematic errors S_i for all momentum bins are collected for the 3σ window and the relative systematic error r_i is evaluated for each bin. Then the weighted mean of r_i is calculated according to the statistics in each momentum bin and the overall systematic error is found to be 1.96%. This error can be directly propagated to the pull and the error on the mass resolution σ_M.

Figure 6.12 shows the pull for the different momentum bins with the quadratically added statistical and systematic error, for the diagonal subset[6]. It agrees very well within the errors with the nominal value 1.0.

6.9 Results

6.9.1 Evaluation with Different Two-Body Decays

The track reconstruction and momentum measurement in LHCb is to first order independent of the decay topology. Therefore the correction factors $F(p)$ should

---

[6] Since the diagonal subset was used to determine $F(p)$ the results in the plot are biased.

Table 6.11: Correction factors $F_{\text{Signal}}(p)$. The data is from the $J/\psi \rightarrow \mu^+\mu^-$ decay, magnet 'up' polarity and binned in momentum, with its statistical and systematic errors.

momentum bins /GeV	$F_{\text{Signal}}(p)$	uncorrel. syst. error S_i	total syst. error r_i(Fp)
0.7–10	$1.589 \pm 2.3\%$	1.3%	2.3%
10–15	$1.496 \pm 0.9\%$	0.5%	1.9%
15–22	$1.491 \pm 0.6\%$	0.3%	1.9%
22–30	$1.490 \pm 0.7\%$	0.4%	1.9%
30–42	$1.532 \pm 0.6\%$	0.3%	1.9%
42–60	$1.596 \pm 0.6\%$	0.3%	1.9%
60–100	$1.620 \pm 0.7\%$	0.3%	1.9%
100–150	$1.582 \pm 1.9\%$	0.9%	2.1%
weighted mean			1.96%

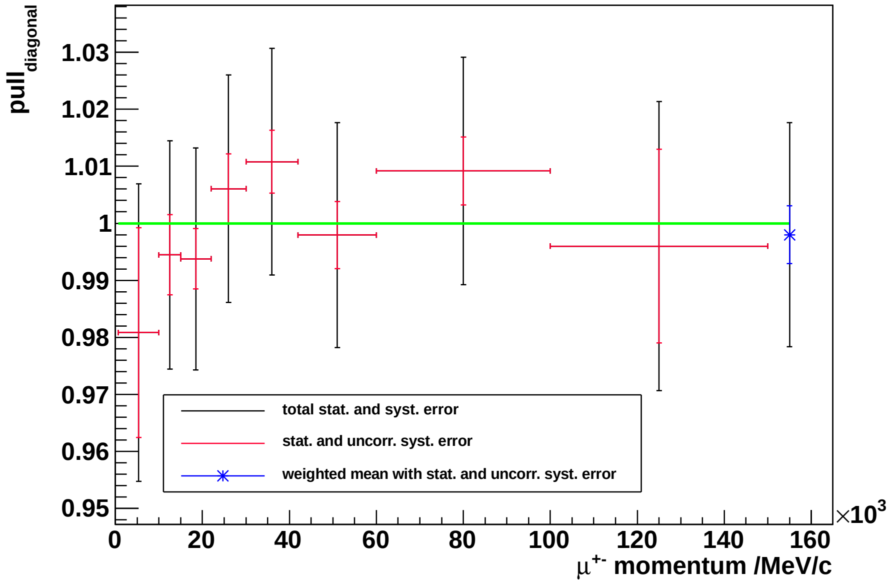

Figure 6.12: Pull of the mass with statistical and systematic error for each momentum bin in red. In blue the total pull of the diagonal sample is shown having assigned the weighted mean as systematic error. All the data points are very well compatible within the errors with the nominal value 1.0 (green).

Table 6.12: $F_{\text{Signal}}(p)$ with statistical and systematic error for $J/\psi \to \mu^+\mu^-$ magnet up polarity.

Momentum Range /MeV	$F_{\text{Signal}}(p)$±stat±sys
$700 < p_\mu < 10000$	$1.589 \pm 0.036 \pm 0.037$
$10000 < p_\mu < 15000$	$1.496 \pm 0.013 \pm 0.029$
$15000 < p_\mu < 22000$	$1.491 \pm 0.009 \pm 0.029$
$22000 < p_\mu < 30000$	$1.490 \pm 0.01 \pm 0.029$
$30000 < p_\mu < 42000$	$1.532 \pm 0.009 \pm 0.029$
$42000 < p_\mu < 60000$	$1.596 \pm 0.01 \pm 0.031$
$60000 < p_\mu < 100000$	$1.620 \pm 0.011 \pm 0.031$
$100000 < p_\mu < 150000$	$1.582 \pm 0.03 \pm 0.033$

Table 6.13: $F_{\text{Signal}}(p)$ with statistical and systematic error for $J/\psi \to \mu^+\mu^-$ magnet down polarity.

Momentum Range /MeV	$F(_{\text{Signal}}p)$ ±stat±sys
$700 < p_\mu < 10000$	$1.655 \pm 0.042 \pm 0.038$
$10000 < p_\mu < 15000$	$1.483 \pm 0.019 \pm 0.029$
$15000 < p_\mu < 22000$	$1.487 \pm 0.014 \pm 0.028$
$22000 < p_\mu < 30000$	$1.512 \pm 0.016 \pm 0.029$
$30000 < p_\mu < 42000$	$1.580 \pm 0.014 \pm 0.03$
$42000 < p_\mu < 60000$	$1.651 \pm 0.015 \pm 0.032$
$60000 < p_\mu < 100000$	$1.657 \pm 0.015 \pm 0.032$
$100000 < p_\mu < 150000$	$1.642 \pm 0.047 \pm 0.034$

be valid for arbitrary decays reconstructed from long tracks.

Tables 6.12 and 6.13 show the results for the correction factors $F_{\text{Signal}}(p)$ with their statistical- and systematic uncertainty, determined from the $J/\psi \to \mu^+\mu^-$ decay for magnet 'up' and magnet 'down' polarity. Figures 6.13 and 6.14 show the plots of the results in Tables 6.12 and 6.13.

The set of $F_{\text{Signal}}(p)$s was applied to the different two-body decays listed in Table 6.14. σ_M was calculated for each event for the different decays with Equation 6.12 using the correction factors from Table 6.12 or 6.13. Table 6.14 presents the mean of the σ_M distribution, which is compared to the width σ_{fit} of the Crystal Ball function or the Gaussian, which were fitted to the full mass spectra. The means of the σ_M distributions and the σ_{fit} show a good agreement for all decays except for $\Upsilon \to \mu^+\mu^-$. In addition the means of the σ_M distributions agree with each other for the different B decays.

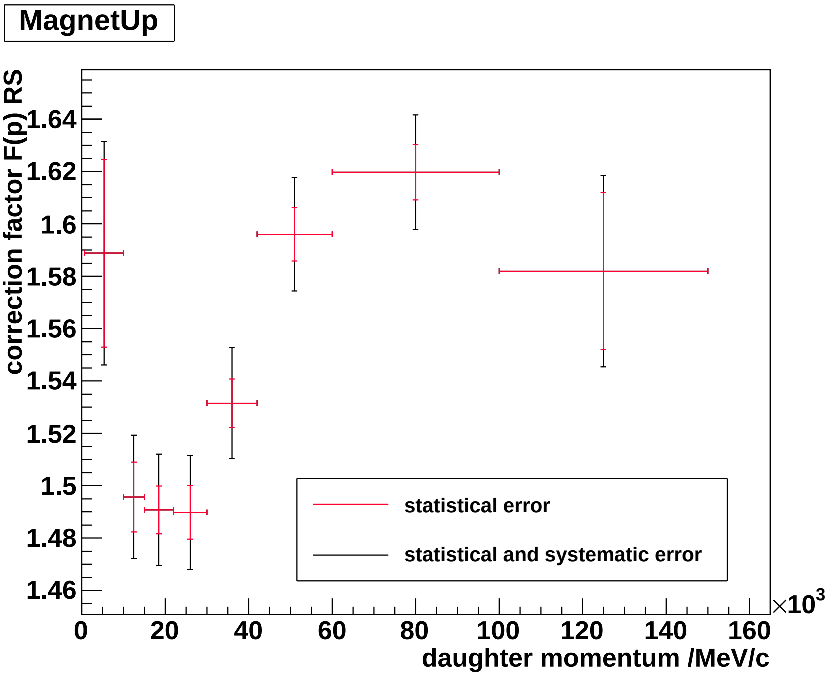

Figure 6.13: Results from Table 6.12.

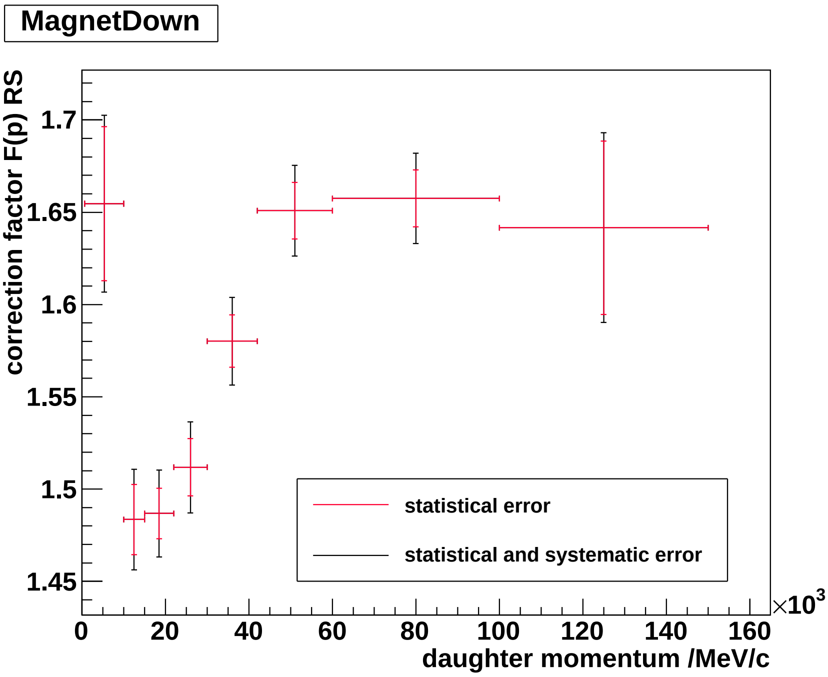

Figure 6.14: Results from Table 6.13.

Table 6.14: Correction factor $F_{\text{Signal}}(p)$ applied to different decays. The quantity measuring the goodness of the method is the pull. The pull is compatible with 1.0 for all the investigated decays.

Decay	Mag.	mean σ_M /MeV	σ_{fit} /MeV	σ_{pull}±stat±sys
$J/\Psi \to \mu^+\mu^-$	up	$13.701 \pm 0.002 \pm 0.269$	13.60 ± 0.01	$1.010 \pm 0.001 \pm 0.020$
$J/\Psi \to \mu^+\mu^-$	down	$13.880 \pm 0.002 \pm 0.272$	13.62 ± 0.02	$0.998 \pm 0.001 \pm 0.020$
$\Upsilon \to \mu^+\mu^-$	up	$48.750 \pm 0.058 \pm 0.956$	45.15 ± 0.66	$0.979 \pm 0.011 \pm 0.019$
$\Upsilon \to \mu^+\mu^-$	down	$49.599 \pm 0.091 \pm 0.972$	47.37 ± 0.82	$1.001 \pm 0.017 \pm 0.020$
$B_s^0 \to K^+K^-$	up	$26.112 \pm 0.355 \pm 0.512$	25.03 ± 3.21	$1.109 \pm 0.113 \pm 0.022$
$B_d^0 \to K^\pm\pi^\mp$	up	$24.687 \pm 0.237 \pm 0.484$	24.42 ± 1.52	$1.006 \pm 0.065 \pm 0.020$
$B_d^0 \to \pi^+\pi^-$	up	$26.145 \pm 0.279 \pm 0.512$	23.98 ± 3.20	$1.052 \pm 0.118 \pm 0.021$
$B_s^0 \to K^+K^-$	down	not enough	data	(TT cold)
$B_d^0 \to K^\pm\pi^\mp$	down	$25.183 \pm 0.331 \pm 0.494$	24.68 ± 2.59	$1.027 \pm 0.100 \pm 0.020$
$B_d^0 \to \pi^+\pi^-$	down	not enough	data	(TT cold)

The quantity measuring the goodness of the error estimate σ_M and $F(p)$ is the Gaussian width σ_{pull} of the invariant mass pull distribution. A width σ_{pull} of 1.0 means the errors on the event-by-event invariant mass are correctly estimated. This is the case for all the investigated decays. Their pulls agree with 1.0 within the errors, thus $F_{\text{Signal}}(p)$ corrects for a wrong momentum estimate.

Conclusion

The Tracker Turicensis at the LHCb experiment was successfully commissioned with more than 99.7% working channels for a total number of about 143000 channels in October 2009. The control- and safety system works reliably and allowed the tuning of hard- and software parameters during injection tests before proton-proton collisions happened in the LHC.

Mass resolution studies led to a better understanding of the track reconstruction of the LHCb experiment. In view of $B_s^0 \to \mu^+\mu^-$ analysis the most important results are:

1. The successful development of a method for calculating the uncertainty σ_M on the mass per event.
2. The calculation of momentum dependent correction factors $F_{\text{Signal}}(p)$ to calibrate the error estimate of the track momentum.
3. The reduction of the systematic error on the mass resolution to 1.96%, using the developed method and the correction factors.

Appendices

Appendix A

Parametrisation of track parameters

A.1 Parametrisation of tx, ty, q/p to p_1, p_2 and $\cos\Theta$

$$cos\Theta = cos\Theta(t_{x_1}, t_{y_1}, t_{x_2}, t_{y_2}) = \frac{t_{x_1}t_{x_2} + t_{y_1}t_{y_2} + 1}{\sqrt{t_{x_1}^2 + t_{y_1}^2 + 1}\sqrt{t_{x_2}^2 + t_{y_2}^2 + 1}} \tag{A.1}$$

$$|p_1| = |p_1|(q_1) = (\frac{q_1}{|p_1|})^{-1} \cdot q_1 \tag{A.2}$$

$$cov(|p_1|, |p_2|, cos\Theta) = G \cdot V_{cov} \cdot G^T \tag{A.3}$$

with V_{cov} the covariance matrix of $t_{x_1}, t_{y_1}, q_1/|p_1|, t_{x_2}, t_{y_2}, q_2/|p_2|$ and

$$G = \begin{pmatrix} \frac{\partial|p_1|}{\partial t_{x_1}} & \frac{\partial|p_1|}{\partial t_{y_1}} & \frac{\partial|p_1|}{\partial q/|p_1|} & \frac{\partial|p_1|}{\partial t_{x_2}} & \frac{\partial|p_1|}{\partial t_{y_2}} & \frac{\partial|p_1|}{\partial q/|p_2|} \\ \frac{\partial|p_2|}{\partial t_{x_1}} & \frac{\partial|p_2|}{\partial t_{y_1}} & \frac{\partial|p_2|}{\partial q/|p_1|} & \frac{\partial|p_2|}{\partial t_{x_2}} & \frac{\partial|p_2|}{\partial t_{y_2}} & \frac{\partial|p_2|}{\partial q/|p_2|} \\ \frac{\partial cos\Theta}{\partial t_{x_1}} & \frac{\partial cos\Theta}{\partial t_{y_1}} & \frac{\partial cos\Theta}{\partial q/|p_1|} & \frac{\partial cos\Theta}{\partial t_{x_2}} & \frac{\partial cos\Theta}{\partial t_{y_2}} & \frac{\partial cos\Theta}{\partial q/|p_2|} \end{pmatrix} \tag{A.4}$$

$$= \begin{pmatrix} 0 & 0 & -\frac{|p_1|^2}{q_1} & 0 & 0 & 0 \\ 0 & 0 & 0 & 0 & 0 & -\frac{|p_2|^2}{q_2} \\ A & B & 0 & C & D & 0 \end{pmatrix} \tag{A.5}$$

$$A = \frac{t_{x_2}}{\sqrt{{t_{x_1}}^2 + {t_{y_1}}^2 + 1}\sqrt{{t_{x_2}}^2 + {t_{y_2}}^2 + 1}} - \frac{(t_{x_1}\,t_{x_2} + t_{y_1}\,t_{y_2} + 1)\,t_{x_1}}{({t_{x_1}}^2 + {t_{y_1}}^2 + 1)^{3/2}\,\sqrt{{t_{x_2}}^2 + {t_{y_2}}^2 + 1}} \tag{A.6}$$

$$B = \frac{t_{y_2}}{\sqrt{{t_{x_1}}^2+{t_{y_1}}^2+1}\sqrt{{t_{x_2}}^2+{t_{y_2}}^2+1}} - \frac{(t_{x_1}\,t_{x_2}+t_{y_1}\,t_{y_2}+1)\,t_{y_1}}{({t_{x_1}}^2+{t_{y_1}}^2+1)^{3/2}\,\sqrt{{t_{x_2}}^2+{t_{y_2}}^2+1}} \tag{A.7}$$

$$C = \frac{t_{x_1}}{\sqrt{{t_{x_1}}^2+{t_{y_1}}^2+1}\sqrt{{t_{x_2}}^2+{t_{y_2}}^2+1}} - \frac{(t_{x_1}\,t_{x_2}+t_{y_1}\,t_{y_2}+1)\,t_{x_2}}{\sqrt{{t_{x_1}}^2+{t_{y_1}}^2+1}\,({t_{x_2}}^2+{t_{y_2}}^2+1)^{3/2}} \tag{A.8}$$

$$D = \frac{t_{y_1}}{\sqrt{{t_{x_1}}^2+{t_{y_1}}^2+1}\sqrt{{t_{x_2}}^2+{t_{y_2}}^2+1}} - \frac{(t_{x_1}\,t_{x_2}+t_{y_1}\,t_{y_2}+1)\,t_{y_2}}{\sqrt{{t_{x_1}}^2+{t_{y_1}}^2+1}\,({t_{x_2}}^2+{t_{y_2}}^2+1)^{3/2}} \tag{A.9}$$

A.2 Parametrisation of p_x, p_y and p_z to p_1, p_2 and $\cos\Theta$

$$cos\Theta = cos\Theta(p_{x_1}, p_{y_1}, p_{z_1}, p_{x_2}, p_{y_2}, p_{z_2}) = \frac{p_{x_1}p_{x_2}+p_{y_1}p_{y_2}+p_{z_1}p_{z_2}}{|p_1||p_2|} \tag{A.10}$$

$$|p_1| = |p_1|(p_{x_1}, p_{y_1}, p_{z_1}) = \sqrt{p_{x_1}^2+p_{y_1}^2+p_{z_1}^2} \tag{A.11}$$

$$cov(|p_1|, |p_2|, cos\Theta) = G \cdot V_{cov} \cdot G^T \tag{A.12}$$

with V_{cov} the covariance matrix of $p_{x_1}, p_{y_1}, p_{z_1}, p_{x_2}, p_{y_2}, p_{z_2}$ and

$$G = \begin{pmatrix} \frac{\partial|p_1|}{\partial p_{x_1}} & \frac{\partial|p_1|}{\partial p_{y_1}} & \frac{\partial|p_1|}{\partial p_{z_1}} & \frac{\partial|p_1|}{\partial p_{x_2}} & \frac{\partial|p_1|}{\partial p_{y_2}} & \frac{\partial|p_1|}{\partial p_{z_2}} \\ \frac{\partial|p_2|}{\partial p_{x_1}} & \frac{\partial|p_2|}{\partial p_{y_1}} & \frac{\partial|p_2|}{\partial p_{z_1}} & \frac{\partial|p_2|}{\partial p_{x_2}} & \frac{\partial|p_2|}{\partial p_{y_2}} & \frac{\partial|p_2|}{\partial p_{z_2}} \\ \frac{\partial cos\Theta}{\partial p_{x_1}} & \frac{\partial cos\Theta}{\partial p_{y_1}} & \frac{\partial cos\Theta}{\partial p_{z_1}} & \frac{\partial cos\Theta}{\partial p_{x_2}} & \frac{\partial cos\Theta}{\partial p_{y_2}} & \frac{\partial cos\Theta}{\partial p_{z_2}} \end{pmatrix} \tag{A.13}$$

$$\frac{\partial|p_1|}{\partial p_{x_1}} = \frac{p_{x_1}}{|p_1|} \tag{A.14}$$

$$\frac{\partial|p_1|}{\partial p_{y_1}} = \frac{p_{y_1}}{|p_1|} \tag{A.15}$$

$$\frac{\partial|p_1|}{\partial p_{z_1}} = \frac{p_{z_1}}{|p_1|} \tag{A.16}$$

$$\frac{\partial|p_1|}{\partial p_{x_2}} = \frac{\partial|p_1|}{\partial p_{y_2}} = \frac{\partial|p_1|}{\partial p_{z_2}} = \frac{\partial|p_2|}{\partial p_{x_1}} = \frac{\partial|p_2|}{\partial p_{y_1}} = \frac{\partial|p_2|}{\partial p_{z_1}} = 0 \tag{A.17}$$

$$\frac{\partial|p_2|}{\partial p_{x_2}} = \frac{p_{x_2}}{|p_2|} \tag{A.18}$$

$$\frac{\partial|p_2|}{\partial p_{y_2}} = \frac{p_{y_2}}{|p_2|} \tag{A.19}$$

$$\frac{\partial|p_2|}{\partial p_{z_2}} = \frac{p_{z_2}}{|p_2|} \tag{A.20}$$

$$\frac{\partial cos\Theta}{\partial p_{x_1}} = \frac{p_{x_2}}{|p_1||p_2|} - \frac{(p_{x_1}p_{x_2} + p_{y_1}p_{y_2} + p_{z_1}p_{z_2})p_{x_1}}{|p_1|^3|p_2|} \tag{A.21}$$

$$\frac{\partial cos\Theta}{\partial p_{y_1}} = \frac{p_{y_2}}{|p_1||p_2|} - \frac{(p_{x_1}p_{x_2} + p_{y_1}p_{y_2} + p_{z_1}p_{z_2})p_{y_1}}{|p_1|^3|p_2|} \tag{A.22}$$

$$\frac{\partial cos\Theta}{\partial p_{z_1}} = \frac{p_{z_2}}{|p_1||p_2|} - \frac{(p_{x_1}p_{x_2} + p_{y_1}p_{y_2} + p_{z_1}p_{z_2})p_{z_1}}{|p_1|^3|p_2|} \tag{A.23}$$

$$\frac{\partial cos\Theta}{\partial p_{x_2}} = \frac{p_{x_1}}{|p_1||p_2|} - \frac{(p_{x_1}p_{x_2} + p_{y_1}p_{y_2} + p_{z_1}p_{z_2})p_{x_2}}{|p_1||p_2|^3} \tag{A.24}$$

$$\frac{\partial cos\Theta}{\partial p_{y_2}} = \frac{p_{y_1}}{|p_1||p_2|} - \frac{(p_{x_1}p_{x_2} + p_{y_1}p_{y_2} + p_{z_1}p_{z_2})p_{y_2}}{|p_1||p_2|^3} \tag{A.25}$$

$$\frac{\partial cos\Theta}{\partial p_{z_2}} = \frac{p_{z_1}}{|p_1||p_2|} - \frac{(p_{x_1}p_{x_2} + p_{y_1}p_{y_2} + p_{z_1}p_{z_2})p_{z_2}}{|p_1||p_2|^3} \tag{A.26}$$

Appendix B

Selection Cuts

The following tables present the selection cuts for the three investigated decays: $B_s^0 \to \mu^+\mu^-$, $K_s^0 \to \pi^+\pi^-$ and $J/\psi \to \mu^+\mu^-$. IP stands for impact parameter, PV for primary vertex, p for momentum, $\text{p}_\top$ for transverse momentum, q for the electric charge, PIDK for particle ID of the Kaon, PIDp for particle ID of the proton, DOCA for distance of closest approach between two tracks, DIRA for the cosine of the angle between the particle momentum and the vector from the primary to the secondary vertex.

Table B.1: Selection cuts for $B_s^0 \to \mu^+\mu^-$ MC.

cut variable	condition	
track and PV χ^2_{IP}/ndf	$>$	12.25
B_s^0 mass	$\pm$	600 MeV
B_s^0 vertex χ^2	$<$	14
B_s^0 vertex distance significance	$>$	12
B_s^0 and PV χ^2_{IP}/ndf	$<$	36
B_s^0 $\text{p}_\top$	$>$	700 MeV

Table B.2: Selection cuts for $K_s^0 \to \pi^+\pi^-$ data and MC. Subscript 1 and 2 stand for the two daughter particles (pions), subscript M stands for the mother particle (K_s^0).

cut variable	condition	
log((IP_PV$_1\cdot$ IP_PV$_2)/$ IP_PV$_M$)	$>$	0.755
K_s^0 p$_\mathrm{T}$ /MeV	$>$	150
K_s^0 DOCA$_M$ /mm	$<$	5
K_s^0 vertex χ^2	$<$	30
K_s^0 DIRA /rad	$>$	0.9999

Table B.3: Selection cuts for $J/\psi \to \mu^+\mu^-$ and $\Upsilon \to \mu^+\mu^-$ data and MC.

cut variable	condition	
mother mass	$\pm$	250 MeV
mother vertex χ^2	$<$	11
track χ^2/ndf	$<$	4
$\mu^\pm$ PIDmu	$>$	0
$\mu^\pm$ isMuon	$=$	1

Table B.4: Selection cuts for $B_s^0 \to K^+K^-$ data.

cut variable	condition	
B_s^0 mass	$\pm$	250 MeV
B_s^0 vertex χ^2	$<$	5
B_s^0 DOCA	$<$	0.06 mm
B_s^0 DIRA	$>$	0.99995
min(K^+ IP , K^- IP)	$>$	0.1 mm MeV
max(K^+ IP , K^- IP)	$>$	0.3 mm MeV
min(K^+ p$_\mathrm{T}$, K^- p$_\mathrm{T}$)	$>$	1000 MeV
max(K^+ p$_\mathrm{T}$, K^- p$_\mathrm{T}$)	$>$	3000 MeV
track χ^2/ndf	$<$	5
p$_K$	$>$	700 MeV
p$_K$	$<$	150 GeV
track PIDK	$>$	3
track PIDp - track PIDK	$<$	5

Table B.5: Selection cuts for $B_d^0 \to K^{+,-}\pi^{-,+}$ data.

cut variable	condition	
B_s^0 mass	$\pm$	250 MeV
B_s^0 vertex χ^2	$<$	5
B_s^0 DOCA	$<$	0.06 mm
B_s^0 DIRA	$>$	0.99992
min(K^+ IP , K^- IP)	$>$	0.1 mm MeV
max(K^+ IP , K^- IP)	$>$	0.3 mm MeV
min(K^+ p_T , K^- p_T)	$>$	1000 MeV
max(K^+ p_T , K^- p_T)	$>$	3000 MeV
track χ^2/ndf	$<$	5
p_K	$>$	700 MeV
p_K	$<$	150 GeV
track_1 PIDK	$>$	3
track_1 PIDp - track_1 PIDK	$<$	5
track_2 PIDK	$<$	-3
track_2 PIDp	$<$	5
q_1	$>$	0
q_2	$<$	0

Table B.6: Selection cuts for $B_d^0 \to \pi^+\pi^-$ data.

cut variable	condition	
B_s^0 mass	$\pm$	250 MeV
B_s^0 vertex χ^2	$<$	5
B_s^0 DOCA	$<$	0.06 mm
B_s^0 DIRA	$>$	0.99995
min(K^+ IP , K^- IP)	$>$	0.1 mm MeV
max(K^+ IP , K^- IP)	$>$	0.3 mm MeV
min(K^+ p_T , K^- p_T)	$>$	1000 MeV
max(K^+ p_T , K^- p_T)	$>$	3000 MeV
track χ^2/ndf	$<$	5
p_K	$>$	700 MeV
p_K	$<$	150 GeV
track PIDK	$<$	-3
track PIDp + track PIDK	$<$	-5

Appendix C

Plots of track parameter influence on the mass resolution

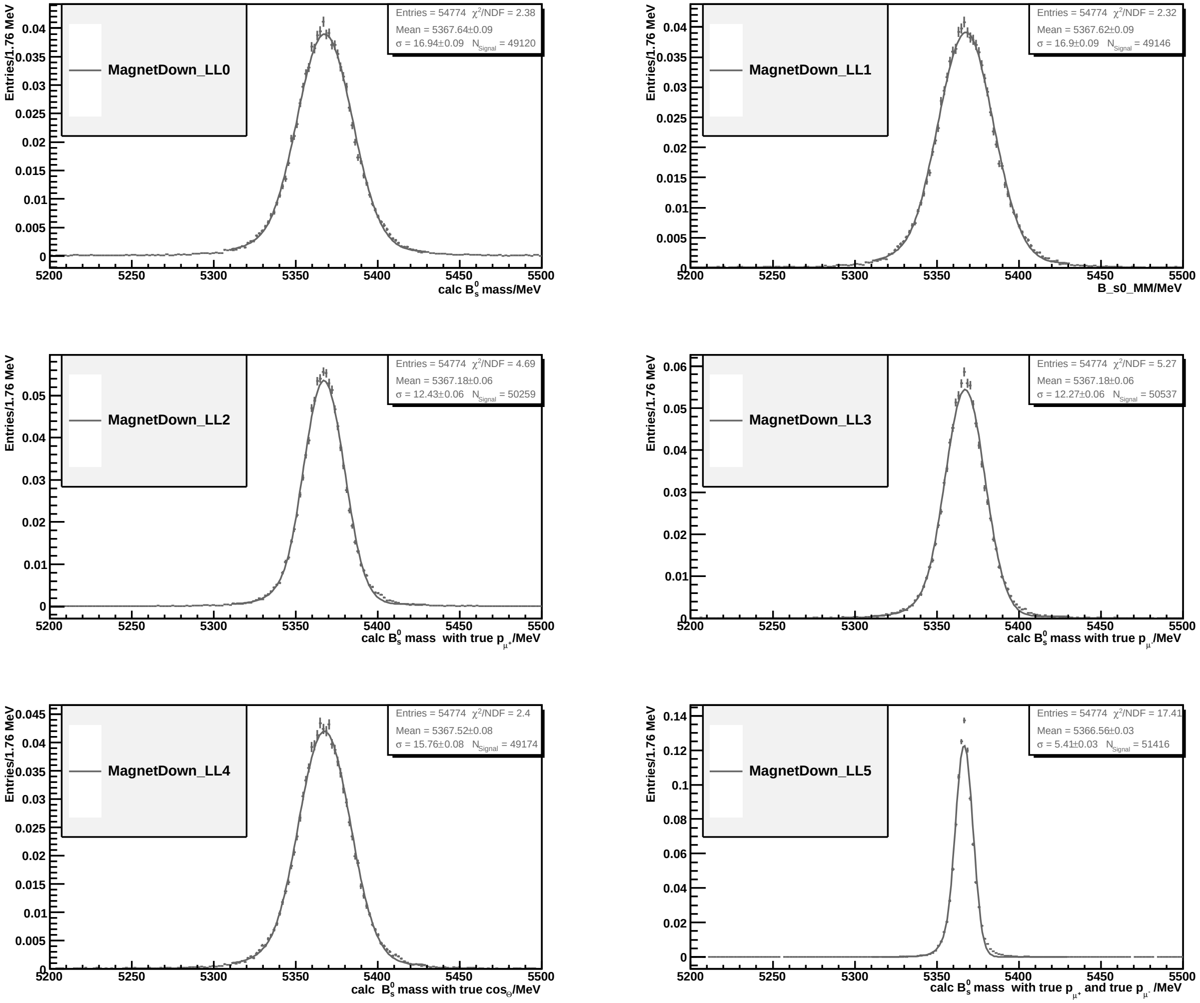

Figure C.1: Mass distributions of $\sqrt{s} = 7$ TeV $B_s^0 \to \mu^+\mu^-$ MC, with true p_μ or true $\cos\Theta$. The distributions are normalised.

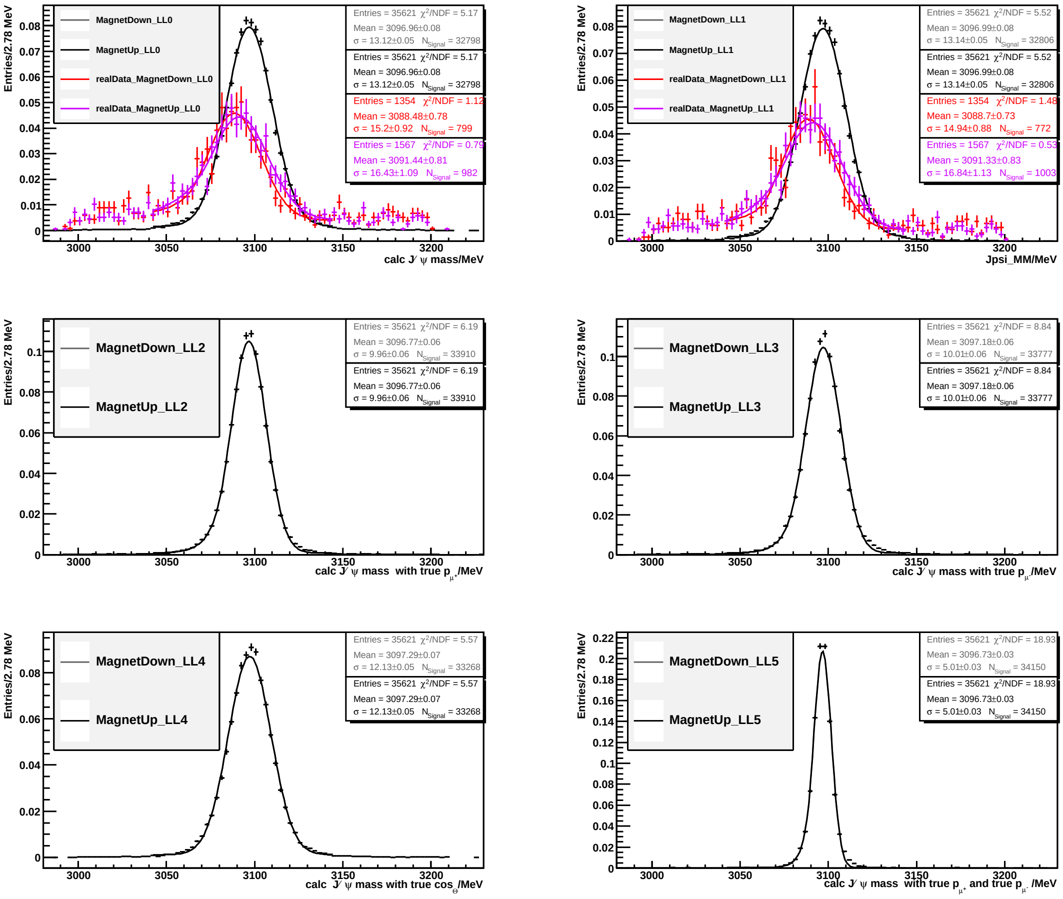

Figure C.2: Mass distribution of $J/\psi \to \mu^+\mu^-$ MC (black) and data from reconstruction 03, magnet 'down' in red and magnet 'up' in violet.

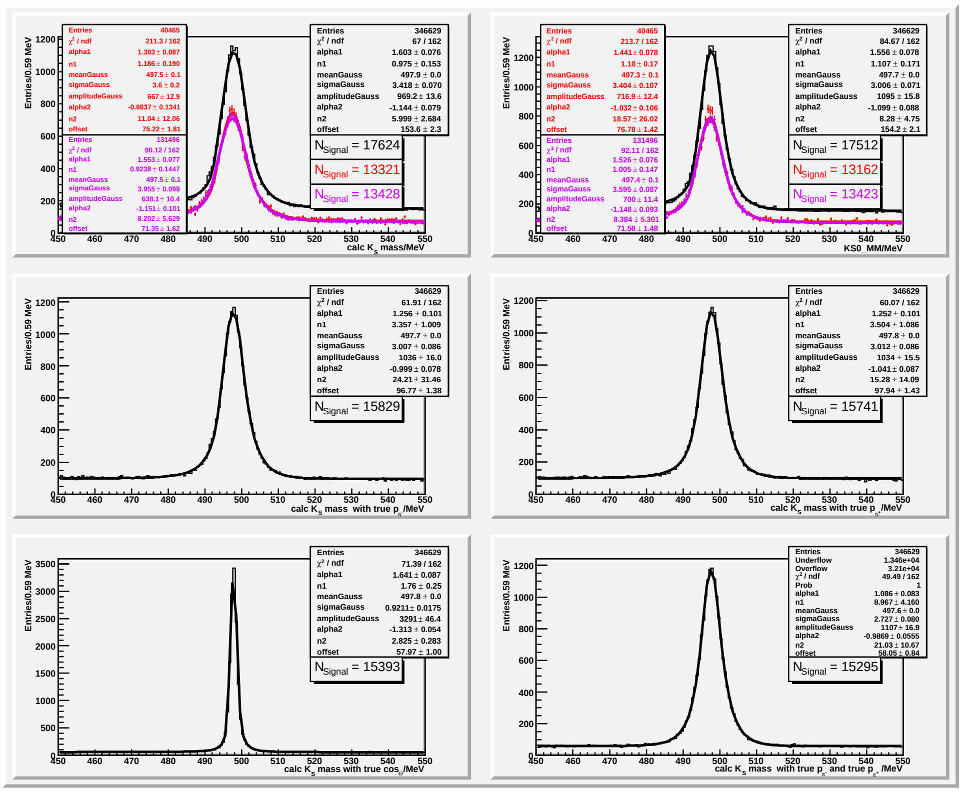

Figure C.3: Mass distributions $K_s^0 \to \pi^+\pi^-$ MC (black) and $K_s^0 \to \pi^+\pi^-$ data from $\sqrt{s} = 7$ TeV (magnet 'down' in red, magnet 'up' in violet).

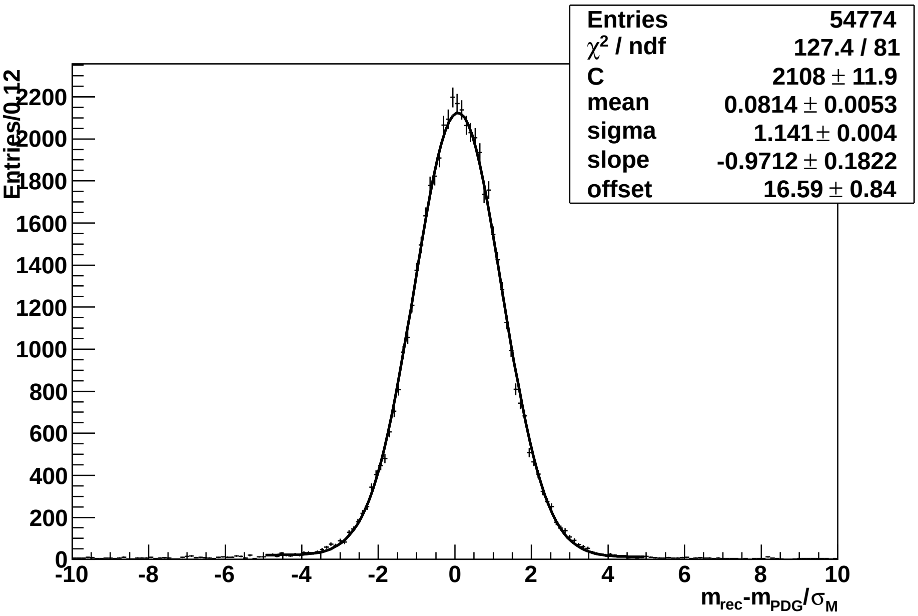

Figure C.4: Mass pull distribution of $B_s^0 \to \mu^+\mu^-$ MC.

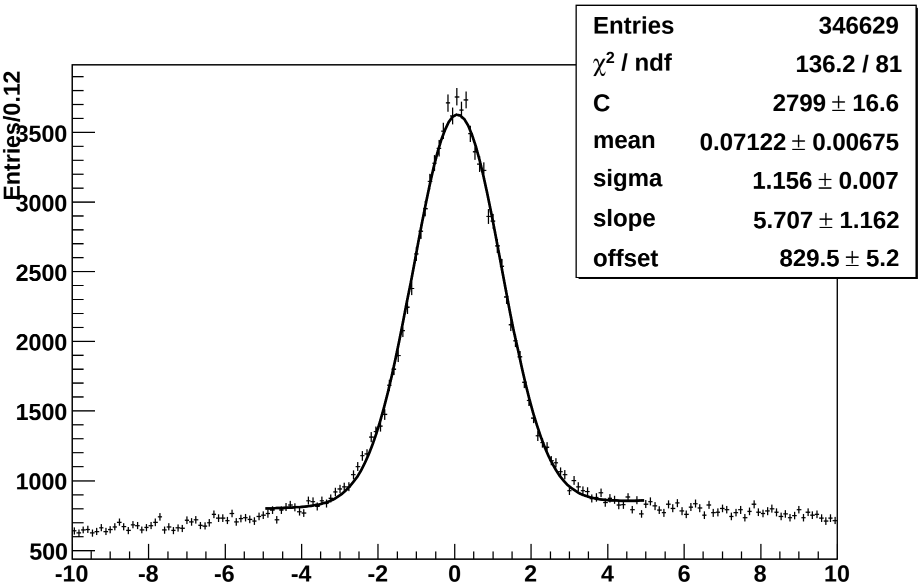

Figure C.5: Mass pull distribution of $K_s^0 \to \pi^+\pi^-$ MC.

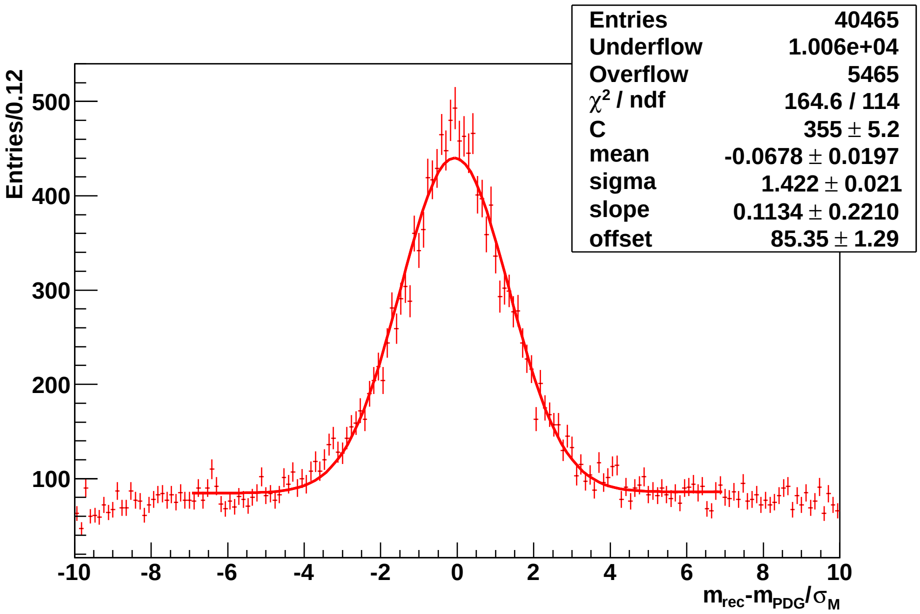

Figure C.6: Mass pull distribution of $K_s^0 \to \pi^+\pi^-$ data from $\sqrt{s} = 7$ TeV.

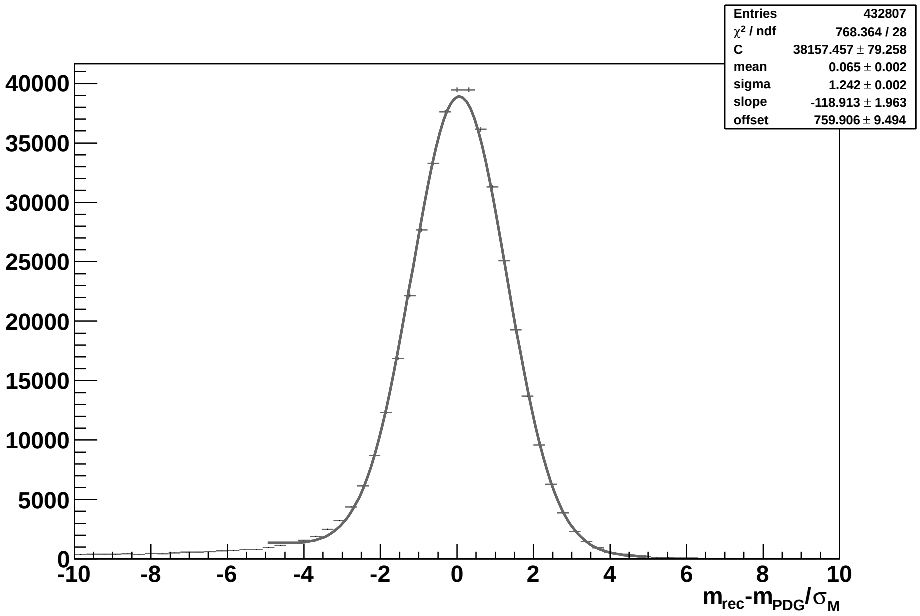

Figure C.7: Mass pull distribution of $J/\psi \to \mu^+\mu^-$ MC.

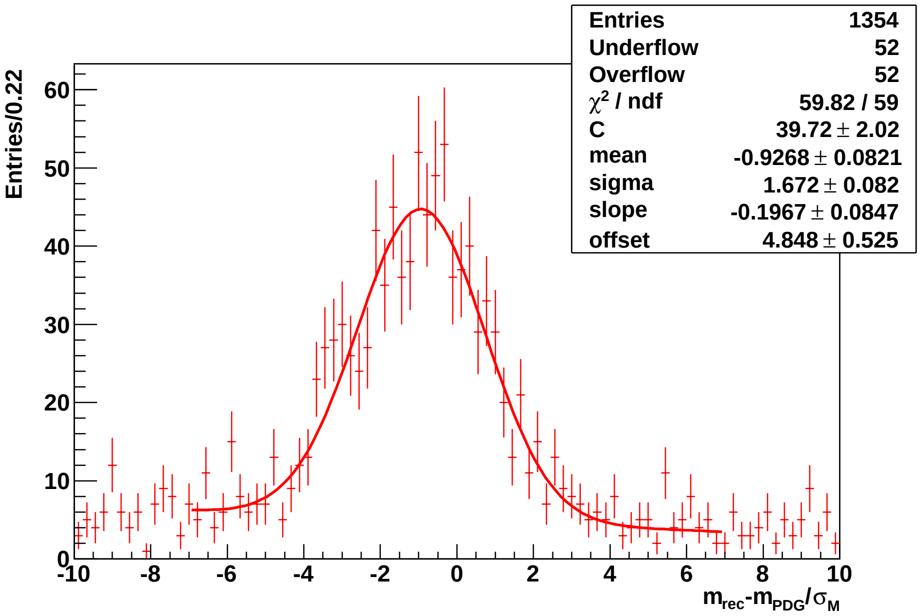

Figure C.8: Mass pull distribution of $J/\psi \to \mu^+\mu^-$data from reconstruction 03 and magnet 'down' polarity.

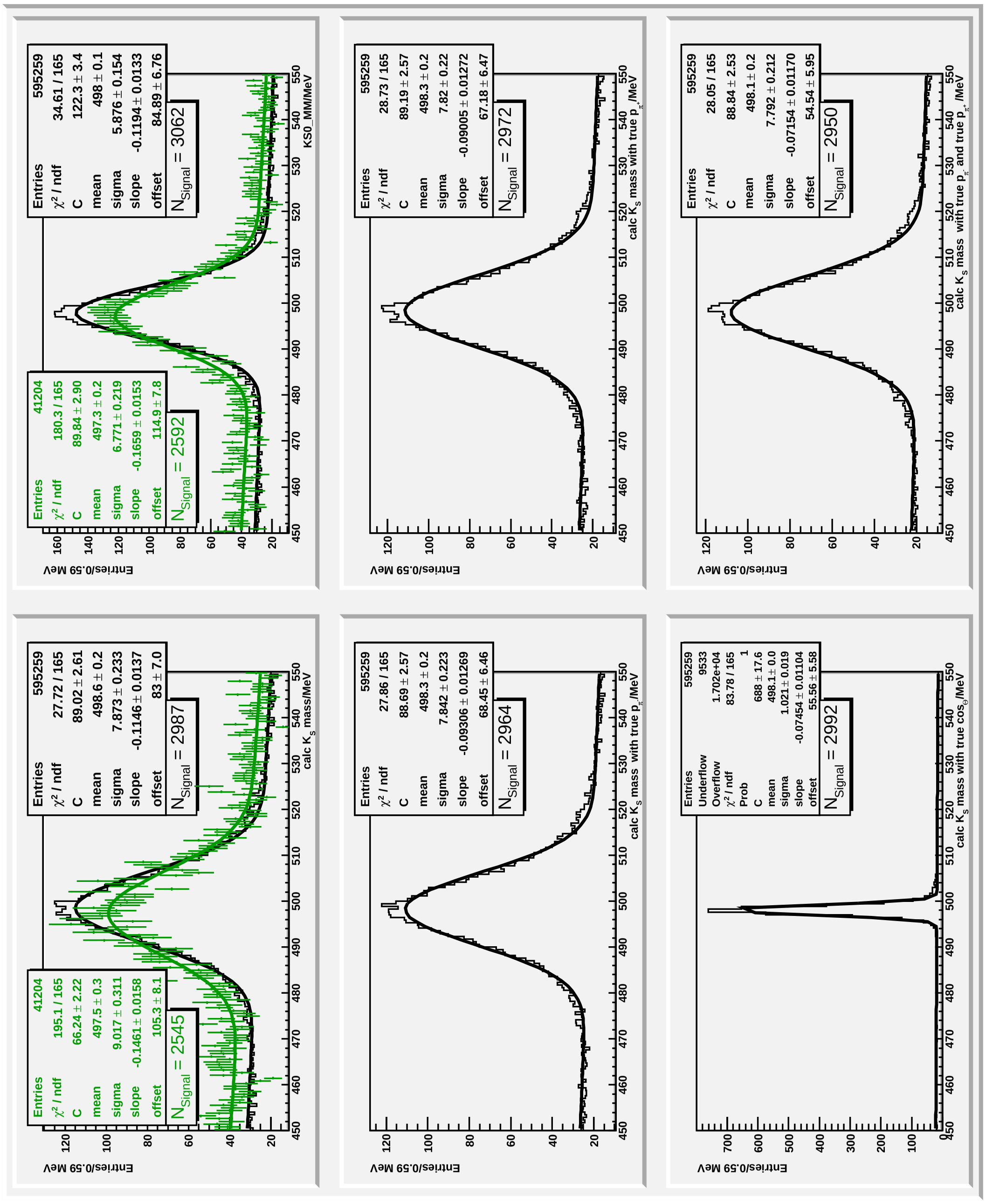

Figure C.9: Mass distributions MC (black) and $\sqrt{s} = 0.9$ TeV data (green) from $K_s^0 \rightarrow \pi^+\pi^-$, downstream tracks

Appendix D

Logarithmic Mass Plots

D.1 Logarithmic Mass Plots Data

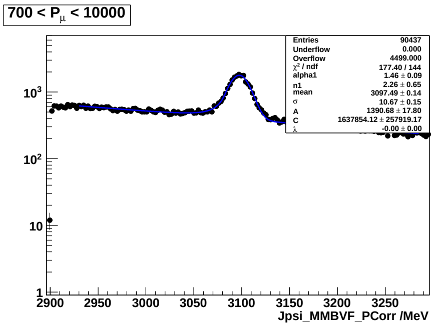

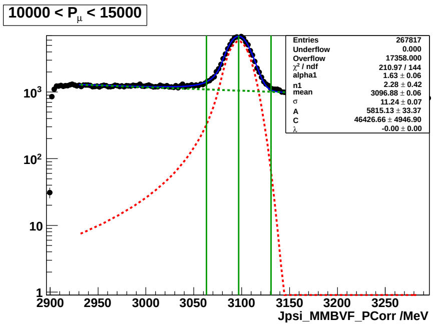

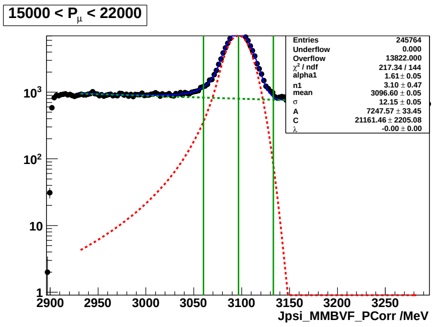

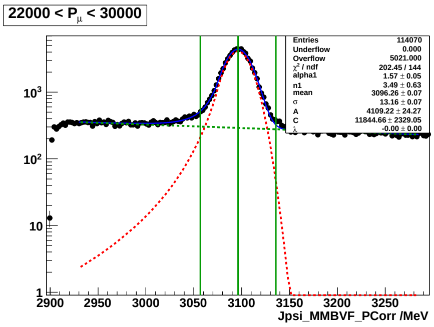

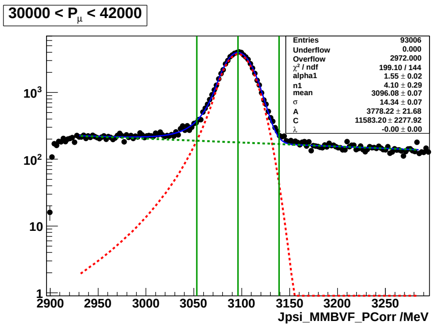
30000 < P_μ < 42000
Entries 93006
Underflow 0.000
Overflow 2972.000
χ² / ndf 199.10 / 144
alpha1 1.55 ± 0.02
n1 4.10 ± 0.29
mean 3096.08 ± 0.07
σ 14.34 ± 0.07
A 3778.22 ± 21.68
C 11583.20 ± 2277.92
λ -0.00 ± 0.00
10³
10²
10
1
2900
2950
3000
3050
3100
3150
3200
3250
Jpsi_MMBVF_PCorr /MeV

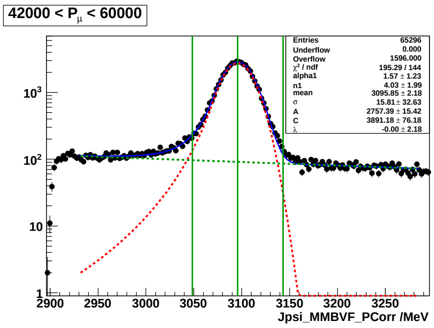
42000 < P_μ < 60000
Entries 65296
Underflow 0.000
Overflow 1596.000
χ² / ndf 195.29 / 144
alpha1 1.57 ± 1.23
n1 4.03 ± 1.99
mean 3095.85 ± 2.18
σ 15.81± 32.63
A 2757.39 ± 15.42
C 3891.18 ± 76.18
λ -0.00 ± 2.18
10³
10²
10
1
2900
2950
3000
3050
3100
3150
3200
3250
Jpsi_MMBVF_PCorr /MeV

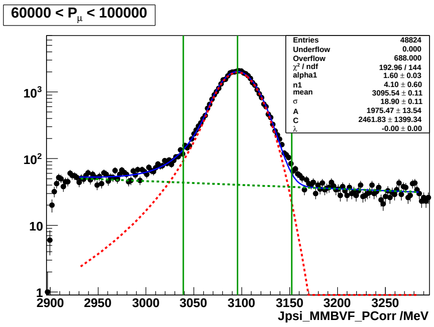
60000 < P_μ < 100000
Entries 48824
Underflow 0.000
Overflow 688.000
χ² / ndf 192.96 / 144
alpha1 1.60 ± 0.03
n1 4.10 ± 0.60
mean 3095.54 ± 0.11
σ 18.90 ± 0.11
A 1975.47 ± 13.54
C 2461.83 ± 1399.34
λ -0.00 ± 0.00
10³
10²
10
1
2900
2950
3000
3050
3100
3150
3200
3250
Jpsi_MMBVF_PCorr /MeV

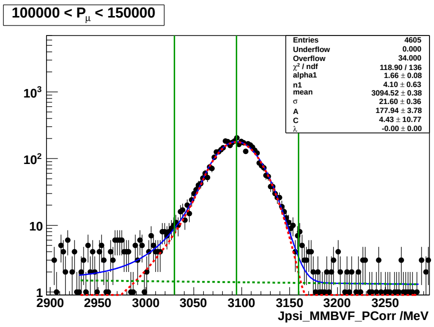
100000 < P_μ < 150000
Entries 4605
Underflow 0.000
Overflow 34.000
χ² / ndf 118.90 / 136
alpha1 1.66 ± 0.08
n1 4.10 ± 0.63
mean 3094.52 ± 0.38
σ 21.60 ± 0.36
A 177.94 ± 3.78
C 4.43 ± 10.77
λ -0.00 ± 0.00
10³
10²
10
1
2900
2950
3000
3050
3100
3150
3200
3250
Jpsi_MMBVF_PCorr /MeV

D.2 Logarithmic Mass Plots MC

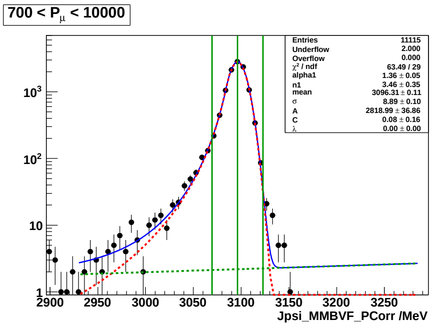

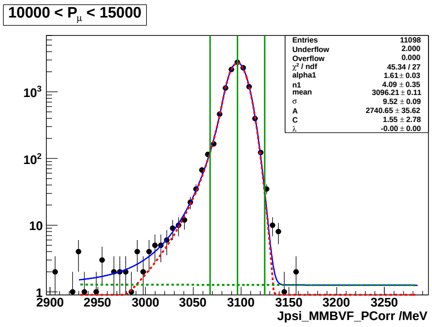

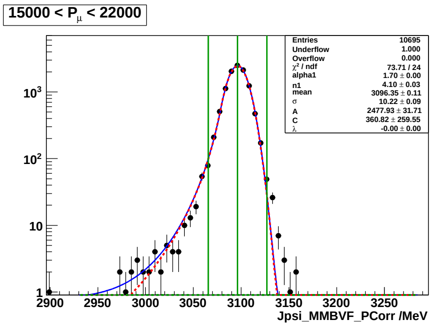

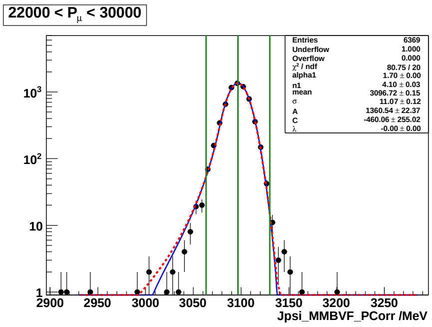

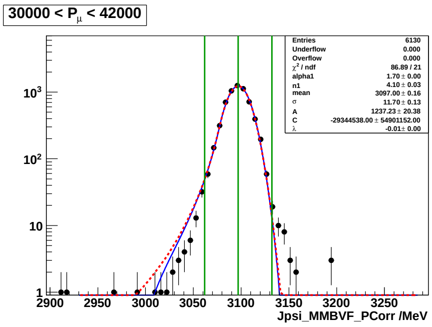

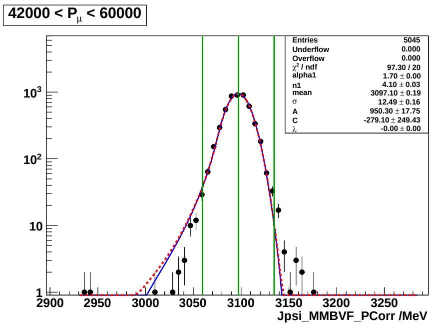

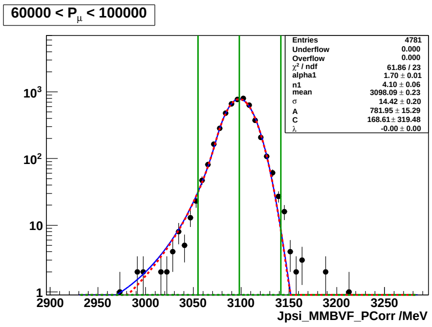
60000 < P_μ < 100000
Entries 4781
Underflow 0.000
Overflow 0.000
χ² / ndf 61.86 / 23
alpha1 1.70 ± 0.01
n1 4.10 ± 0.06
mean 3098.09 ± 0.23
σ 14.42 ± 0.20
A 781.95 ± 15.29
C 168.61 ± 319.48
λ -0.00 ± 0.00
10³
10²
10
1
2900
2950
3000
3050
3100
3150
3200
3250
Jpsi_MMBVF_PCorr /MeV

Appendix E

Mass in Momentum Bins MC

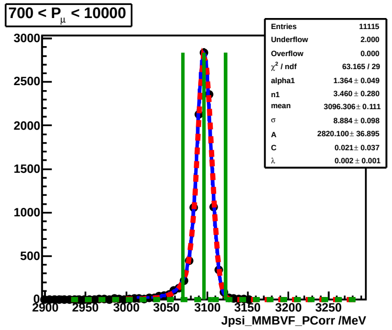
$700 < P_\mu < 10000$
Entries 11115
Underflow 2.000
Overflow 0.000
χ^2 / ndf 63.165 / 29
alpha1 1.364 ± 0.049
n1 3.460 ± 0.280
mean 3096.306 ± 0.111
σ 8.884 ± 0.098
A 2820.100 ± 36.895
C 0.021 ± 0.037
λ 0.002 ± 0.001
3000
2500
2000
1500
1000
500
0
2900
2950
3000
3050
3100
3150
3200
3250
Jpsi_MMBVF_PCorr /MeV

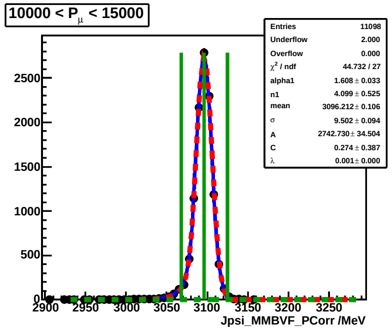
$10000 < P_\mu < 15000$
Entries 11098
Underflow 2.000
Overflow 0.000
χ^2 / ndf 44.732 / 27
alpha1 1.608 ± 0.033
n1 4.099 ± 0.525
mean 3096.212 ± 0.106
σ 9.502 ± 0.094
A 2742.730 ± 34.504
C 0.274 ± 0.387
λ 0.001 ± 0.000
2500
2000
1500
1000
500
0
2900
2950
3000
3050
3100
3150
3200
3250
Jpsi_MMBVF_PCorr /MeV

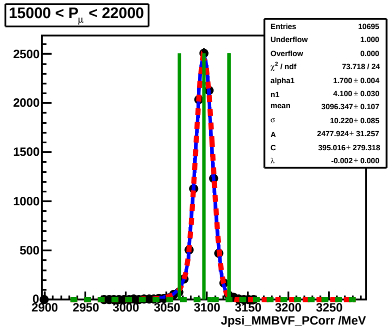
$15000 < P_\mu < 22000$
Entries 10695
Underflow 1.000
Overflow 0.000
χ^2 / ndf 73.718 / 24
alpha1 1.700 ± 0.004
n1 4.100 ± 0.030
mean 3096.347 ± 0.107
σ 10.220 ± 0.085
A 2477.924 ± 31.257
C 395.016 ± 279.318
λ -0.002 ± 0.000
2500
2000
1500
1000
500
0
2900
2950
3000
3050
3100
3150
3200
3250
Jpsi_MMBVF_PCorr /MeV

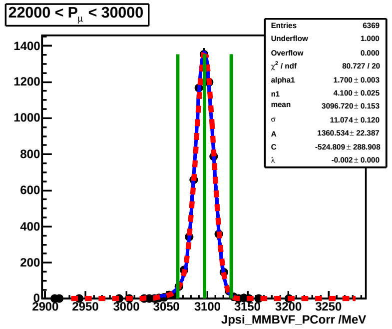
$22000 < P_\mu < 30000$
Entries 6369
Underflow 1.000
Overflow 0.000
χ^2 / ndf 80.727 / 20
alpha1 1.700 ± 0.003
n1 4.100 ± 0.025
mean 3096.720 ± 0.153
σ 11.074 ± 0.120
A 1360.534 ± 22.387
C -524.809 ± 288.908
λ -0.002 ± 0.000
1400
1200
1000
800
600
400
200
0
2900
2950
3000
3050
3100
3150
3200
3250
Jpsi_MMBVF_PCorr /MeV

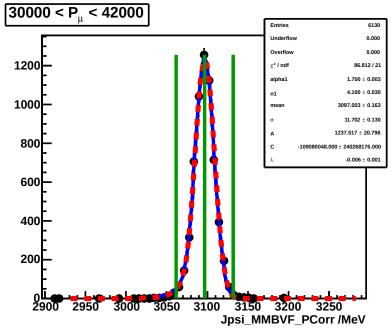
$30000 < P_\mu < 42000$
Entries 6130
Underflow 0.000
Overflow 0.000
χ^2 / ndf 86.812 / 21
alpha1 1.700 ± 0.003
n1 4.100 ± 0.030
mean 3097.003 ± 0.163
σ 11.702 ± 0.130
A 1237.517 ± 20.798
C -109080048.000 ± 240268176.000
λ -0.006 ± 0.001
1200
1000
800
600
400
200
0
2900
2950
3000
3050
3100
3150
3200
3250
Jpsi_MMBVF_PCorr /MeV

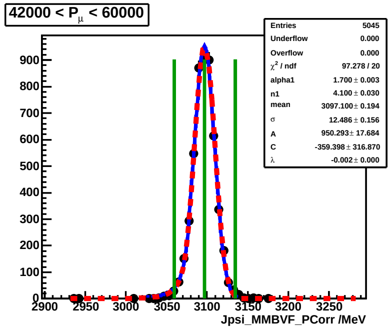
$42000 < P_\mu < 60000$
Entries 5045
Underflow 0.000
Overflow 0.000
χ^2 / ndf 97.278 / 20
alpha1 1.700 ± 0.003
n1 4.100 ± 0.030
mean 3097.100 ± 0.194
σ 12.486 ± 0.156
A 950.293 ± 17.684
C -359.398 ± 316.870
λ -0.002 ± 0.000
900
800
700
600
500
400
300
200
100
0
2900
2950
3000
3050
3100
3150
3200
3250
Jpsi_MMBVF_PCorr /MeV

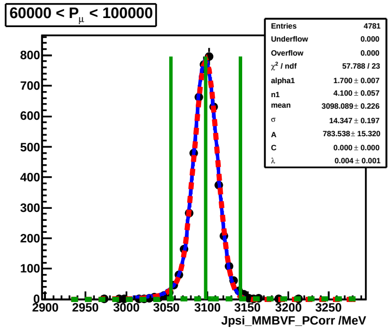
$60000 < P_\mu < 100000$
Entries 4781
Underflow 0.000
Overflow 0.000
χ^2 / ndf 57.788 / 23
alpha1 1.700 ± 0.007
n1 4.100 ± 0.057
mean 3098.089 ± 0.226
σ 14.347 ± 0.197
A 783.538 ± 15.320
C 0.000 ± 0.000
λ 0.004 ± 0.001
800
700
600
500
400
300
200
100
0
2900
2950
3000
3050
3100
3150
3200
3250
Jpsi_MMBVF_PCorr /MeV

Appendix F

$F(p)$ Plots from Sideband Subtraction Steps

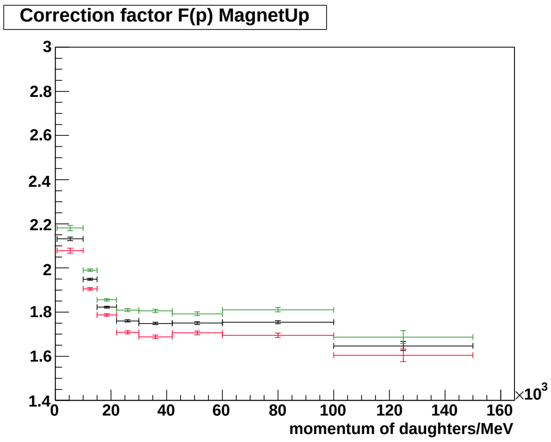

Figure F.1: Correction factor $F(p)$ for signal and background events in the signal window. In black is the approach with the full signal window, in red only the right half of the signal window is used. As a cross check only the left half of the signal window was used to compute $F(p)$ (green).

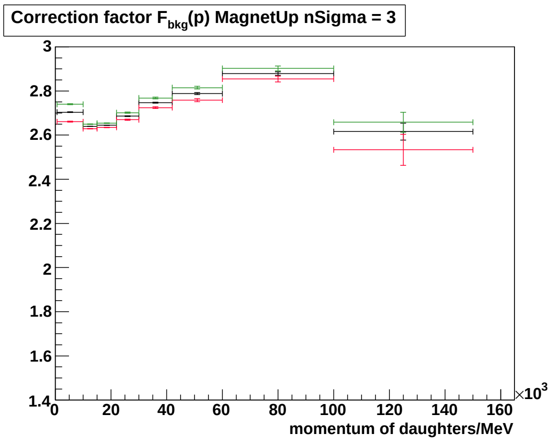

Figure F.2: Correction factor $F_{\text{bkg}}(p)$ for background events from mass sidebands. The colours indicate again the different approaches for $F(p)$ as explained in Figure F.1 but extended to the use of both (black), only the right (red) and only the left (green) sidebands.

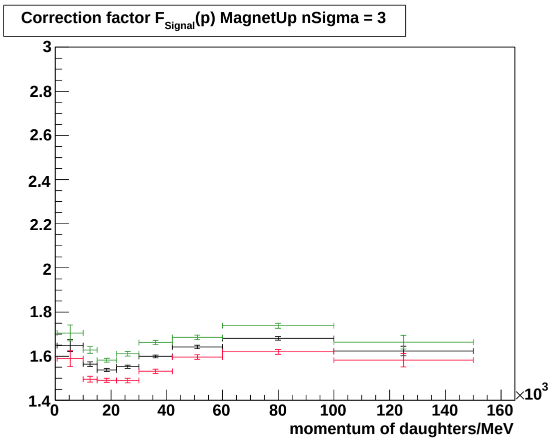

Figure F.3: Correction factor $F_{\text{Signal}}(p)$ after sideband subtraction of the background. In black is the approach with the full signal window, in red only the right half of the signal window is used. As a cross check only the left half of the signal window was used to compute $F_{\text{Signal}}(p)$ (green).

Appendix G

Mass Resolution Plots

G.1 J/ψ Magnet Up MC without Radiative Tail

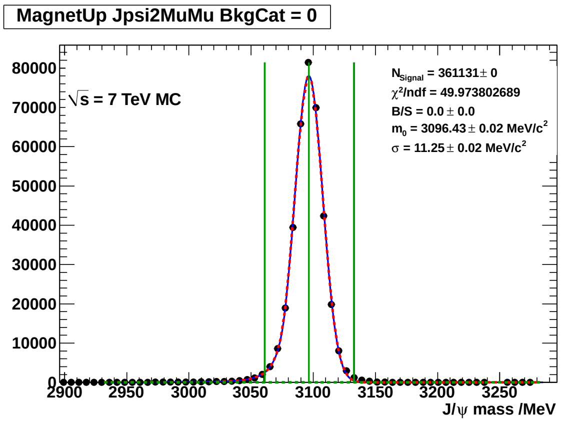

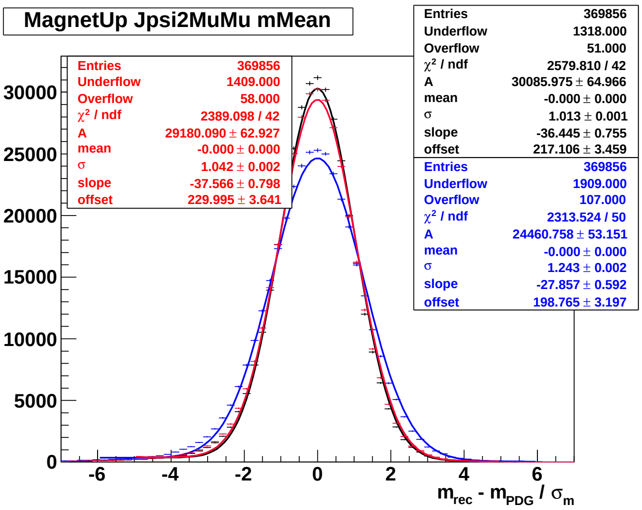

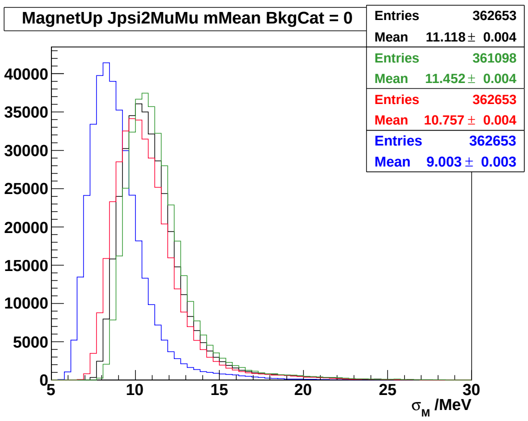

G.2 J/ψ Mass Error Magnet Up

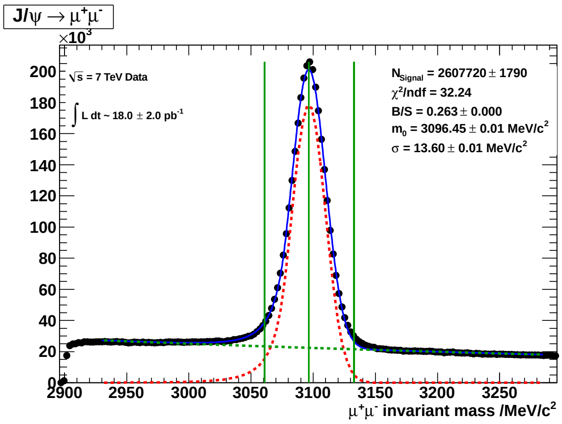

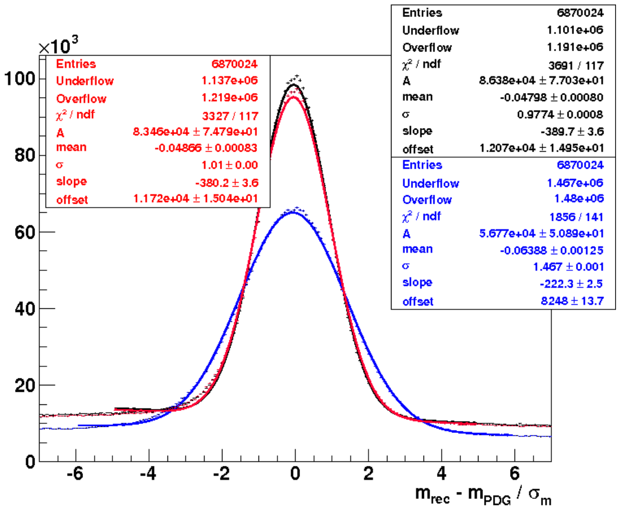

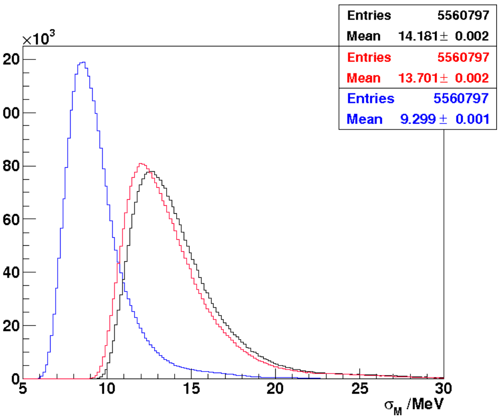

G.3 J/ψ Mass Error Magnet Down

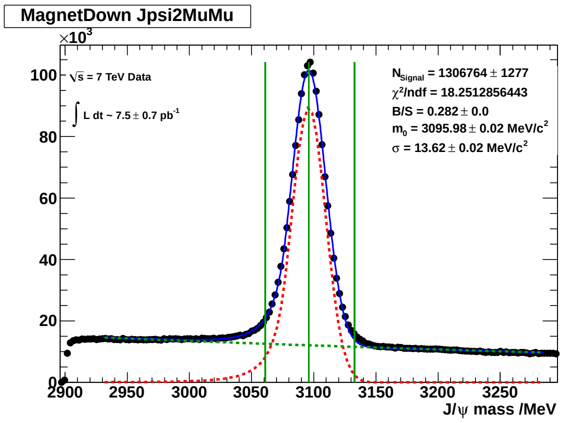

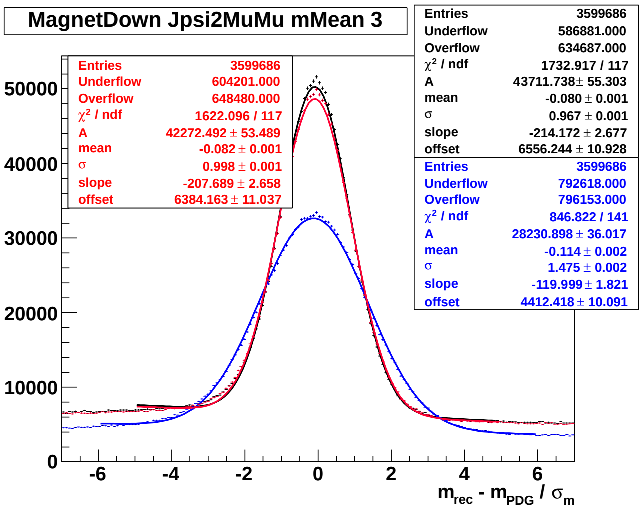

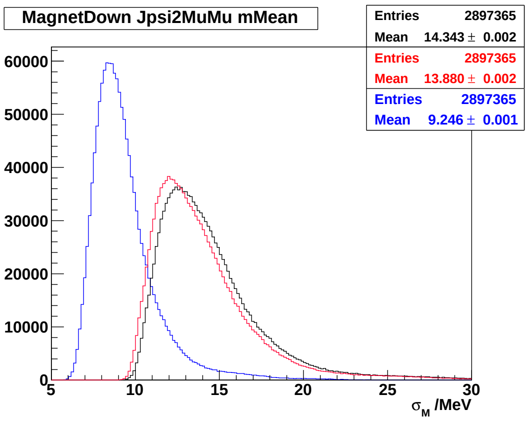

G.4 Υ Mass Error Magnet Up

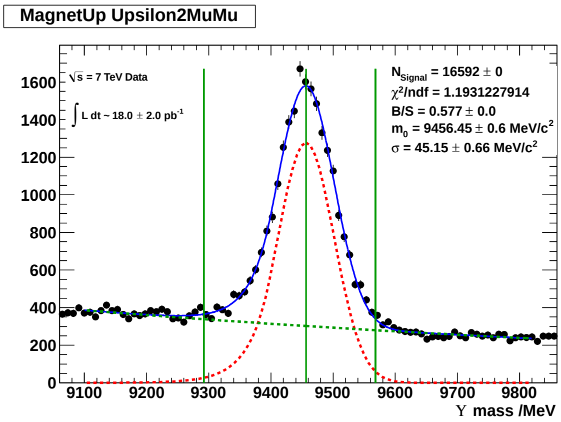

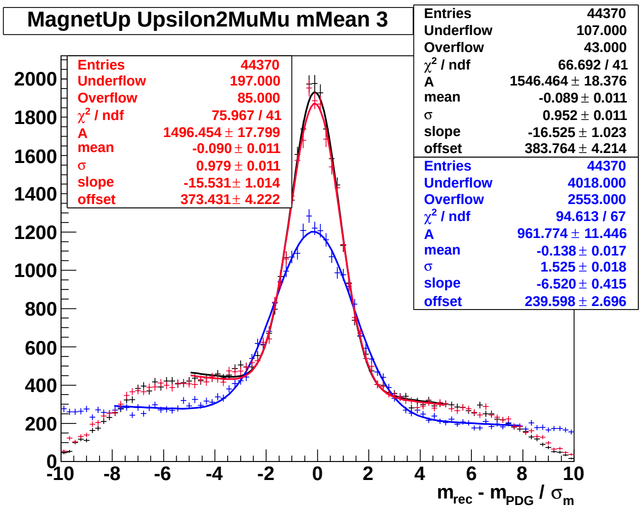

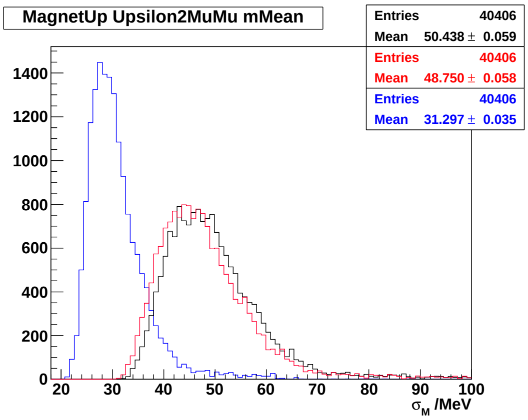

G.5 Υ Mass Error Magnet Down

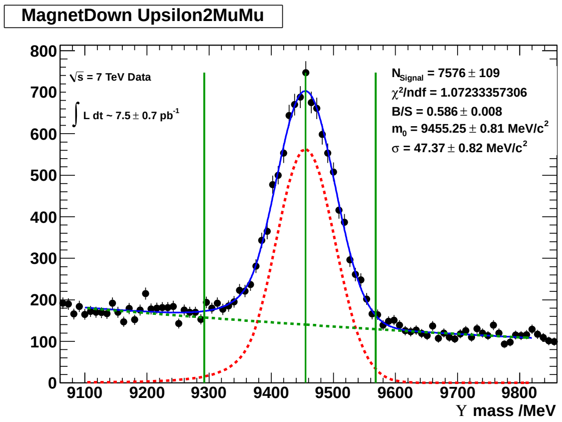

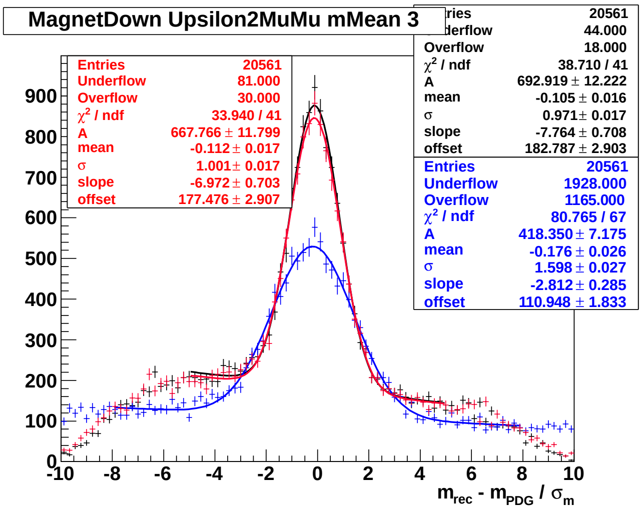

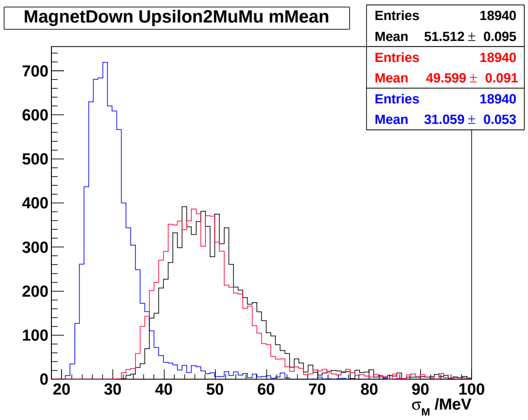

G.6 $B_s^0 \to K^+K^-$ Mass Error Magnet Up

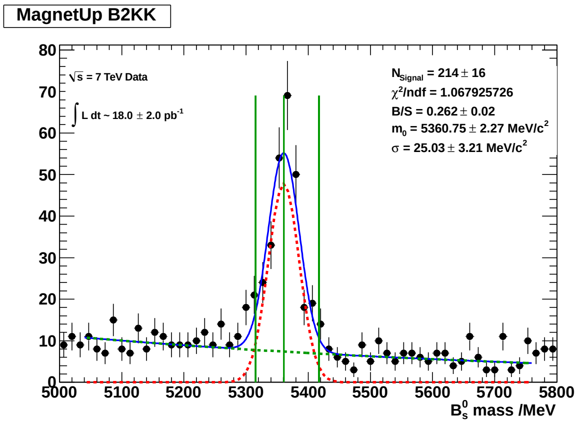

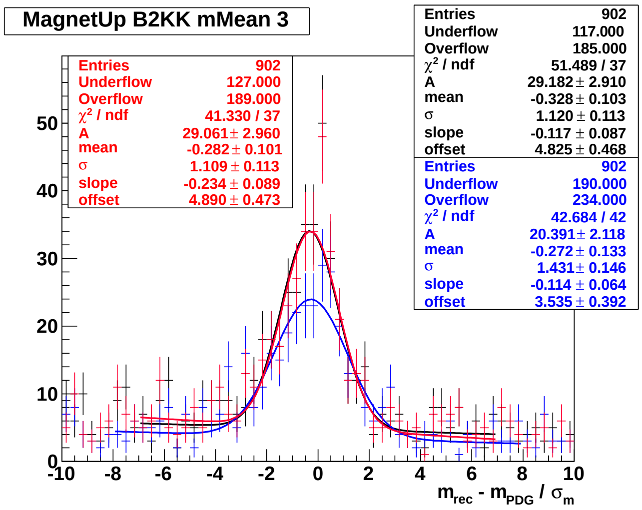

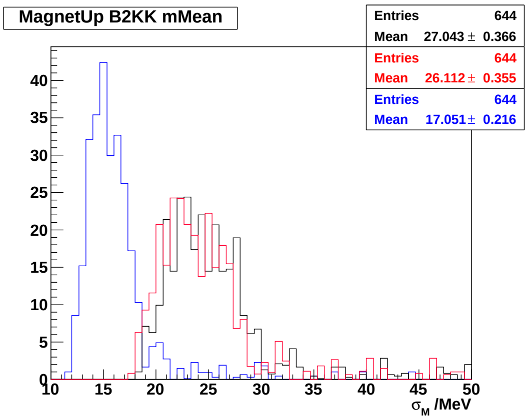

G.7 $B_d^0 \rightarrow K\pi$ Mass Error Magnet Up

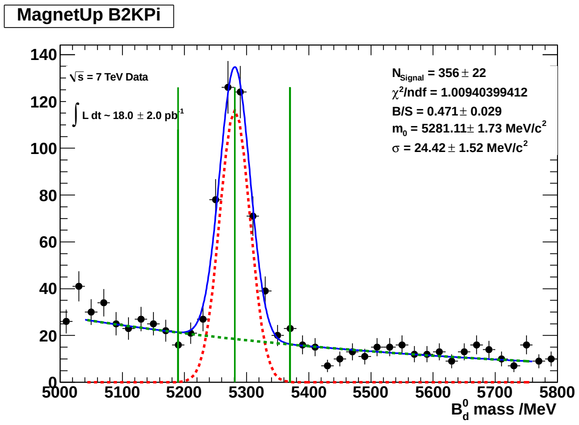

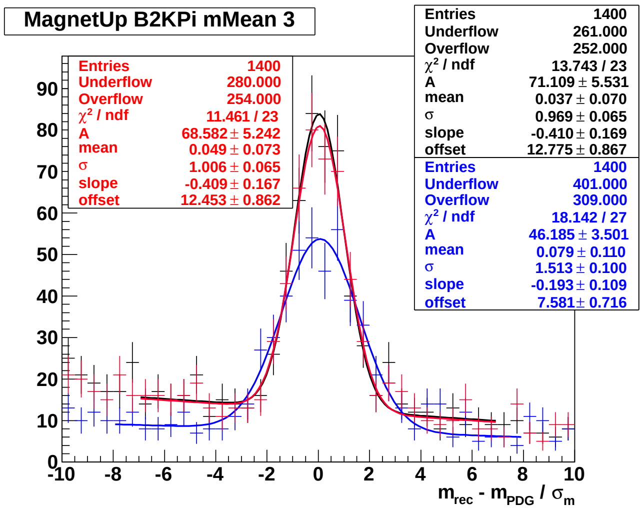

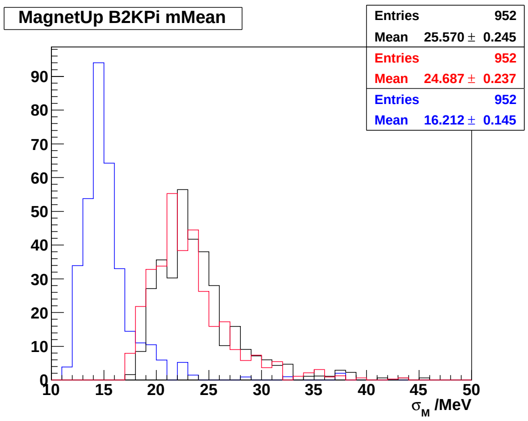

G.8 $B_d^0 \to \pi^+\pi^-$ Mass Error Magnet Up

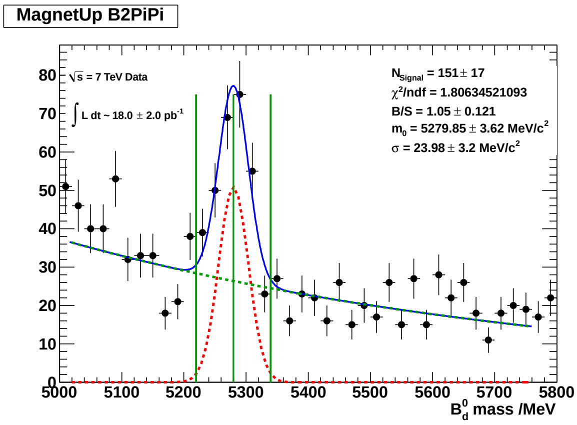

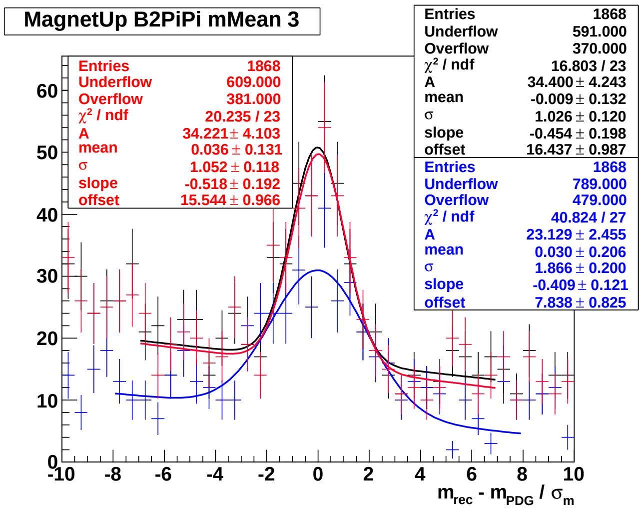

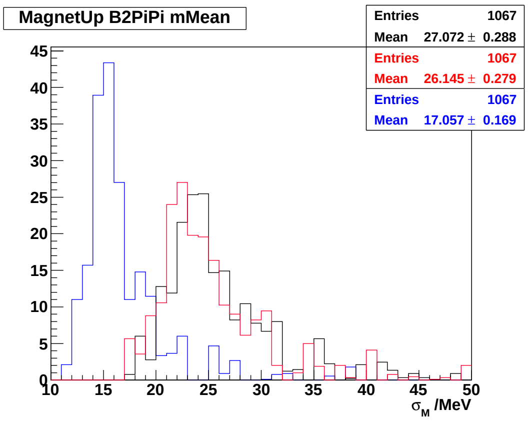

G.9 $B_d^0 \to K\pi$ Mass Error Magnet Down

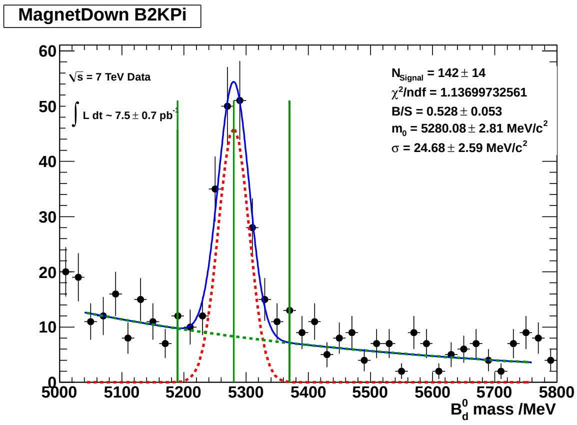

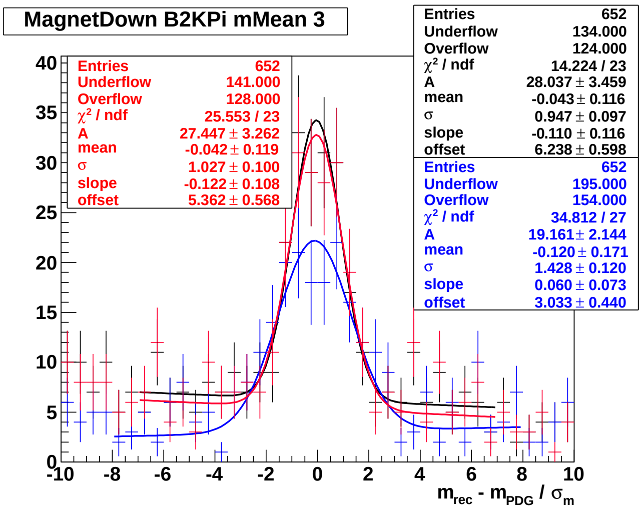

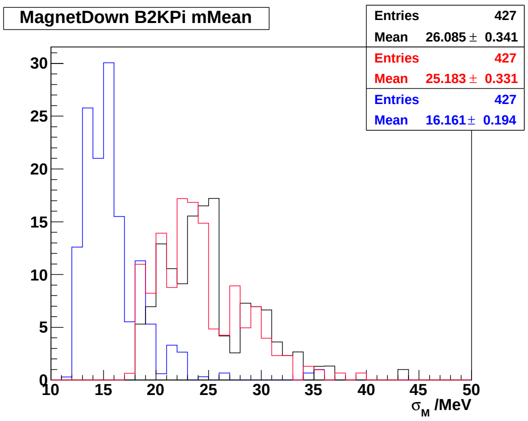

Appendix H

$F(p)$ for different window sizes

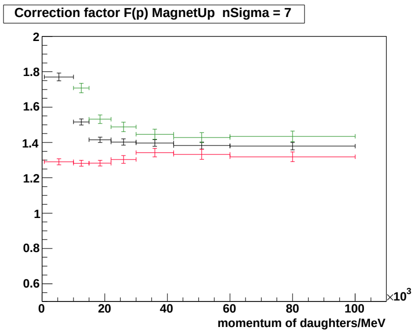
Correction factor F(p) MagnetUp nSigma = 7

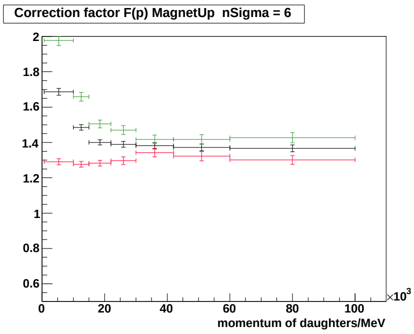
Correction factor F(p) MagnetUp nSigma = 6

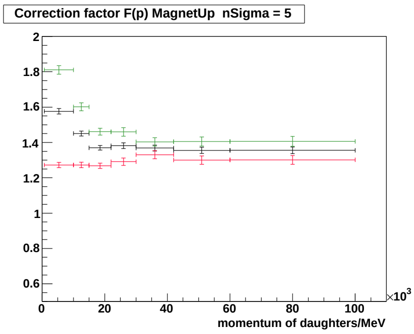
Correction factor F(p) MagnetUp nSigma = 5

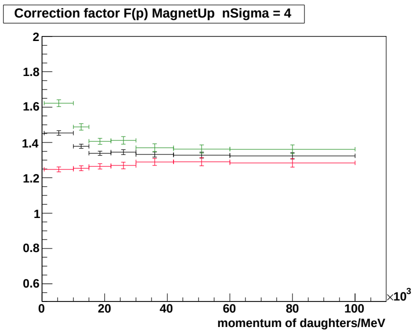
Correction factor F(p) MagnetUp nSigma = 4

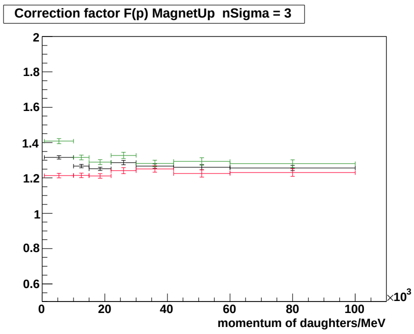
Correction factor F(p) MagnetUp nSigma = 3
2
1.8
1.6
1.4
1.2
1
0.8
0.6
0
20
40
60
80
100
$\times 10^3$
momentum of daughters/MeV

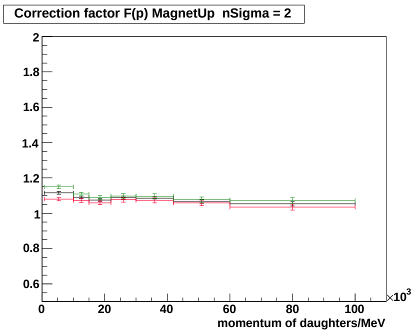
Correction factor F(p) MagnetUp nSigma = 2
2
1.8
1.6
1.4
1.2
1
0.8
0.6
0
20
40
60
80
100
$\times 10^3$
momentum of daughters/MeV

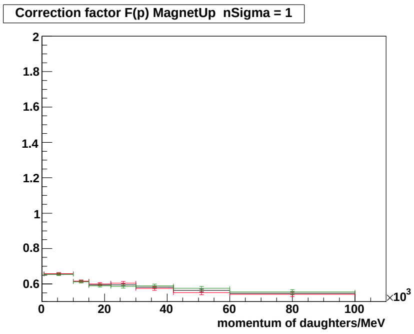
Correction factor F(p) MagnetUp nSigma = 1
2
1.8
1.6
1.4
1.2
1
0.8
0.6
0
20
40
60
80
100
$\times 10^3$
momentum of daughters/MeV

Appendix I

Technical Drawings for z-Positions of Silicon Layers

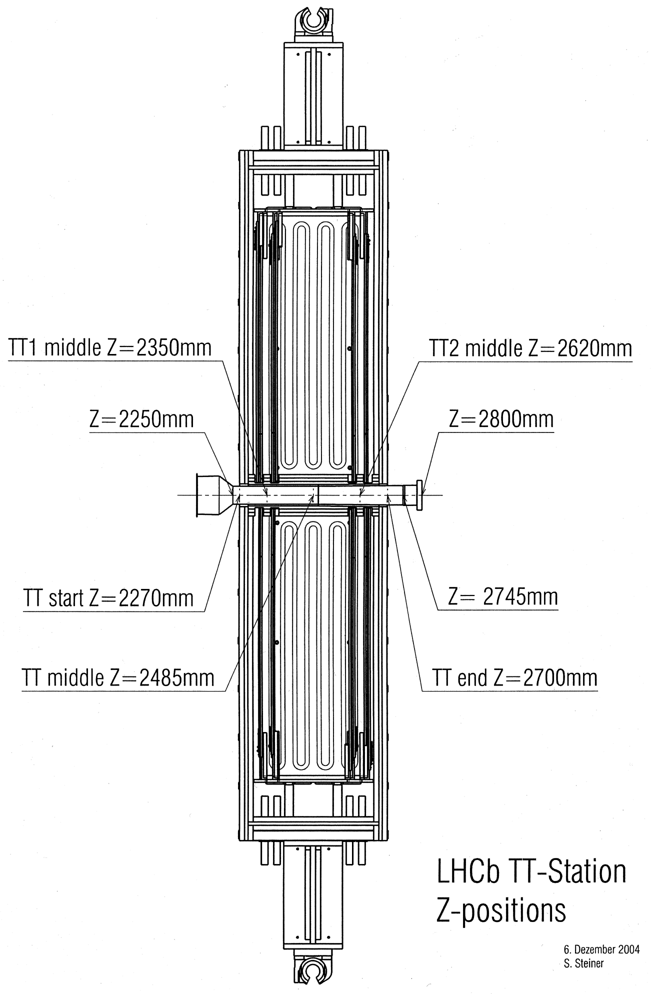

Figure I.1: TT1 middle and TT2 middle z-positions. TT1 middle is the centre of X1 and U layer, TT2 middle is the centre of V and X2 layer. On the left hand is the RICH1 and on the right hand the magnet.

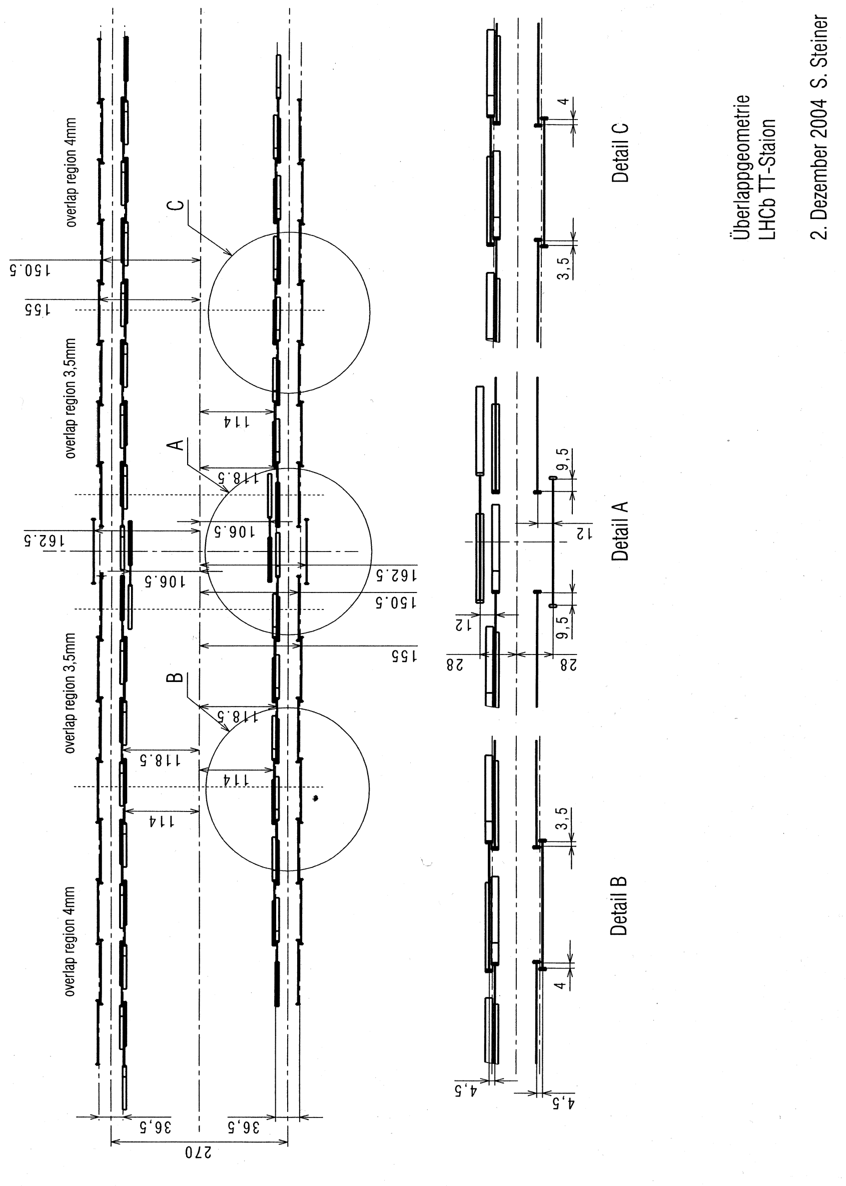

Figure I.2: The gap between X1 and U (V and X2 respectively) is 36.5 mm. To determine the z positions of the layers, for X1 $36.5/2 = 18.25$ mm are subtracted from the TT1 middle Z position I.1 and for U 18.25 mm are added to the TT1 middle z-position. For V and X2 analogue calculation but with TT2 middle z-position.

Appendix J

Colour changing polyurethane hoses

Table J.1: Parameters of the PU hoses given by the vendor Angst&Pfister

Material:	polyurethane, TPE-U (polyether- type)	
Colour:	blue, RAL 5015	
Operating temperature:	-20 to +80°C	
Product description:	highly flexible, external calibrated tube with high wear resistance	
Inner ∅:	4 mm	8 mm
Outer ∅:	6 mm	10 mm
Wall thickness:	1 mm	1 mm

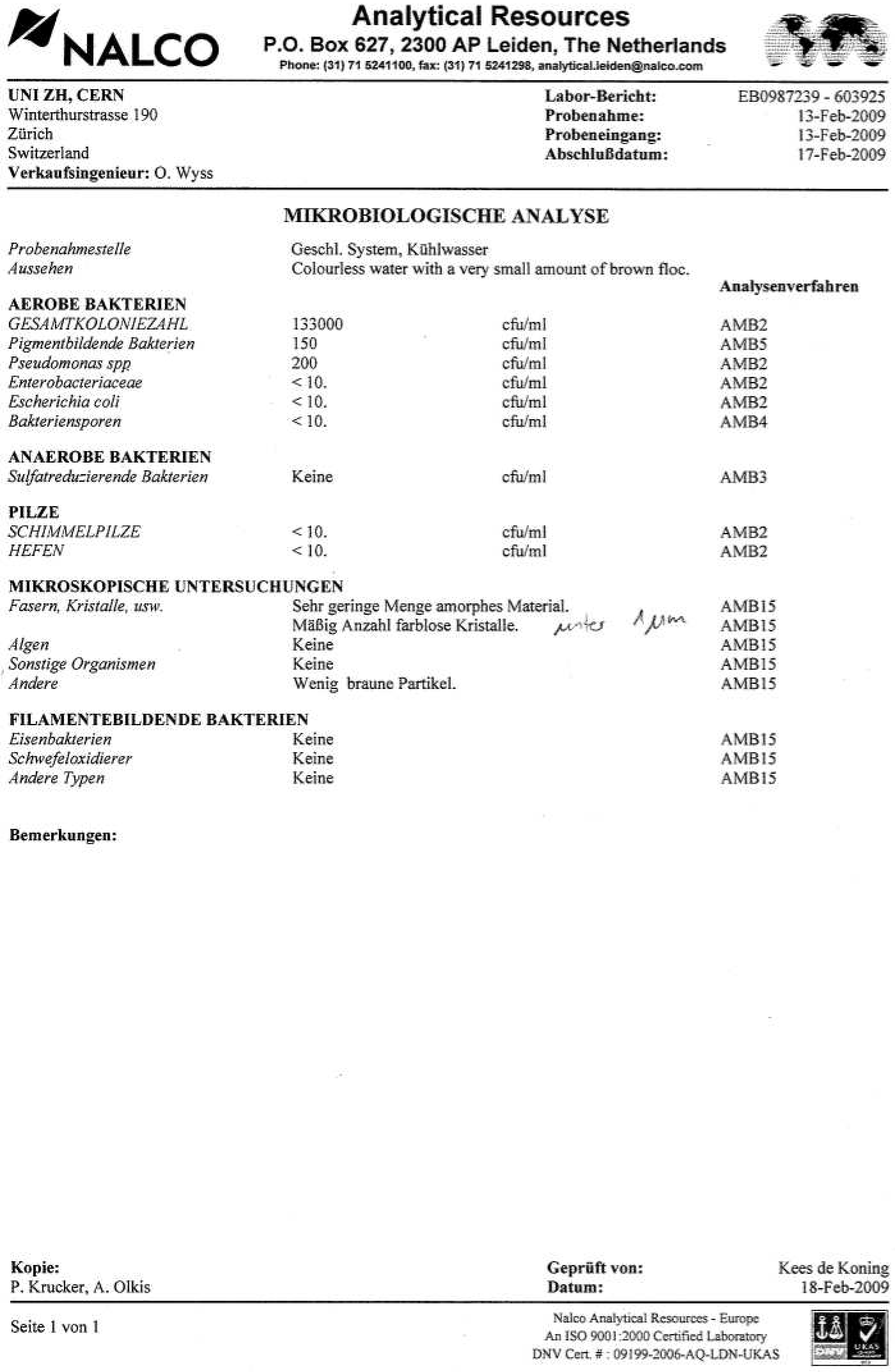

NALCO

Analytical Resources
P.O. Box 627, 2300 AP Leiden, The Netherlands
Phone: (31) 71 5241100, fax: (31) 71 5241298, analytical.leiden@nalco.com

UNI ZH, CERN
Winterthurstrasse 190
Zürich
Switzerland
Verkaufsingenieur: O. Wyss

Labor-Bericht:	EB0987239 - 603925
Probenahme:	13-Feb-2009
Probeneingang:	13-Feb-2009
Abschlußdatum:	17-Feb-2009

MIKROBIOLOGISCHE ANALYSE

Probenahmestelle	Geschl. System, Kühlwasser		
Aussehen	Colourless water with a very small amount of brown floc.		
			Analysenverfahren
AEROBE BAKTERIEN			
GESAMTKOLONIEZAHL	133000	cfu/ml	AMB2
Pigmentbildende Bakterien	150	cfu/ml	AMB5
Pseudomonas spp	200	cfu/ml	AMB2
Enterobacteriaceae	< 10.	cfu/ml	AMB2
Escherichia coli	< 10.	cfu/ml	AMB2
Bakteriensporen	< 10.	cfu/ml	AMB4
ANAEROBE BAKTERIEN			
Sulfatreduzierende Bakterien	Keine	cfu/ml	AMB3
PILZE			
SCHIMMELPILZE	< 10.	cfu/ml	AMB2
HEFEN	< 10.	cfu/ml	AMB2
MIKROSKOPISCHE UNTERSUCHUNGEN			
Fasern, Kristalle, usw.	Sehr geringe Menge amorphes Material.		AMB15
	Mäßig Anzahl farblose Kristalle.	unter 1µm	AMB15
Algen	Keine		AMB15
Sonstige Organismen	Keine		AMB15
Andere	Wenig braune Partikel.		AMB15
FILAMENTEBILDENDE BAKTERIEN			
Eisenbakterien	Keine		AMB15
Schwefeloxidierer	Keine		AMB15
Andere Typen	Keine		AMB15

Bemerkungen:

Kopie:
P. Krucker, A. Olkis

Geprüft von:	Kees de Koning
Datum:	18-Feb-2009

Seite 1 von 1

Nalco Analytical Resources - Europe
An ISO 9001:2000 Certified Laboratory
DNV Cert. # : 09199-2006-AQ-LDN-UKAS

NALCO
Analytical Resources
P.O. Box 627, 2300 AP Leiden, The Netherlands
Phone: (31) 71 5241100, fax: (31) 71 5241298, analytical.leiden@nalco.com

UNI ZH, CERN
Winterthurstrasse 190
Zürich
Switzerland
Verkaufsingenieur: O. Wyss

Labor-Bericht:	ED0932514 - 603958
Probenahme:	1-Feb-2009
Probeneingang:	13-Feb-2009
Abschlußdatum:	24-Feb-2009

ABLAGERUNGSANALYSE

Probenahmestelle: Not specified (tubes)

Infrared analysis

The sample was received as two pieces of blue tube, one short piece of 6 mm outer diameter and one long piece of 10 mm outer diameter. The two tubes, of unknown origin, showed a brown discolouration on the outside of the tubes The inner surface of the tubes was covered with brown deposit. A request was made to identify the nature of the brown deposit and the brown discolouration.

Visual examination and stereomicroscopy

Examination with a stereozoom microscope indicated that the inner surface of both tubes was covered with a thin layer of rust-brown deposit. This deposit could easily be scraped from the surface. The cleaned inner surface of the tubes had a dark-brown to black, shiny appearance. The outer surface was unevenly brown discoloured.

Scanning Electron Microscopy and X-ray micro-analysis

The tubes and their internal surface deposits were investigated with the Environmental SEM and its X-ray microanalysis (EDS) system. The internal surface deposits were scraped off prior to analysis.
EDS analysis of the rust-brown deposit in the 10 mm tube showed high Fe, low C, Si and Zn and traces of Al, P, S, Ca and Cu. C cannot be quantified by EDS, but its amount was estimated to be low. On a C- and H_2O-free base the composition would be approximately:

~85-90 %	Fe_2O_3
2-3 %	SiO_2
3-5 %	ZnO

EDS analysis of the rust-brown deposit in the 6 mm tube showed high Fe, low C, Si and Zn and traces of Al, P, S, Ca, Ni and Cu. C cannot be quantified by EDS, but its amount was estimated to be low. On a C- and H_2O-free base the composition would be approximately:

~85-90 %	Fe_2O_3
2-3 %	SiO_2
3-5 %	ZnO

EDS analysis of the blue parts of both tubes indicated the presence of C and O only. EDS analysis of the inner and outer surfaces of the brown discoloured parts of the tubes indicated that the inner surfaces contained roughly 7 % Fe_2O_3 and the outer surfaces 0.1 % Fe_2O_3. Apparently, the Fe-rich, brown deposit on the inner surfaces of the tubes penetrated into the tubes, causing the brown discolouration.

Infrared analysis

Infrared spectral analysis was performed to identify the nature of the tubes and their internal surface deposits using micro internal reflection techniques. This indicated that the blue tubes consisted of a poly(ester urethane) resin.
Infrared analysis of the brown internal surface deposits indicated the presence of primarily iron (hydr)oxides, probably mainly present as Goethite (α-FeOOH) and Lepidocrocite (γ-FeOOH). No significant amounts of other compounds were found.
Infrared analysis of the brown discoloured parts of the tubes did not indicate any significant differences when compared with the blue parts. No evidence was found for degradation of the poly(ester urethane).

Conclusions

The brown deposit on the internal surface of the blue poly(ester urethane) tubes was found to primarily consist of iron corrosion products. The brown discolouration of the blue tubes has also its origin in iron corrosion products. Poly(ester urethane) resin is known for its generally high water permeability, which apparently also causes iron corrosion products to penetrate into the material. No evidence was found for chemical degradation of the poly(ester

Kopie:	**Geprüft von:**	R. Schaap
A. Olkis, P. Krucker	**Datum:**	24-Feb-2009

NALCO

Analytical Resources
P.O. Box 627, 2300 AP Leiden, The Netherlands
Phone: (31) 71 5241100, fax: (31) 71 5241298, analytical.leiden@nalco.com

UNI ZH, CERN
Winterthurstrasse 190
Zürich
Switzerland
Verkaufsingenieur: O. Wyss

Labor-Bericht: ED0932514 - 603958
Probenahme: 1-Feb-2009
Probeneingang: 13-Feb-2009
Abschlußdatum: 24-Feb-2009

ABLAGERUNGSANALYSE

urethane) material.

Kopie:
A. Olkis, P. Krucker

Geprüft von: R. Schaap
Datum: 24-Feb-2009

Seite 2 von 2

Nalco Analytical Resources - Europe
An ISO 9001:2000 Certified Laboratory
DNV Cert. # : 09199-2006-AQ-LDN-UKAS

Bibliography

[1] Buras, A J and Isidori, G and Paradisi, P, “EDMs vs. CPV in B$_{s,d}$ mixing in two Higgs doublet models with MFV,” *arXiv*, no. 1007.5291v2, 2010.

[2] Aaij, R et al, “Search for the rare decays $B_s^0 \to \mu^+\mu^-$ and $B^0 \to \mu^+\mu^-$. oai:cds.cern.ch:1335686,” Mar 2011. Comments: 18 pages, 5 figures.

[3] Martin, S P, “A Supersymmetry Primer,” *arXiv*, vol. hep-ph, Sep 2011.

[4] Kazakov, D I, “Beyond the Standard Model (In Search of Supersymmetry),” *arXiv*, vol. hep-ph, Dec 2000.

[5] Zeller, G P et al (NuTeV Collaboration), “Erratum: Precise Determination of Electroweak Parameters in Neutrino-Nucleon Scattering [Phys. Rev. Lett. 88, 091802 (2002)],” *Phys. Rev. Lett.*, vol. 90, p. 239902, Jun 2003.

[6] Herb, S W et al, “Observation of a Dimuon Resonance at 9.5 GeV in 400-GeV Proton-Nucleus Collisions,” *Phys. Rev. Lett.*, vol. 39, pp. 252–255, Aug 1977.

[7] Christenson, J H and Cronin, J W and Fitch, V L and Turlay, R, “Evidence for the 2π Decay of the K$_2^0$ Meson,” *Phys. Rev. Lett.*, vol. 13, pp. 138–140, 1964.

[8] Nir, Y, “Flavor Physics and CP Violation,” (Rehovot 76100, Israel), Mar 2009.

[9] Amsler, C et al (Particle Data Group), *Physics Letters B667, 1 (2008) and 2009 partial update for the 2010 edition*, vol. 1. Jul 2008.

[10] CDF Collaboration, “Search for $B_s^0 \to \mu^+\mu^-$ and $B_d^0 \to \mu^+\mu^-$ Decays in 3.7 fb^{-1} of $p\overline{p}$ Collisions with CDF II,” *CDF Public Note*, no. 9892.

[11] Buchmueller, O et al, “Likelihood Functions for Supersymmetric Observables in Frequentist Analyses of the CMSSM and NUHM1,” *arXiv*, no. 0907.5568v1, 2009.

[12] Brüning, O S and Collier, P and Lebrun, P and Myers, S and Ostojic, R and Poole, J and Proudlock, P, *LHC Design Report*. Geneva: CERN, 2004.

[13] *LHCb: Technical Proposal*. Tech. Proposal, Geneva: CERN, 1998.

[14] Photo is a courtesy of De Cian, M, Physik-Institut, Universität Zürich.

[15] Potterat, C and Bay, A, *Direct Search for Standard Model-Like Higgs Boson and Software Integration of Data Acquisition Cards. oai:cds.cern.ch:1266883*. PhD thesis, Lausanne, EPFL, Lausanne, 2010. Presented on 06 May 2010.

[16] Antunes-Nobrega, R et al, *LHCb reoptimized detector design and performance: Technical Design Report*. Technical Design Report LHCb, Geneva: CERN, 2003.

[17] Löchner, S and Schmelling, M, "The Beetle Reference Manual - chip version 1.3, 1.4 and 1.5," Tech. Rep. CERN-LHCb-2005-105, CERN, Geneva, Nov 2006.

[18] Bajko, M et al, "Report of the Task Force on the Incident of 19th September 2008 at the LHC. oai:cds.cern.ch:1168025," Tech. Rep. CERN-LHC-PROJECT-Report-1168, CERN, Geneva, Mar 2009.

[19] Alves, A et al, "The LHCb Detector at the LHC," *J. Instrum.*, vol. 3, p. S08005, 2008. Also published by CERN Geneva in 2010.

[20] Haefeli, G and Bay, A and Gong, A and Gong, H and Mücke, M and Neufeld, N and Schneider, O, "The LHCb DAQ interface board TELL1," *Nucl. Instrum. Methods Phys. Res., A*, vol. 560, pp. 494–502, 2006.

[21] Sievers, P and Straumann, U, *A Silicon Inner Tracker for the LHCb Experiment*. PhD thesis, Universität Zürich, Geneva, 2002. Presented on Dec 2002.

[22] Baumann, G et al, "Quality Assurance of 100 CMS2-OB2 Sensors," Tech. Rep. CERN-LHCb-2004-105, CERN, Geneva, Feb 2005.

[23] Esperante Pereira, D, *Design and Development of Electronics and the Control Software for the Silicon Tracker of LHCb*. PhD thesis, Universidata de Santiago de Compostela, 2010.

[24] Moreira, P et al, "GOL Reference Manual," tech. rep., CERN - EP/MIC, Geneva, Oct 2005.

[25] Magazzu, G and Marchioro, A and Moreira, P, "DCUF User Guide," tech. rep., CERN - EP/MIC, Geneva, May 2004.

[26] Needham, M and Steinkamp, O, "Updated channel numbering and readout partitioning for the Silicon Tracker," Tech. Rep. CERN-LHCb-2007-137, CERN, Geneva, Nov 2007. revised version submitted on 2008-07-11 11:47:57.

[27] "PVSS-II, Prozessvisualisierungs- und Steuerungs-System, SCADA tool." http://www.pvss.com/. September 16^{th}, 2011, 14:20.

[28] "SMI++ - State Management Interface." http://smi.web.cern.ch/smi/. September 16^{th}, 2011, 14:20.

[29] Büchler, A, "Thermal and Mechanical Characterization of the TT Detector for the LHCb Experiment," Master's thesis, Physics Institute of the University of Zürich, Feb 2007.

[30] Vollhardt, A, "The LHCb Silicon Tracker: lessons learned (so far)," Tech. Rep. CERN-LHCb-2008-049, CERN, Geneva, Sep 2008.

[31] Knecht, M et al, "Commissioning of the LHCb Silicon Tracker using data from the LHC injection tests," May 2011. LHCb-TALK-2009-014.

[32] Christiansen, J and Marchioro, A and Moreira, P and Toifl, T, "TTCrx Reference Manual," tech. rep., CERN - EP/MIC, Geneva, Aug 2005.

[33] Esperante-Pereira, D and Vollhardt, A, "Design and development of the Control Board for the LHCb Silicon Tracker," Tech. Rep. CERN-LHCb-2007-153, CERN, Geneva, Jan 2008.

[34] The Particle Data Group, "The Review of Particle Physics," tech. rep., CERN, Geneva, Dec 2010.

[35] Knecht, M and Schneider, O, *Commissioning of the LHCb Inner Tracker and measurement of* V^0*-particle production in* pp *collisions at 0.9 TeV. oai:cds.cern.ch:1372190*. PhD thesis, Lausanne, EPFL, Lausanne, 2011. Presented 01 Jul 2011.

[36] Christiansen, J, "Requirements to the L0 front-end electronics; 2001 ed.," Tech. Rep. LHCb-2001-014, CERN, Geneva, Jul 2001. Supersedes LHCb-NOTE-FE-99-29.

[37] Read, A L, "Modified frequentist analysis of search results (the CL_s method)," no. CERN-OPEN-2000-205, 2000.

[38] Gandelman, M and Polycarpo, E, "The Performance of the LHCb Muon Identification Procedure," Tech. Rep. CERN-LHCb-2007-145, CERN, Geneva, Mar 2008.

[39] Martinez Santos, D and Adeva Andany, B and Hernando Morata, J A, *Study of the very rare decay* $B_s \to \mu^+\mu^-$ *in LHCb. oai:cds.cern.ch:1264603*. PhD thesis, Universidade de Santiago de Compostela, Santiago de Compostela, 2010. Presented on 05 May 2010.

[40] Louvot, R (on behalf of the Belle collaboration), "$\Upsilon(5S)$ Results at Belle," *arXiv*, vol. hep-ex, Sep 2009.

[41] LHCb Collaboration, "Average f_s/f_d b-hadron production fraction for 7TeV pp collisions," Jul 2011. No analysis notes related.

[42] Martínez, D and Hernando, J A and Teubert, F, "LHCb potential to measure/exclure the branching ratio of the decay $B_s \rightarrow \mu^+\mu^-$," Tech. Rep. CERN-LHCb-2007-033, CERN, Geneva, Apr 2007.

[43] Gaiser, J E, *Charmonium Spectroscopy from Radiative Decays of the $J/\psi$and Ψ'.* PhD thesis, Stanford Linear Accelerator Center, Stanford, California 94305, 1982.

[44] Elsasser, C, "Determination of the Invariant Mass Distribution for $B^0_{(s)} \rightarrow \mu^+\mu^-$ at the LHCb Experiment," Master's thesis, Mathematisch-naturwissenschaftliche Fakultät der Universität Zürich, Aug 2011.

[45] Bettler, MO and Schneider, O, *Construction of the Inner Tracker and Sensitivity to the $B^0_s \rightarrow \mu\mu$ Decay at LHCb. oai:cds.cern.ch:1257978.* PhD thesis, LPHE, Lausanne, Lausanne, 2010. Presented 01 Apr 2010.

[46] Van Tilburg, J and Merk, M, *Track simulation and reconstruction in LHCb. oai:cds.cern.ch:885750.* PhD thesis, Vrije Univ. Amsterdam, Amsterdam, 2005. Presented on 01 Sep 2005.

[47] Conti, G and Nakada, T, *LHCb detector momentum calibration with the first year data and a performance study of CP violation measurement with the $B^0_s \rightarrow J/\psi\phi$ decays. oai:cds.cern.ch:1300766.* PhD thesis, Lausanne, EPFL, Lausanne, 2010.

[48] Needham, M, "Momentum scale calibration using resonances," Tech. Rep. CERN-LHCb-2008-037. LPHE-2008-08, CERN, Geneva, Jul 2008.

[49] Bressieux, J and Needham, M and Schneider, O, "Measurement of the X(3872) mass using 2010 data," May 2011. LHCb-ANA-2011-030.

[50] Barlow, R, "Systematic Errors: Facts and Fictions," *arXiv*, vol. hep-ex, no. arXiv:hep-ex/0207026v1, 2002.

Acknowledgments

First of all I want to express my gratitude to Ueli Straumann for the unique opportunity for a disseration covering a wide variety of important phases of a detector. I want to thank him for the unconfined trust concerning the installation of the Tracker Turicensis, entrusting me even with the most delicate jobs. During the commissioning phase he made sure we got every support. He even sat down himself with me to get to the bottom of some nasty complex problems and brought in his valuable longterm experience. I always could count on his open ear and interest; whenever I felt like sharing a problem, he took time to listen. This I appreciate most looking at his tight time schedule.

Then of course I want to thank my friend Stefan Steiner for the great time during installation and commissioning. I doubth that I will ever experience again such working harmony with someone, where one has the same ideas how problems should be solved before sharing them and the same working flow. With Daniel Esperante I shared joy and pain with PVSS and I want to thank him for this great time, all his help and patience. And it was always a joy, whenever Achim Vollhardt joined us to help out. In that context I want to thank Abraham Gallas for cheering me up with surprising statements and his good company. Thanks to Rolf Lindner all kind of experimental hall related problems could be solved in a uncomplicated way and I liked our coffee breaks and the nice discussions.

My two supervisors Jeroen van Tilburg and Olaf Steinkamp were supporting me a lot for the analysis part. I am most thankful for the fruitful discussions, the many thoughts they spent about unexpected results and of course for the time they invested to read and comment my thesis so carefully. And Jeroen, thanks a lot for your patience with me.

A big thanks goes to my office mates Christophe, Michel, Mark, Jonny and Philipp. You are my heroes, helped me out with a zillion of problems (mainly software related) and made my office life during my PhD much more joyful.

Andi, thanks a million for everything you have done for me during these years.

Christian, thanks a lot for your efforts to remove the high energy particle physics slang in my thesis and for your proofreading, which I appreciate a lot.

I am very grateful for my sister Ramona and my parents, as well as all my friends who supported me the one or the other way during my PhD time or even came visiting me at LHCb.

This work was supported by the Swiss National Foundation SNF.

CURRICULUM VITAE

PERSONAL INFORMATION

Last Name: Büchler
First Name: Angela
Day of Birth: 30. August, 1977
Hometown and Canton: Goldach, SG

EDUCATION

2007–2011	**Dissertation** in Physics, University of Zürich *Mass Resolution Study of the B_s-Meson* *with First LHCb Data* Supervisor: Prof. Dr. Ulrich Straumann
2007	**Master of Science** at University of Zürich
2006–2007	Master Thesis, University of Zürich *Thermal and Mechanical Characterization* *of the TT Detector for the LHCb Experiment* Supervisor: Prof. Dr. Ulrich Straumann
2002–2007	Study of Physics, University of Zürich
1999–2002	Primary School Teacher, 4th to 6th grade, Dällikon ZH
1999	**Primarlehrerdiplom**
1993–1999	Primarlehrerseminar Kantonsschule Heerbrugg.